

Relaxation and physical aging in network glasses: a review

This content has been downloaded from IOPscience. Please scroll down to see the full text.

2016 Rep. Prog. Phys. 79 066504

(<http://iopscience.iop.org/0034-4885/79/6/066504>)

View [the table of contents for this issue](#), or go to the [journal homepage](#) for more

Download details:

IP Address: 134.157.146.58

This content was downloaded on 23/05/2016 at 14:51

Please note that [terms and conditions apply](#).

Review

Relaxation and physical aging in network glasses: a review

Matthieu Micoulaut

Paris Sorbonne Universités, LPTMC—UPMC, 4 place Jussieu, 75252 Paris cedex 05, France

E-mail: mmi@lptl.jussieu.fr

Received 31 March 2014, revised 22 February 2016

Accepted for publication 29 February 2016

Published 23 May 2016



Invited by Sean Washburn

Abstract

Recent progress in the description of glassy relaxation and aging are reviewed for the wide class of network-forming materials such as GeO_2 , $\text{Ge}_x\text{Se}_{1-x}$, silicates ($\text{SiO}_2\text{--Na}_2\text{O}$) or borates ($\text{B}_2\text{O}_3\text{--Li}_2\text{O}$), all of which have an important usefulness in domestic, geological or optoelectronic applications. A brief introduction of the glass transition phenomenology is given, together with the salient features that are revealed both from theory and experiments. Standard experimental methods used for the characterization of the slowing down of the dynamics are reviewed. We then discuss the important role played by aspects of network topology and rigidity for the understanding of the relaxation of the glass transition, while also permitting analytical predictions of glass properties from simple and insightful models based on the network structure. We also emphasize the great utility of computer simulations which probe the dynamics at the molecular level, and permit the calculation of various structure-related functions in connection with glassy relaxation and the physics of aging which reveal the non-equilibrium nature of glasses. We discuss the notion of spatial variations of structure which leads to the concept of ‘*dynamic heterogeneities*’, and recent results in relation to this important topic for network glasses are also reviewed.

Keywords: glasses, structure, relaxation

(Some figures may appear in colour only in the online journal)

Symbols

T_m	Melting temperature	T_K	Kauzmann temperature
η	Viscosity	S_c	Configurational entropy
$H, H(T)$	Enthalpy	τ	Structural relaxation time
V	Volume	$\bar{r} = \langle r \rangle$	Network mean coordination number
C_p	Heat capacity	$S(k)$	Static structure factor
T_g	Glass transition temperature	$g(r)$	Pair correlation function
η_∞	Viscosity at infinite temperature	k_{FSDP}	First sharp diffraction peak position of $S(k)$
E_A	Activation energy for viscous flow	Δk_{FSDP}	Width of the first sharp diffraction peak of $S(k)$
\mathcal{M}	Fragility	β	Kohlrausch exponent characterizing the stretched exponent
G_∞	Infinite frequency shear modulus	f_c	Non-ergodicity parameter characterizing the β -relaxation plateau
T_0	Characteristic temperature of the VFT equation		

t_R	Reaction time in glass homogeneity studies	$P_{\alpha\beta}$	Molecular stress tensor
σ_M	Variance of fragility measurements	A_H	Area of the enthalpy hysteresis curve in a cooling/heating experiment across the glass transition
T_f	Fictive temperature		
T_w	Temperature at which an aging experiment is performed	A_V	Area of the volume hysteresis curve in a cooling/heating experiment across the glass transition
q	Heating rate during a glass transition measurement		
R	Ideal gas constant	\mathcal{N}	Number of outer shell electrons
C_{pg}	Glass heat capacity	\bar{r}_{c2}	Network mean coordination number at the stress transition
C_{pe}	Equilibrium heat capacity	\bar{r}_{c1}	Network mean coordination number at the rigidity transition
$C_p^*(i\omega)$	Complex heat capacity		
$\varepsilon^*(i\omega)$	Complex permittivity	D or D_i	Diffusivity
\dot{H}_{nr}	Non-reversing heat flow in MDSC experiments	$\mathcal{G}_s^\alpha(r, t)$	Self part of the van Hove correlation function for species
\dot{H}_{rev}	Reversing heat flow in MDSC experiments	αN_α	Number of atoms of species α .
ΔH_{nr}	Non-reversing enthalpy in MDSC experiments	$\alpha_2(t)$	Non-Gaussian parameter
C_p''	Imaginary part of the complex heat capacity	$Q(t)$	Overlap function in models for dynamic heterogeneities
$M^*(\omega)$	Imaginary electrical modulus	$f(\mathbf{r}, t)$	Mobility field in models for dynamic heterogeneities
$\sigma^*(\omega)$	Complex electrical conductivity	$g_4(\mathbf{r}, t)$	Four-point correlation function used for the description of dynamic heterogeneities
$S(\mathbf{k}, \omega)$	Dynamic structure factor		
$F_{inc}(\mathbf{k}, t) = F_s(\mathbf{k}, t)$	Incoherent or self intermediate scattering function	$S_4(\mathbf{k}, t)$	Four-point structure factor used for the description of dynamic heterogeneities
$F_{coh}(\mathbf{k}, t)$	Coherent intermediate scattering function	$\chi_4(t)$	Dynamic susceptibility
C_{pm}	Melt heat capacity	ξ_4	Dynamic length scale of dynamic heterogeneities
Δh^*	Activation energy of the Tool–Narayanaswamy–Moynihan model	$R_{SE} \equiv D\eta/T$	Stokes–Einstein ratio
x	Non-linear parameter of the Tool–Narayanaswamy–Moynihan model	$R_{DSE} \equiv \eta/\tau T$	Debye–Stokes–Einstein ratio
T_x	Crystallization temperature	ζ	Parameter characterizing the fractional Stokes–Einstein relation
$\langle r^2(t) \rangle$	Mean square displacement	$\Omega(e_{IS})$	Number of basins of energy e_{IS} in an energy landscape picture
$g(\omega)$	Vibrational density of states		
n_c	Number of topological constraints per atom	t_w	Waiting (aging) time before an experiment is performed
r	Atomic coordination number	T_{eff}	Effective temperature of a non-equilibrium system
f	Density of floppy modes		
\mathcal{F}	Free energy of the rigidity Hamiltonian	$X(t, t_w)$	Fluctuation-dissipation ratio
$q_i^j(T)$	Mauro–Gupta step function in topological constraint theory	ΔH_∞	Maximum enthalpy that can be relaxed in an aging experiment
Δ	Activation energy for broken topological constraints		
T_α	Onset temperature beyond which topological constraints are intact		
β_B	Boron bond-angle constraints		
β_{Si}	Silicon bond-angle constraints		
$P(\theta_{ij})$	Partial bond angle distributions appearing in MD-based constraint counting		
σ_θ	Standard deviation of a partial bond angle distribution $P(\theta_{ij})$		
$\bar{\theta}$	Mean bond angle in MD-based constraint counting		
$\bar{\theta}_k$	Mean bond angle in MD-based constraint counting on individual atoms		
σ_i	Species related (e.g. $i = \text{Ge, Se}$) standard deviations		

Acronyms

AG	Adam–Gibbs
AM	Avramov–Milchev
BB	Bond-bending
BS	Bond-stretching
DSC	Differential scanning calorimetry
ES	Edge-sharing (tetrahedra)
FSDP	First sharp diffraction peak (of $S(k)$)
GK	Green–Kubo
IP	Intermediate phase
IRO	Intermediate range order
IS	Inherent structures
KWW	Kohlrausch–Williams–Watt
MD	Molecular dynamics

mDSC	Modulated differential scanning calorimetry
MYEGA	Mauro–Yue–Ellison–Gupta–Allan
NDF	Neighbor distribution functions
NMR	Nuclear magnetic resonance
OTP	orto-terphenyl
PBAD	Partial bond angle distributions
PCS	Photon correlation spectroscopy
RW	Reversibility window
SLR	Spin lattice relaxation in NMR experiments
TNM	Tool–Narayanaswamy–Moynihan
VFT	Vogel–Fulcher–Tamman

1. Introduction

From glass windows and light bulbs to lenses and fiberglass insulation, advances in glass science and technology have indisputably played a vital role in enabling modern civilization. The performance of every glass product, especially high-technology glasses such as optical fibers, amorphous phase change DVDs or scratch-resistant flat panel displays (including cell-phones) is governed by the underlying properties of the glass at the atomic scale.

What is a glass? This important question is poorly understood, and remains unanswered today beyond the level of general statements, albeit substantial progress in understanding has been made in recent years. Solving this problem represents a great challenge for the science, technology, and engineering communities at large, with obvious technological applications. It has led to intense research activity that spans over vast fields of inquiry, from theoretical physics of liquids to materials science. When a high temperature liquid can be cooled fast enough, it will usually be able to avoid crystallization at the melting temperature T_m and will become ‘*supercooled*’, which represents a thermodynamic metastable state with respect to the corresponding crystal. At very high temperatures, relaxation times to equilibrium are found to be of the order of the typical atomic vibrational period, i.e. of about $\tau = 0.1\text{--}1$ ps, whereas the viscosity η is of the order of $10^{-4}\text{--}10^{-2}$ Pa · s. Once the melting temperature has been bypassed, upon further cooling the viscosity and the relaxation time increase dramatically to reach $\tau \simeq 100\text{--}1000$ s and $\eta = 10^{12}$ Pa · s at a reference temperature that is defined in the literature as the glass transition temperature T_g . This empirical definition simply signals that below T_g , a liquid will be too viscous to flow on a laboratory timescale (i.e. days or years [1]), and the obtained material will be identified with a glass, i.e. a material that displays all the salient microscopic features of a liquid, but has the macroscopic characteristics of a solid. Once a glass has been obtained, there is, however, still thermal evolution towards equilibrium, but its complete experimental study is partially out of reach so that glasses are usually considered as being ‘*out-of-equilibrium*’. As a result, properties will evolve slowly with time, and measurements will depend on the waiting time at which they have begun, a phenomenon known as ‘*aging*’.

Of very special interest is the field of network glasses (figure 1), probably the most familiar and, historically, those which have attracted early interest. This is due, in part, to the

effect of the x-ray determined structure at the local, intermediate or long-range order which appears to be central to the understanding of many chemical physical properties including those revealing the slowing down of the dynamics. Appropriate (stoichiometric) mixtures of Group III–Group V elements (e.g. silicon, boron, germanium, etc) with Group VI oxides and chalcogenides (oxygen, sulphur, selenium) indeed lead to a network structure that is imposed at the very local level by geometrical building blocks typical of a short-range order [3], e.g. the $\text{SiO}_{4/2}$ tetrahedron in silicates. The disordered arrangement of such building blocks on longer scales is then representative of glasses which form a highly cross-linked network of chemical bonds. Addition of alkali and alkaline earth modifiers alter the network structure, and while such elements are usually present as ions, they compensate by attracting nearby non-bridging Group VI atoms which induce a disruption of the network structure. The presence of such non-bridging atoms lowers the relative number of strong bonds in the glass and, in the liquid state, this will lead to an important modification of the melt viscosity, relaxation time, and various dynamic quantities. In fact, an appropriate alloying of such components permits one to tune dynamic quantities of glass-forming liquids in an almost systematic fashion, allowing for the detection of anomalies which provide a greater insight into the glass transition phenomenon.

In this contribution, we review experimental and theoretical methods and studies that have been reported recently on relaxation and aging of network glasses. Because of lack of space, and although some reported features may have an intrinsic interest for the present purpose, we will largely discard the vast body of literature on the relaxation of sphere liquids interacting with very simple potentials that are not ‘*realistic*’ for any physical system. While non-equilibrium processes have been rather well-characterized and some generic behavior revealed from such crude models, the simplified form of the interaction (in short, a repulsive core and an attractive interaction at long distances) is unable to reproduce basic features and structural properties of network glasses which are dominated by specific diffraction patterns for which every detail matters. This makes the correct structural reproduction a prerequisite to any theoretical description. Indeed, for such glasses, aspects of structure control a large part of the dynamics and the relaxation phenomena taking place in the vicinity of the glass transition. However, as emphasized above, glassiness is not restricted to the archetypal silica system and/or to inorganic glasses because sugars, food, organic polymers, and more generally complex disordered systems will display this phenomenon as well, while the glass transition can also be achieved through an appropriate densification, and this indicates that glassy behavior can also be observed under jamming [4].

2. Property changes across the glass transition

Although all quantities remain continuous across the glass transition, rapid changes in physical, thermal, rheological, mechanical, etc properties are observed. As the temperature increases from low temperature to above the glass transition

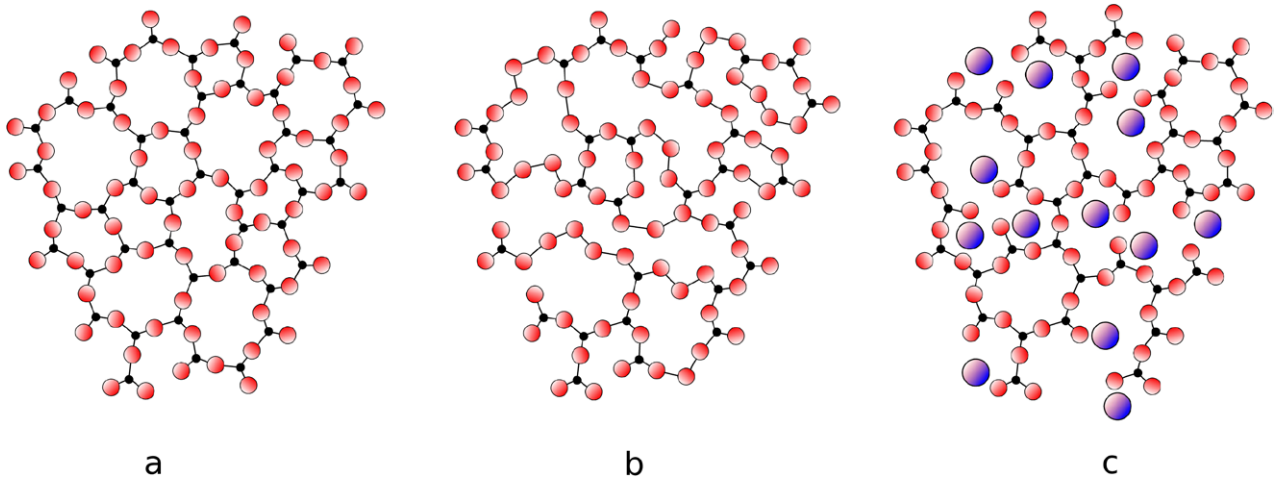


Figure 1. Typical network-forming glasses: (a) a stoichiometric glass former (SiO_2 , B_2S_3) whose structure and network connectivity can be altered by the addition (b) of two-fold coordinated atoms (usually chalcogens, S, Se) that lead to cross-linked chains. The structure can also be depolymerized (c) by the addition of a network modifier (alkali oxides or chalcogenides, Na_2O , Li_2S , etc). Glassy dynamics depends strongly on the network topology, i.e. the way bonds and angles arrange to lead to a connected atomic network. Note, that only chalcogenides can produce a mixture of these three kinds of basic networks, e.g. $(1-x)\text{Ge}_3\text{Se}_{1-y-x}\text{Ag}_2\text{Se}$ [2]. Here, $x = 0$ corresponds to case (b), $y = 33\%$ corresponds to case (c), and both conditions together ($x = 0$, $y = 33\%$) to case (a).

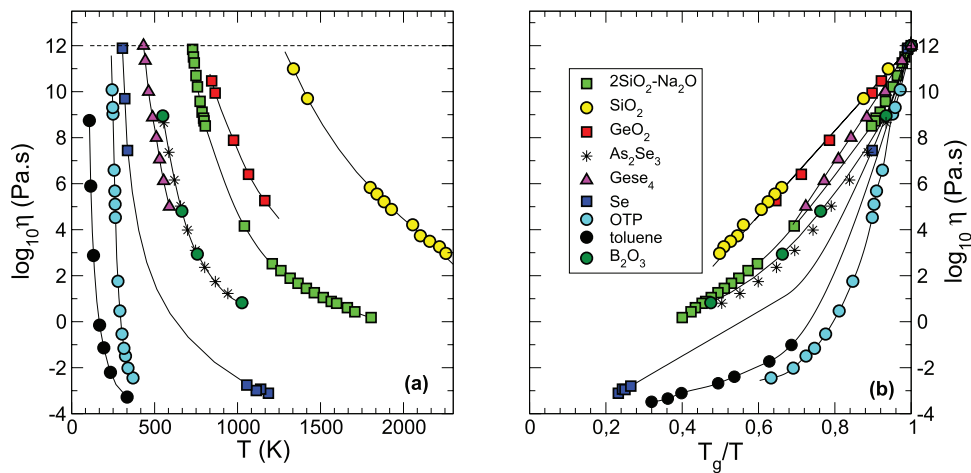


Figure 2. (a) Behavior of the liquid viscosity η of different supercooled liquids as a function of temperature. (b) Uhlmann–Angell plot of viscosity rescaling the same data with respect to T_g/T where T_g is defined by $\eta(T_g) = 10^{12} \text{ Pa} \cdot \text{s}$. Data taken from [5–8].

temperature, many of these properties suddenly change emphatically and manifest, e.g. by important variations in heat capacity, thermal expansion coefficient and/or viscoelastic properties. There are two broad classes of measurements based either on rheological properties (viscosity η and modulus G) or on thermal and thermodynamic properties (enthalpy H , volume V , heat capacity C_p , and expansion coefficient α), the latter usually allowing for a neat measurement of the glass transition temperature T_g from calorimetric/dilatometric measurements, as discussed below.

2.1. Viscosity plots and fragility

The evolution of viscosity (η) is probably one of the most spectacular observed changes as the melt is cooled down to its glass transition. Figure 2(a) represents the evolution of the viscosity for different network-forming liquids (selenium, silica, germania, GeSe_4 , etc) which can be formed in the

supercooled state. These are also compared to other prototypical glass-forming liquids. It can be seen that the increase in viscosity is dramatic for certain substances, and, for organic glass formers such as o-terphenyl (OTP) or toluene, the temperature decrease can lead to a change in η by several orders of magnitude under only tens of degrees temperature change. The behavior of network glass-forming viscosities with T appears to be more moderate, although similar viscosities ($10^{12} \text{ Pa} \cdot \text{s}$) are obtained at a reference temperature T_g that is usually found to be somewhat higher than that of organic glass-forming liquids. This temperature usually serves to rescale the viscosity data in an appropriate plot, initially introduced by Laughlin and Uhlmann [9], and subsequently popularized by Angell [10].

In this plot, the inverse temperature is rescaled with respect to this reference T_g at which the liquid reaches $10^{12} \text{ Pa} \cdot \text{s}$, and the same viscosity data as figure 2(a) are now shown in figure 2(b). An immediate inspection of this figure leads to

the conclusion that such supercooled liquids behave very differently close to their glass transition. Some of them show a behavior $\eta(T)$ that follows an Arrhenius law of the form $\eta = \eta_\infty \exp[E_A/T]$, and typical examples are silica and germania [5] or GeSe₄ [6]. However, as one moves down the figure, other liquids (e.g. B₂O₃, 2SiO₂–Na₂O, As₂Se₃ or Se) now exhibit a viscosity behavior that shows an important bending [6] at intermediate values of T_g/T , whereas organic glass formers (OTP and toluene) display the most pronounced curvature and must involve a super-Arrhenius parametrization of the form $\eta = \eta_\infty \exp[E_A(T)/T]$ where the activation energy E_A must now explicitly depend on temperature.

A simple means to separate liquids for which E_A and the underlying relaxation is independent of temperature from those having an explicit temperature dependence, $E_A(T)$, and exhibiting a rapid increase of η close to $T_g/T = 1$, is provided by the ‘strong’ versus ‘fragile’ classification which permits one to distinguish the two types of behavior [10–12]. This has led to the introduction of a ‘fragility index’ \mathcal{M} which is defined by the slope of $\log \eta(T)$ versus T_g/T at T_g :

$$\mathcal{M} \equiv \left[\frac{d \log_{10} \eta}{dT_g/T} \right]_{T=T_g} \quad (1)$$

As detected from figure 2(b), large slopes will correspond to fragile glass formers displaying an important curvature, a variable $E_A(T)$ and a rapid evolution of η as one approaches T_g , while small slopes (i.e. small \mathcal{M}) will correspond to strong glass formers having a nearly Arrhenius variation involving a constant E_A . Once examined over a wide variety of glass-forming liquids [13], \mathcal{M} is found to vary between a high value [14] of $\mathcal{M} = 214$ for a polymer to a low value [15] of 14.8 for the network-forming liquid Ge₂₂Se₇₈, a value that is actually found to be lower than the usual reported value of silica ($\mathcal{M} = 20$ [13]). Note, also that the terms introduced ‘strong’ and ‘fragile’ are somewhat inappropriate given that they neither connect to underlying mechanical properties, nor to the possible inter-atomic interactions, although most of the strong glass formers have a directional ionic-covalent interaction, but exceptions do exist [16].

Alternatively to the definition (1), several fragility indexes have been introduced to characterize the viscosity behavior of liquids, such as the Bruning–Sutton [17], Avramov [18] and Doremus [16] fragility parameters. All of these attempt to obtain within a single parameter the curvature or slope of the viscosity curves. For instance, the Bruning–Sutton approach [17] prefers to relate the viscosity behavior of supercooled liquids with an apparent activation energy for viscous flow which is either constant (for strong liquids) or highly temperature-dependent for fragile liquids close to the glass transition.

At high temperature, most of the liquids seem to converge to a value that is close to $\eta_\infty = 10^{-4}$ Pa · s. An analysis of viscosity curves [19] using a convenient fitting formula for silicate liquids and other liquids including metallic, molecular, and ionic systems, has shown that the high temperature viscosity limit of such liquids is about $10^{-2.93}$ Pa · s [19]. As there seems to be no systematic dependence of η_∞ on composition, at least for the silicates given the narrow spread around

the average value of $10^{-2.93}$ Pa · s, it is believed that η_∞ has some kind of a universal character. A similar analysis has been performed by Russell and colleagues [20] using alternative fitting formulae for a series of silicate melts, and the prediction of the high temperature viscosity limit has been found to be of about $10^{-4.3 \pm 0.74}$ Pa · s to $10^{-3.2 \pm 0.66}$ Pa · s. While this issue may be considered as secondary for the present purpose, the degree of universality of η_∞ appears to be central to the validity of proposed viscosity fitting formulae (see below) which all assume a universal high temperature limit of viscosity η_∞ to derive the low temperature behavior of $\eta(T)$ close to the glass transition. Given the highly non-linear behavior of viscosity with temperature, the departure from an Arrhenius scaling (figure 2(b)) reflects the influence of the second derivative of η with respect to the inverse temperature that might involve a high temperature parametrized limit embedded in η_∞ , and not only the effect of the low temperature behavior. As seen from equation (1), a non-Arrhenius character can, indeed, be solely parametrized with the fragility index, \mathcal{M} , but the latter is a low temperature quantity representing only a first derivative of the viscosity curve at T_g .

2.2. Fitting functionals

The temperature dependence of the viscosity data (or relaxation time given that one has $\eta = G_\infty \tau$ with G_∞ the infinite frequency shear modulus) is often described approximately by convenient fitting functionals. The most popular one is given by the Vogel–Tammann–Fulcher (VFT) equation [21]:

$$\log_{10} \eta = \log_{10} \eta_\infty + \frac{A}{T - T_0} \quad (2)$$

where A has the dimension of an activation energy, and T_0 a reference temperature that leads to an Arrhenius behavior for $T_0 = 0$. An alternative and perhaps more insightful form of the VFT equation (2) explicitly using the fragility and the glass transition temperature T_g is as follows:

$$\log_{10} \eta(T) = \log_{10} \eta_\infty + \frac{(12 - \log_{10} \eta_\infty)^2}{\mathcal{M}(T/T_g - 1) + (12 - \log_{10} \eta_\infty)} \quad (3)$$

It should be noted that for $T = T_0 < T_g$, the viscosity will become infinite, and this might indicate some sort of phase transition, on which there has been quite some speculation and debate. For instance, it has been stated that T_0 is very close to the Kauzmann temperature T_K [22], a temperature at which the excess entropy of the liquid, with respect to the corresponding crystal, is supposed to vanish. This connects the kinetic view of the glass transition represented by the evolution of $\eta(T)$ with a thermodynamic one. However, this ‘entropy crisis’ is rather counterintuitive because one does not expect the entropy of a glass to be lower than that of the corresponding crystal, given the increased number of accessible states for the former. In addition, neither does one expect, upon further cooling, the entropy of a liquid to become negative as this would violate the third law of thermodynamics. However, apart from the obvious argument stating that an ordered state of matter (the liquid) should not have an entropy lower than

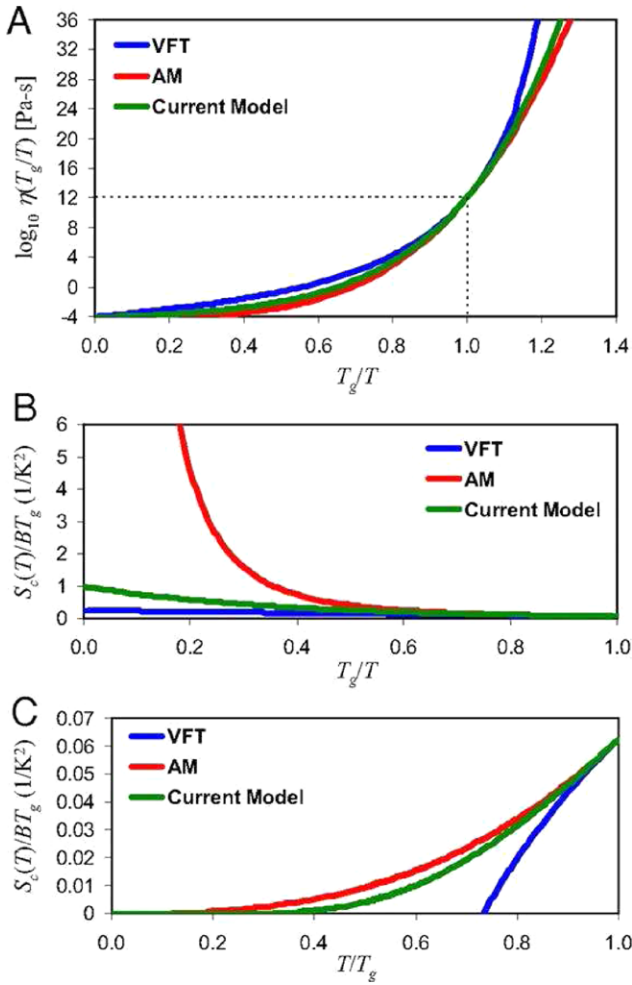


Figure 3. Comparison of different viscosity models [33]. (a) Temperature dependence of viscosity for VFT, (AM) and MYEGA (current) models, assuming $\mathcal{M} = 60$ and $\log_{10} \eta_\infty = -4$. (b) Plot of The Adam-Gibbs exponential argument $S_c(T)/BT_g$ for $T > T_g$. The AM model yields a divergent configurational entropy in the limit of $T \rightarrow \infty$. (c) Plot of $S_c(T)/BT_g$ for $T < T_g$. As already mentioned, the VFT model predicts a vanishing of the configurational entropy at a finite $T = T_0$. Copyright Proceedings of the National Academy of Sciences of the United States 2009.

the corresponding ordered state (the crystal), there is no general principle ruling the various contributions of liquid- and solid-like materials so this apparent paradox may well be consistent with the current experimental observation showing the entropy to vary in a very similar fashion to first derivatives of the free energy, without indication that it extrapolates to zero at some finite temperature.

In a rather systematic study on different glass formers, Richert and Angell [23] have shown that the ratio T_K/T_0 is very close to one for fragile glass formers, but for common network glasses (SiO_2 , GeO_2) which are strong glass formers and have $T_0 \simeq 0$, the fit of the viscosity behavior using equation (2) and its connection to the Kauzmann temperature appears to be inconclusive. However, a fit on Ge–Se liquids using the VFT form has shown that T_0 goes through a minimum for 22% Ge [24], i.e. at the same composition at which a fragility minimum has been measured [15]. Since the discussion about the relationship between T_0 and T_K depends on the functional used

for the viscosity/relaxation time fitting, conclusions regarding the validity of $T_0 \simeq T_K$ can be quite contradictory [25, 26]

An interesting and insightful link between the configurational entropy of the liquid and the relaxation (or viscosity) has been suggested by Adam and Gibbs [27]

$$\eta = \eta_\infty \exp \left[\frac{A}{TS_c} \right] \quad (4)$$

Equation (4), which is central to many investigations of the glass transition (see below), provides an important connection between a kinetic and a thermodynamic viewpoint of the glass transition. In the latter, the configurational entropy variation with decreasing temperature is believed to result from the reduction of the number of possible minima in the complex energy landscape [28–30] characterizing the material. According to this picture, the slowing down of the relaxation, the dramatic increase of τ , result from the reduced ability of the system to explore the landscape in order to locate the energy minimum, driven by the strong reduction of the number of accessible energy minima as the temperature is decreased. Ultimately, structural arrest may occur and, since for an ideal glass at $T = T_K$ one has a single energy minimum only, the configurational entropy vanishes and the relaxation time diverges.

There is actually not necessarily any need to have a functional displaying a diverging behavior at some typical/critical temperature T_0 . Other popular fitting functionals can reproduce the non-exponentiality of the temperature evolution of viscosity, for example the Bässler law [31]:

$$\eta = \eta_\infty \exp \left[\frac{D}{T^2} \right], \quad (5)$$

which yields a curvature in the Angell representation of liquids, or the Avramov–Milchev [32] form:

$$\log_{10} \eta = \log_{10} \eta_\infty + \left(\frac{A}{T} \right)^\alpha \quad (6)$$

where α is the Avramov fragility parameter [18] which is equal to $\alpha = 1$ for strong liquids, whereas liquids with higher α values become more fragile. Most of these models lead to a systematic error when they are extrapolated to low temperatures. A more recent and interesting contribution is due to Mauro and colleagues [33] which provide a viscosity model with a clear physical foundation based on the temperature dependence of the configurational entropy. It offers an accurate prediction of low-temperature isokoms without any singularity at finite temperature. Using the Adam-Gibbs model for viscosity (equation (4)), the configurational entropy can be expressed as a function of topological degrees of freedom [34] (see below) that are temperature-dependent and thermally activated [35], and this leads to the Mauro–Yue–Ellison–Gupta–Allan (MYEGA) equation:

$$\log_{10} \eta = \log_{10} \eta_\infty + \frac{K}{T} \exp \left[\frac{C}{T} \right] \quad (7)$$

which avoids a divergence at low temperature found in the VFT equation (figure 3, equation (7)), and has been tested and compared to alternative viscosity forms (including VFT)

over hundreds of network glass-forming liquids (silicates) and organic supercooled liquids.

Given the huge number of possible compositions and thermodynamic conditions, it is nearly impossible to provide a full database of viscosity measurements for network glass-forming liquids. Useful references are the handbooks of Borisova [37] and Mazurin [38] for oxides and chalcogenides, and the handbook of Popescu on chalcogenides [39]. Instead, we prefer to focus on the forthcoming reported correlations between the fragility index \mathcal{M} and some insightful physical or chemical properties.

2.3. Fragility relationships

2.3.1. Fragility- T_g scaling. An interesting scaling law relating the fragility index to the glass transition temperature is provided by McKenna and colleagues [13]. There is, indeed, conventional wisdom suggesting that fragility increases with the glass transition temperature [10] which implicitly underscores the fact that energy barriers for relaxation increase with increasing T_g .

The derivation of this scaling law combines, for example, the VFT form of equation (2), and the definition of the fragility (equation (1)), and calculates the fragility and the activation energy E_A as a function of the glass transition temperature. One obtains:

$$\mathcal{M} = \frac{AT_g}{(T_g - T_0)^2 \ln 10} \quad (8)$$

and:

$$E_A = \frac{AT_g^2}{(T_g - T_0)^2} \quad (9)$$

Because T_g is of the same order as T_0 , equations (8) and (9) reveal that \mathcal{M} and E_A will scale with T_g and T_g^2 , respectively. Note that this scaling law can also be independently derived from alternative fitting forms for the viscosity, such as the similar Williams–Landel–Ferry form [36].

Using such scaling laws, Qin and McKenna [40] have shown that the correlations (8) and (9) are fulfilled in a large class of hydrogen bonding organics, polymeric and metallic glass formers. All these systems show a linear increase of \mathcal{M} with T_g , and E_A with T_g^2 , whereas network glass formers do not seem to follow such scaling laws. From this study, \mathcal{M} appears to be nearly independent of the glass transition temperature for the reported inorganic glass formers [40]. But, in a systematic study into the composition of chalcogenides, Boolchand and colleagues [15, 41] have demonstrated that this scaling holds in network glasses [40] at select compositions.

Figure 4 represents the behavior of the fragility index \mathcal{M} as a function of measured glass transition temperature T_g for various network-forming glasses. An inspection of $\text{As}_x\text{Se}_{1-x}$ and $\text{Ge}_x\text{Se}_{1-x}$ chalcogenides shows that when the non-stoichiometric melts are followed as a function of tiny changes in composition, the scaling laws (8) and (9) are fulfilled for only selected compositions corresponding to the stressed rigid and

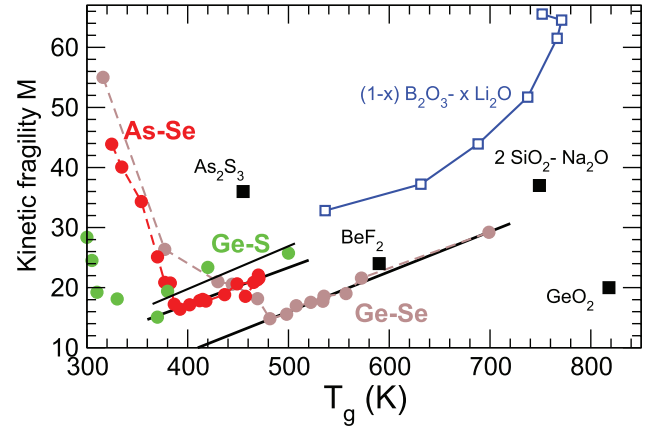


Figure 4. Fragility as a function of glass transition temperature in As–Se (red, [41]), Ge–S [47] and Ge–Se liquids (blue, [15]), together with data for typical network glass formers [13, 44, 45] and binary glasses [46].

intermediate phase compositions (see below) of these glasses [42, 43], i.e. one has a linear increase in $\mathcal{M}(T_g)$ for $x > 22\%$ in Ge–Se [15], and for $x > 27\%$ in As–Se [41]. A least-square fit to such compositions yields to $\mathcal{M} = -7.53(5) + 0.061(7)T_g$ and to $\mathcal{M} = -17.356 + 0.060(1)T_g$ for As–Se and Ge–Se, respectively [41]. The slope of both curves (≈ 0.06) is found to be somewhat lower than the one obtained [40] in polymers (0.28), metallic glass formers (0.17), and hydrogen bonded liquids (0.25).

For low glass transition temperatures (i.e. selenium rich in Ge–Se or As–Se), a negative correlation is found which obviously cannot be accounted for from the VFT equation given that it would lead to unphysical behaviors such as the divergence of relaxation at a temperature $T_0 > T_g$ or an increase in relaxation time τ with temperature [15]. It has been further detected [41] that only the VFT equation (3) can lead to a positive correlation in the scaling law (8). For other fitting formula, such as the simple Arrhenius law $\mathcal{M} = A/T_g \ln 10$ or the MYEGA equation (7), one obtains [41]:

$$\mathcal{M} = \frac{K}{T_g} \left(1 + \frac{C}{T_g} \right) \exp [C/T_g] \quad (10)$$

which decrease as T_g increases. In addition to T_g , \mathcal{M} has also been proposed to correlate to the melting enthalpy ΔH_m [48] and nonpolymeric supercooled liquid shape has been found to display the empirical correlation:

$$\mathcal{M} = \frac{56\Delta C_p T_g}{\Delta H_m} \quad (11)$$

which, similarly to the Adam–Gibbs approach [27] provides another relationship between thermodynamics and dynamics of the glass transition.

2.3.2. Qualitative fragility relationships. In network glass-forming liquids, the fragility index also appears to be deeply related to structural properties. Such a basic observation has been made recently and extensively documented by Sidebottom [49]. By considering a two-state model for the glass

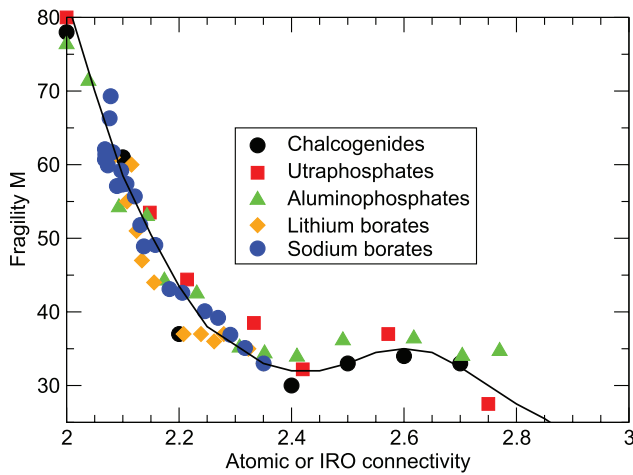


Figure 5. Fragility scaling [49] of various network-forming liquids as a function of connectivity (mean coordination number \bar{r} or mean local connectivity or mean intermediate range order connectivity).

transition separating the intact bond state from a thermally excited broken bond state [50–52], a general variation of the configurational entropy with network connectivity can be proposed. In this model, the fragility index \mathcal{M} is then determined solely by the entropy increase, which is associated with the occurrence of new configurations that become accessible when bonds are broken under temperature increase. For bonds between atomic species [50], the construction can be generalized via a coarse-graining approach to bonds between local structures (such as tetrahedral species in silicates [53]) or even bonds between intermediate range order (IRO) structures that are found in borates [54]. A generic behavior of the index \mathcal{M} variation is obtained (figure 5) which demonstrates a universal dependence of the glass-forming fragility on the topological connectivity of the network. For the special case where intermediate range order is present, the coarse-graining procedure to a bond lattice indicates that the weakest links (i.e. those which connect IRO) are the most relevant in determining the liquid fragility.

Building on a similar idea, large scale molecular dynamics simulations of network-forming liquids [55] show that aspects of topology and IRO control the relaxation of the liquid. Here, the network topology is changed by varying the anion polarizability [56] of the interaction potential, which governs the intertetrahedral bond angle, and, ultimately it is shown that the fragility is correlated to structural arrangements on different length scales. In particular, \mathcal{M} is found to increase with the number of edge-sharing (ES) tetrahedral motifs in tetrahedral glass-forming liquids. For the special case of Ge-X ($X = \text{S}, \text{Se}$) systems, however, the link between edge-sharing tetrahedra and the fragility index does not follow such a correlation [47, 57]. A direct measurement of \mathcal{M} and the ES fraction from Raman spectroscopy indicates that the trend in the fragility index is essentially governed by the underlying topology, and, in particular, by aspects of rigidity (see below).

An alternative viewpoint is proposed by Luther-Davies and others [58, 59] who emphasize the role played by chemical order, and especially by deviation from stoichiometry, rather

than topology or rigidity. A joint spectroscopic and fragility experiment is analyzed in terms of network dimensionality and stoichiometry change. It is suggested that fragility does not follow predictions from rigidity percolation (in As–Se) but instead correlates with structural dimensionality, whereas for the ternary As–Ge–Se a minimum in fragility is claimed to be associated with a maximum in structural heterogeneity consisting of appropriate ratios of Se-chains and $\text{GeSe}_{4/2}$ tetrahedra. This claim is actually contradicted by the early work of Angell and collaborators, highlighting the connection between topology/rigidity and fragility index in the same chalcogenide liquid (Ge–As–Se [8]). The minimum in \mathcal{M} has been obtained at the network mean coordination number $\bar{r} = \langle r \rangle = 2.4$ which is the location of a rigidity percolation threshold [60, 61]. The correlation with chemical order is also debated by Boolchand and others who have emphasized the link between fragility minima and isostatic compositions [15, 41, 47], i.e. compositions that are close to the rigidity percolation threshold. This link between topology and fragility is also evidenced by the investigation of ionic diffusion and fragility on a series of iron-bearing alkali–alkaline earth silicate glasses [62].

2.3.3. Fragility: structure relationships. Glass fragility is also found to display a relationship with atomic ordering on intermediate and extended ranges, a relationship that also connects to the notion of dynamic heterogeneities (see below). Specifically, the structure can be characterized in terms of topological and chemical ordering from neutron diffraction experiments in real (pair correlation function $g(r)$) and reciprocal space (static structure factor $S(k)$) [63]. It transpires that the ordering for GeO_2 , SiO_2 and ZnCl_2 at distances greater than the nearest neighbor lengthscale can be rationalized in terms of an interplay between the relative importance of two length scales [64]. One of these is associated with an intermediate range that is directly accessed from the structure factor $S(k)$; the other lengthscale is associated with an extended range that is characterized from the decay of Bhatia–Thornton pair correlation functions in real space. With increasing glass fragility, i.e. when moving from GeO_2 to ZnCl_2 , it has been found that the extended range ordering dominates [64].

Having such simple structural correlations at hand, it is not surprising that glassy relaxation has also been investigated by diffraction methods in order to follow low wavevector features with temperature, and, specifically, the first sharp diffraction peak (FSDP) of the structure factor $S(k)$. It has been stated [10] that fragile liquids usually do not have any structural signature of long-range correlations so that the absence of an FSDP is indicative of a fragile glass-forming liquid. This correlation has been verified on a certain number of systems such as the very fragile ZrO_2 and Al_2O_3 [65] which do not exhibit an FSDP, in contrast with the less fragile ZnCl_2 which shows a well-defined, but not sharp, FSDP [66], and with other examples of strong glass-forming liquids such as germania and silica which display a sharp FSDP [67, 68].

By analyzing the typical features of the simulated structure factors with changing thermodynamic conditions (density, composition), Bauchy and Micoulaut [69–71] have found

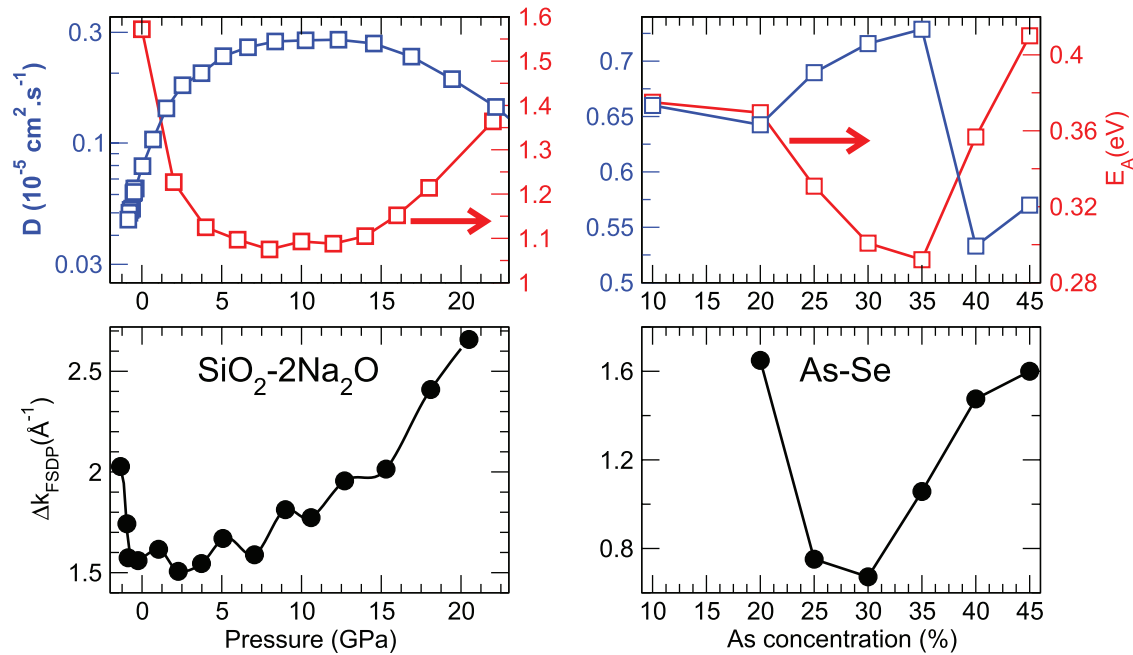


Figure 6. Correlation between relaxation properties, calculated diffusivity D (blue) and activation energy E_A for diffusivity (red axis of the upper panels), and structural properties in the glassy state (black curve, width Δk_{FSDP} of the FSDP) in systems with changing pressure ($2\text{SiO}_2\text{-Na}_2\text{O}$, [69, 70], left panels) or changing composition (As-Se, [71], right panels). Note, that for As-Se, an opposite behavior for Δk_{FSDP} with composition is found from a reverse Monte Carlo simulation [72].

that anomalies (extrema) in properties associated with glassy dynamics (diffusivity D , activation energy E_A which is proportional to fragility if T_g does not vary too much) are correlated with anomalies in structural features, as revealed by the change in FSDP (peak position k_{FSDP} and width Δk_{FSDP} , figure 6). The established correlation suggests that in strong glasses, typical length scales of distance $L = 2\pi/k_{\text{FSDP}}$ involved in the slower variation of viscosity with T_g/T must lead to a growth of the FSDP because the latter reflects some repetitive characteristic distance between structural units. Also, the broadening of the FSDP is indicative of a correlation length (Scherrer equation [73]) defined by $2\pi/\Delta k_{\text{FSDP}}$ that tends to maximize for strong glass-forming liquids (figure 6, bottom).

2.3.4. Other fragility relationships. Network glass-forming fragilities display a certain number of other correlations with physical, chemical or rheological properties that have been reported in the literature.

An inspection of figure 2 also indicates that supercooled liquids with a lower fragility index \mathcal{M} will lead to higher viscosities at a fixed T/T_g . It has been observed [74] that the glass-forming tendency is increased for liquids that are able to increase their melt viscosity at lower temperatures, i.e. for a given class of materials having a similar T_g , the glass-forming tendency is increased for melts with lower fragilities: this argument is particularly relevant for binary alloys. Indeed, in eutectics where freezing-point depressions exist, glasses will form more easily because these depressions bring the liquid to lower temperatures and higher viscosities, while preventing from crystallization. Such observations are, furthermore, found to correlate rather well when the composition of the eutectic is compared to compositions at which one has a

minimum of the critical cooling rate that is needed in order to avoid crystallization [75].

Correlations have been suggested between fragility and non-exponentiality ($\exp(-t/\tau)^\beta$) of the structural relaxation characterized by a Kohlrausch exponent β [76] at low temperature and long durations. Here, τ represents the relaxation time. These have been established [44] from a combination of experimental techniques (figure 7). When all subgroups of glass formers are represented (organic, polymers, networks) a clear relationship appears and indicates that the fragility index \mathcal{M} decreases with the exponent β , i.e. as one moves towards the Debye-type one-step relaxation limit ($\beta = 1$), the fragility reaches its minimum value ($\mathcal{M} < 20$). A correlation of fragility to the non-ergodic level of the glass has been also found in the liquid phase as measured directly by dynamic light scattering [77]. Other authors have emphasized the central role played by elastic properties such as compressibility [78]. Novikov and Sokolov [79] have shown that the fragility of a glass-forming liquid is directly linked to the ratio of the instantaneous bulk and shear moduli, or the Poisson ratio. Since the latter is related to the very local deformations of the cage structure made by neighboring atoms, these authors argue that the Poisson ratio should also control the non-ergodicity parameter which controls the fast dynamics of the liquid. However, this result has been challenged [80], and evidence has been provided that \mathcal{M} should, in fact, scale with the ratio of the transverse and longitudinal sound velocity. Building on a similar relationship, Ruocco and colleagues [81] have emphasized that the fragility should be linked with the elastic properties of the corresponding glass, quantified from the non-ergodicity parameter f_c accessed from inelastic x-ray scattering (inset of figure 7).

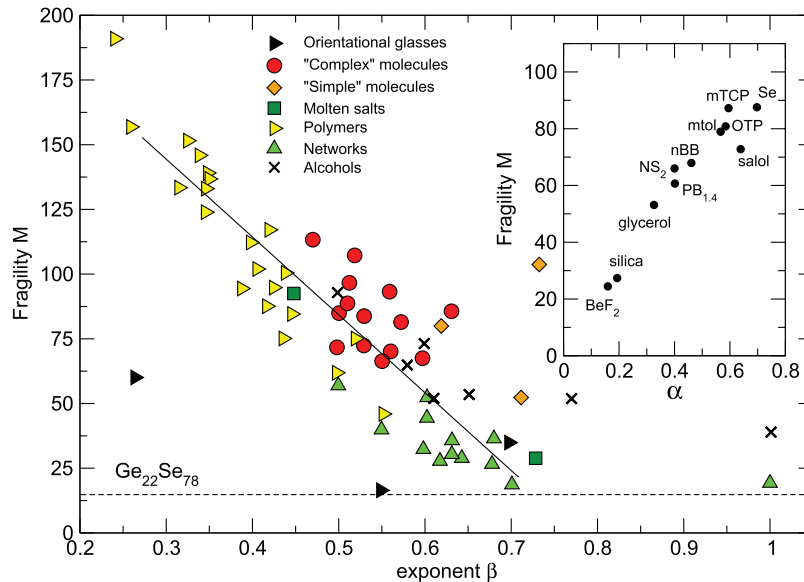


Figure 7. Correlations between fragility \mathcal{M} and some physical properties. Fragility of various glass formers (collected from [44, 46, 47]) as a function of the Kohlrausch stretching exponent β . Minimum fragility \mathcal{M} of $\text{Ge}_{22}\text{Se}_{78}$ [15] is represented by a broken line. The inset shows a correlation between fragility and a parameter (α) characterizing the non-ergodicity factor $f_c(T)$ (collected from [7, 81, 82]) via $f_c(T) = (1 + \alpha(T/T_g))^{-1}$.

Some other authors have also proposed an empirical relation between the fragility and the strength of fast dynamics which can be quantified from Raman spectroscopy of corresponding glasses [83, 84]. According to this idea, the ratio of the relaxational to vibrational contributions around the Boson peak has been proposed to relate to the fragility of the liquid. This relationship has been also challenged and no such correlation could be recovered [85] from a careful Raman analysis. It should be stressed that most of these correlations are proposed from a literature survey of a variety of glasses, allowing large ranges in fragility to be covered (see y-axis in figure 7). However, when the focus is only on the network-forming inorganic liquids which have typically $\mathcal{M} < 70$, the correlation becomes less obvious because of the reduced fragility index range. It would certainly be instructive to quantitatively test such correlations for the wide subclass of network glasses.

It must finally be stressed that proposed relationships are often based on melt fragility indexes that can sometimes be flawed by improper sample preparation, especially for strong liquids which have the highest viscosities (e.g. GeSe_4). A careful study [86] of the effect of melt homogeneity on the measurement of \mathcal{M} shows that inhomogeneous melts can lead to a spread in measurements, and, eventually, to improper established correlations. The variance of the measurement decreases as glasses homogenize (figure 8), whereas the mean value increases to saturation at values characteristic of homogeneous glasses [15, 41].

2.4. Stress relaxation

Given their disordered atomic structure and their out-of-equilibrium nature once $T < T_g$, glasses exhibit residual frozen stresses. This is because atoms are randomly placed in the network, and this situation is energetically unfavorable, at

least with respect to a regular crystalline lattice. These stresses can be partially released by moderate temperature annealing, a technique known by the ancient Phoenicians, that prevents stress-induced cracking, and the related relaxation can therefore represent an alternative and interesting way to probe the dynamics of a glass or a deeply supercooled liquid through its glass transition [89–91].

When a material is subjected to a constant strain, there is a gradual decay in the stress that can be analyzed as a function of time, and reveals the viscoelastic properties as a function of thermodynamic conditions [92]. Note, that for glasses with a low glass transition temperature (chalcogenides), aspects of viscoelasticity can also be probed at room temperature. In practice, relaxation is embedded in a relaxation function $\Phi(t)$ that relates the relaxing stress/strain behavior to its initial value, provided that the strain is imposed in an instantaneous fashion at $t = 0$.

A certain number of experiments have shown that such measured relaxation functions $\Phi(t)$ can be conveniently fitted with a stretched exponential that seems to decay to zero at $t \rightarrow \infty$ (figure 9) for most of the inorganic glasses, in contrast with cross linked polymers [93] or crystals [94] which decay to a finite stress/strain value. The detail of the analysis [95] also shows that during relaxation the viscoelastic deformation under stress can be decomposed into a sum of an elastic part, an inelastic (or viscous) part and a delayed elastic part; the latter being responsible for the non-linear primary creep stage observed during creep tests. In addition, such a delayed elasticity has been found to be directly correlated to the dispersion of relaxation times of the processes involved during relaxation.

Measurements using different methods have been made on, for example, Ge–Se [96–98], Te–As–Ge [99], and As–Ge–Se [100], which can be related to structural aspects, while also

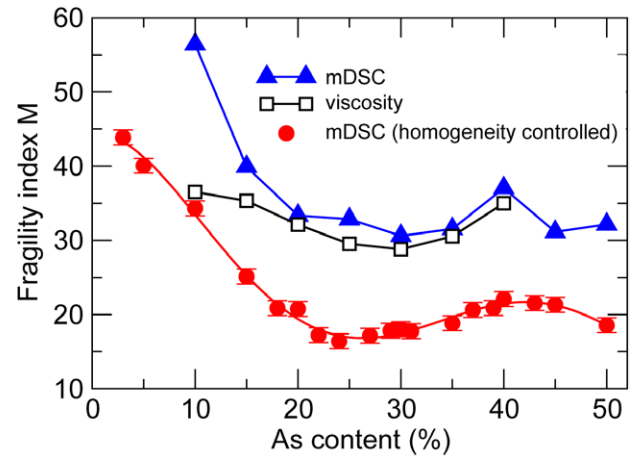
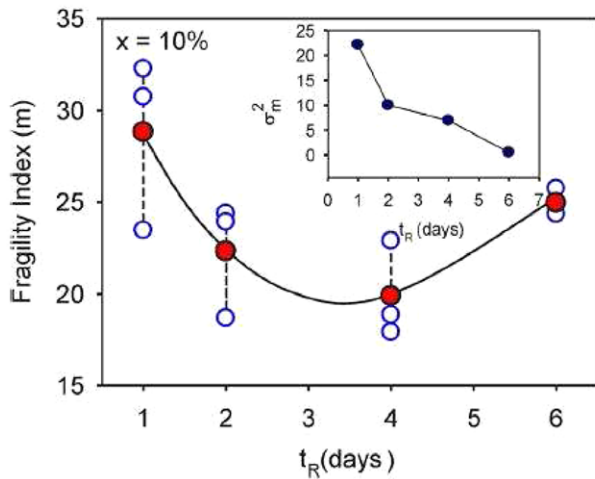


Figure 8. Effect of glass homogeneity on fragility measurements [86]. Left: effect of the reaction time t_R on the fragility index M in $\text{Ge}_{10}\text{Se}_{90}$. Symbols indicate measurements on different batch parts, whereas the red circles indicate batch average. The inset shows the spread of the measurement (variance σ_M as a function of t_R). Permission from John Wiley & Sons 2015. Right: compositional variation of the fragility index M of the As–Se system, and the effect of measurement type (mDSC [41, 87]; viscosity [88]) and sample homogeneity. Using the same measurement method, glasses with Raman verified homogeneity [57] lead to lower fragilities (red symbols, [41]). Permission from AIP Publishing LLC 2015.

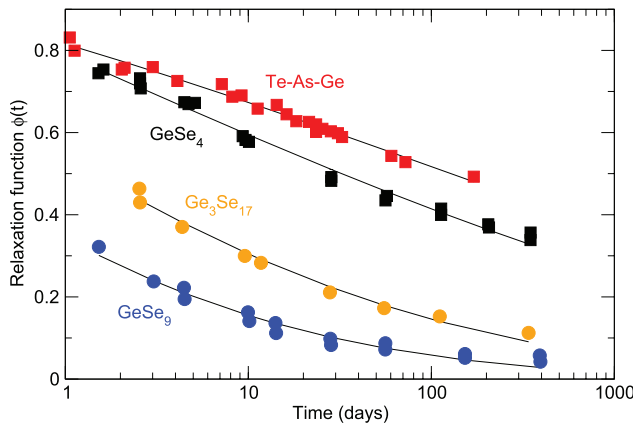


Figure 9. Relaxation function $\Phi(t)$ in Ge–Se and Te–As–Ge glasses from stress relaxation measurements [97]. Lines represent fits using a stretched exponential $\exp[-(t/\tau)^\beta]$ function.

revealing that a significant part of the stress is not released on experimental timescales (months) in certain compositions for given systems (e.g. GeSe_4 in Ge–Se [97]). Such stress relaxation measurements have some importance in the field of ion exchange glasses (e.g. sodium borosilicates) because of the strengthening of the glass surface that is steadily improved [101, 102]. It has also been considered for soda-lime [92, 103, 104] or borosilicate glasses [105]. For the latter [105], a long-time study has permitted the first detectable signatures of glass relaxation far below T_g ($T/T_g \approx 0.3$), and the measure of strain with time, in other words the relaxation of the glass, follows a stretched exponent with a Kohlrausch exponent $\beta = 0.43$ that has been predicted from dimensional arguments [106].

In the case of chalcogenides, an interesting perspective is provided by the comparison with the generic behavior of organic polymers [93] since amorphous Se is considered as a glassy polymer made of long chains that are progressively cross-linked by the addition of alloying elements. Stress

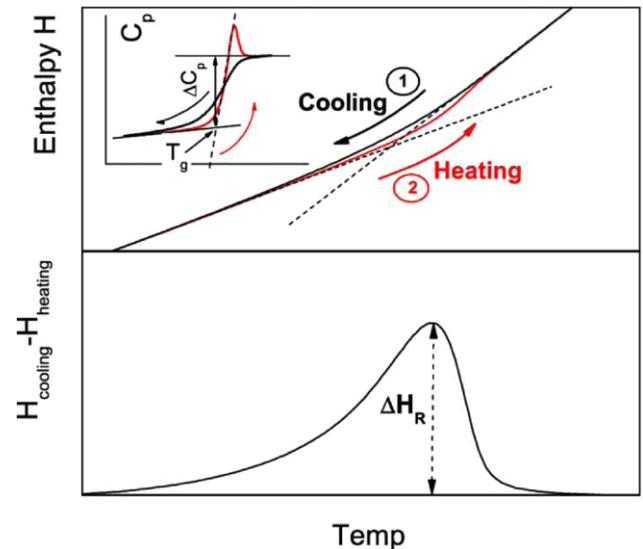


Figure 10. A schematic plot of thermal properties (enthalpy H) at the glass transition [108]. When fast enough, cooling from the high temperature melt avoids crystallization, leading to the supercooled liquid and, ultimately, to a glass at a certain fictive temperature (crossover of the broken curves). Upon reheating (red curve), a hysteresis appears that is related to the relaxation of the glass. Corresponding heat capacity during cooling and subsequent heating without annealing, covering enthalpy relaxation in glass states, and subsequent enthalpy recovery (bottom) upon glass transition. Permission from AIP Publishing LLC 2015.

relaxation is also thought to have some impact on the resistance drift phenomena [107] which is crucial for the functionality of heavier chalcogenides such as amorphous phase-change tellurides ($\text{Ge}_2\text{Sb}_2\text{Te}_5$).

2.5. Thermal changes

Signatures for the onset of glassy behavior can be also detected from thermal changes.

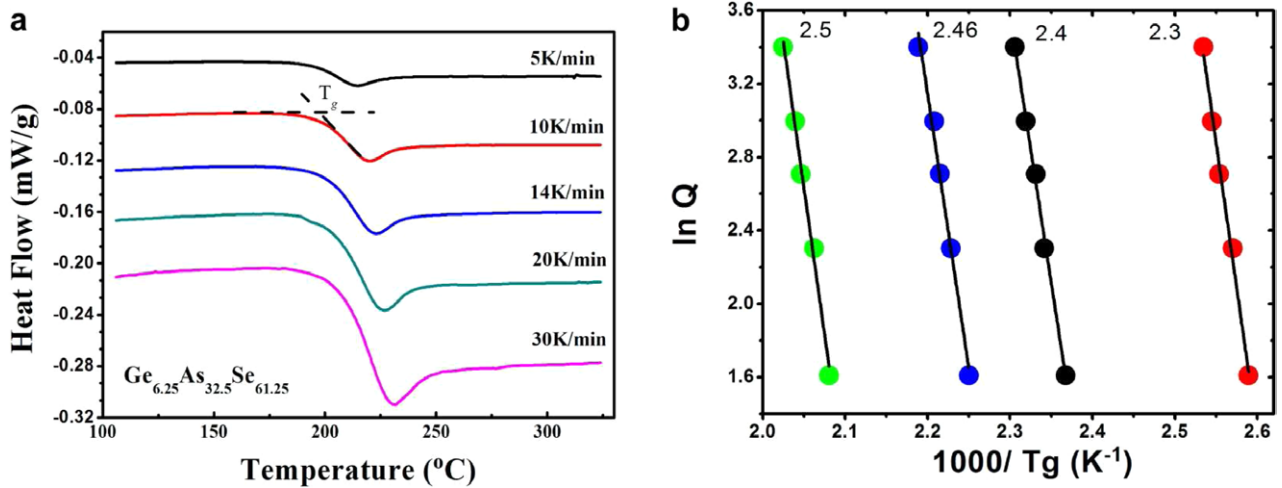


Figure 11. (a) DSC curves [58] showing the total heat flow \dot{H}_{tot} of a ternary Ge_{6.25}As_{32.5}Se_{61.25} glass obtained for changing scan (heating) rates q^+ from 30 K min⁻¹ to 5 K min⁻¹. (b) Plot of $\ln q^+$ as a function of $1000/T_g$ for different glasses in this ternary As–Ge–Se. A linear fit leads to values for E_A , using equation (13). Reprinted with permission from [58].

2.5.1. General behavior. Figure 10 shows a typical behavior of the enthalpy from the high temperature liquid down to the glass. A rapid cooling from the melt avoids crystallization at the melting temperature and brings the liquid into the supercooled regime. As the equilibration cannot proceed further on computer or experimental timescale (see below) given the rapid increase of the relaxation time, the enthalpy curve (or the volume curve) deviates from the high temperature equilibrium line at the fictive temperature T_f which depends on the cooling rate. A faster cooling rate will lead to a higher fictive temperature, whereas a lower cooling rate will produce a lower fictive temperature because equilibration can be achieved down to lower temperatures. As both enthalpy and volume display a different slope below or above the fictive temperature, their derivative with respect to temperature (heat capacity, thermal expansion, inset of figure 10) will lead to an abrupt change with a step-like change across the glass transition that depends on the cooling rate.

However, even in the obtained glassy state, the material will continue to relax to a lower energy state leading to lower volumes or lower enthalpies. As mentioned above, these relaxation processes happen on timescales that now exceed the laboratory timescale by several orders of magnitude. As a result, the enthalpy/volume curve upon reheating (red curve) will be markedly different, and this effect can even be enhanced if the glass is maintained at some waiting temperature T_w for a certain time (days, weeks, years), allowing for an increased relaxation. This experimental situation corresponds to physical aging, and it can also be detected from the heat capacity or thermal expansion change. Calorimetry permits the tracking of such effects (relaxation and aging) and when the heat capacity is measured during an upscan (red and black curves in figure 10) a hysteresis loop appears, which also causes a heat capacity overshoot at the glass transition. This endotherm peak simply reveals that previously frozen degrees of freedom during the quench are now excited so that the overshoot is a direct manifestation of the relaxation taking place between the laboratory temperature, or the temperature T_w at which the

glass is aged, and T_g . As a result, an enthalpic recovery (ΔH_R in figure 10 bottom) can be measured upon reheating. Note, that due to this kinetic nature, the glass transition temperature T_g cannot be uniquely defined by, for example, calorimetry, and its value differs slightly from the reference temperature satisfying $\eta(T_g) = 10^{12}$ Pa · s.

In addition, extrinsic factors due to the kinetic character of glass transition must be taken into account. For instance, the effect of the heating rate on glass transition temperature dependence is rather well documented in the literature, and obeys the phenomenological Kissinger equation [109]:

$$\frac{d \ln(q/T_g^2)}{d(1/T_g)} = -\frac{E_A}{R} \quad (12)$$

or, alternatively, the Moynihan equation [110]:

$$\frac{d \ln q}{d(1/T_g)} = -\frac{E_A}{R} \quad (13)$$

which translates, via the assumption of an activated process with energy E_A for the relaxation kinetics of the glass transition, into a higher rate leading to a higher measured T_g . Under the assumption that the activation energy involved in equations (12) and (13) is the same as the one involved in the relaxation of the viscous liquids, a measurement of T_g at different scan rates q leads to a determination of the fragility for strong glass formers via $\mathcal{M} = E_A / \ln_{10} RT_g$. Applications of such methods to network glasses can be found for a variety of glasses (e.g. Ge–As–Se [58] using equation (13), figure 11). Note, that the fragility determination from the Kissinger equation might be subject to considerable uncertainty. Instead, methods incorporating the effect of the fictive temperature and cooling rate can give reliable values, quite comparable with the viscosity-based fragility measurements [111, 112].

In the literature, a vast body of data exists on such measurements given that T_g is generally determined by calorimetry which measures the change in thermodynamic properties (heat capacity) at the glass transition.

3. Experimental methods

3.1. Scanning calorimetry

The most frequently used technique for determining the glass transition temperature and studying enthalpy relaxation is differential scanning calorimetry (DSC). The technique measures a difference between an electrical power needed to heat a sample at a uniform scan (heating) rate. As the measured heat flow, once the reference signal has been removed, is proportional to C_p of the system, one has access to the heat capacity across the glass transition in order to investigate effects such as those represented in figure 10(b).

For DSC, one usually uses the definition for T_f for the enthalpy:

$$H(T) = H_e(T_f) - \int_T^{T_f} C_{pg}(T_f) dT_f \quad (14)$$

where C_{pg} is the heat capacity of the glass, and $H_e(T_f)$ is the equilibrium value of H at the fictive temperature. One then has access to the heat capacity by differentiating the equation to obtain:

$$\frac{dT_f}{dT} = \frac{[C_p - C_{pg}]_T}{[C_{pe} - C_{pg}]_{T_f}} \simeq \frac{[C_p - C_{pg}]_T}{\Delta C_p} = C_p^N \quad (15)$$

where C_p^N is the normalized heat capacity, and it is often assumed that ΔC_p calculated at the fictive temperature is the same as at temperature T so that dT_f/dT equals C_p^N . In practice, these DSC signals are scan rate dependent given that the glass transition temperature depends on the heating rate (figure 11).

3.2. AC calorimetry and modulated DSC

The first introduction of this technique (AC calorimetry) came from Birge and Nagel who added onto the DSC linear signal a small oscillation [113–115]. It represents an interesting extension since enthalpy relaxation can be measured in the linear region of small temperature changes, thus avoiding possible non-linear responses of the sample. However, most applications have focused on organic liquids such as glycerol [113], and we are not aware of any measurements for network glass-forming liquids.

From a statistical mechanics viewpoint, one can consider the imaginary part of the heat capacity, $C_p^*(i\omega)$, as a complex response function (similar to the dielectric permittivity $\epsilon^*(i\omega)$, see below), and this part is usually associated with the absorption of energy from an applied external field. This frequency-dependent heat capacity is complex, a property that is a direct consequence from the fluctuation-dissipation theorem which applies to a function that is proportional to the mean-square fluctuations in entropy, $k_B C_p = \langle S^2 \rangle$, which in turn have a spectral distribution. Birge [115] suggests that in AC calorimetry there is no net exchange of energy between the sample and its surroundings, but there is a change in the entropy of the surroundings that is proportional to C_p , and the second law of thermodynamics ensures that $C_p > 0$.

Kob and colleagues [116] have given a statistical mechanics description of AC calorimetry by deriving a relationship

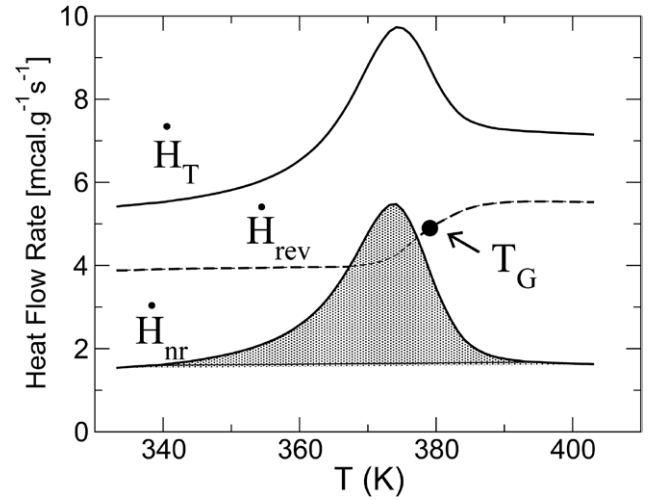


Figure 12. mDSC scan of a $\text{As}_{45}\text{Se}_{55}$ glass showing the deconvolution of the total heat flow \dot{H}_{tot} into a reversing and non-reversing part (\dot{H}_{nr}). The area between the setup baseline and \dot{H}_{nr} permits one to define a non-reversing enthalpy ΔH_{nr} . Adapted from [42].

between the frequency-dependent specific heat and the auto-correlation function of temperature fluctuations. Using molecular dynamics simulations of silica, they have shown that both real and imaginary parts of C_p exhibit the usual shape of complex response functions, the out of phase (imaginary) component displaying a maximum corresponding to the typical α -relaxation peak at $\omega_{\text{max}}\tau = 1$. The dependence of τ on temperature has been found to agree with the one determined from the long-time (α -relaxation) behavior of the incoherent scattering function. This indicates that AC calorimetry, and its extension to modulated differential scanning calorimetry (mDSC), can be used as a spectroscopic probe for structural relaxation in glasses [117, 118].

An improved technique, mDSC, appeared nearly two decades ago, and represents a promising extension of [113], with frequency ranges being reduced by several decades. It allows for investigations of thermal conditions with increased relaxation times, close to the glass transition. This technique is somewhat versatile since measurements are performed in the course of a usual DSC scan. It is thus likely to offer a new convenient way to probe molecular mobility in connection with relaxation. In practice, and as in AC calorimetry, one superposes a sinusoidal variation on the usual linear T ramp of the form $T(t) = T_{\text{disc}}(t) + \sin(\omega t)$. In direct space, this technique permits one to deconvolute [119, 120] the total heat flow (\dot{H}_{tot}) into a reversing and a non-reversing component. The reversing component (\dot{H}_r) tracks the temperature modulation at the same frequency ω while the difference term (renamed as ‘non-reversing’), $\dot{H}_{\text{nr}} = \dot{H}_{\text{tot}} - \dot{H}_r$ does not, and captures most of the kinetic events associated the slowing down of the relaxation close to the glass transition (figure 12). The decomposition into several heat flow components can be formally written as:

$$\dot{H}_{\text{tot}} = \dot{H}_{\text{rev}} + \dot{H}_{\text{nr}} = C_p(T)\dot{T} + f(t, T) \quad (16)$$

where \dot{H}_{rev} and \dot{H}_{nr} represent the reversing heat flow and the non-reversing heat flow, respectively. The function $f(T, t)$ contains most of the time and temperature-dependent processes.

When studying the glass transition, this function becomes important when one reaches the transition temperature, because the system needs more and more time to equilibrate upon temperature change, and this is, in fact, observed in the example displayed (figure 12). Frequency corrections can be realized to provide a nearly independent measure of C_p and its inflexion point serves to determine the glass transition temperature. When properly placed with respect to the measurement baseline, the area \dot{H}_{nr} leads to the definition of a non-reversing heat enthalpy (ΔH_{nr} , figure 12) that has some importance in the field of rigidity transitions (see below). The complex heat capacity $C_p^*(\omega)$ can be linked to the sinusoidal part of the heat flow response contained in both contributions of \dot{H}_{tot} , either through the base frequency (\dot{H}_{rev}) or through the secondary harmonics (\dot{H}_{nr}).

In order to probe the dynamics ranging from a very short timescale of pico-to-nanoseconds typical of high temperature, to the low temperature domain of μs to seconds, different sets of experiments can be used, and these comprise neutron scattering, dielectric and calorimetric spectroscopy. These methods can be seen as complementary given that they do not probe the same timescale; the former essentially focusing on the high temperature regime when τ is very small.

In an mDSC measurement, a decomposition of the complex $C_p^*(\omega)$ into real and imaginary parts leads to curves which have the characteristic forms of the complex susceptibility of a relaxation process (figure 13(a)), as also accessed from dielectric measurements. In particular, for a given temperature the imaginary part C_p'' peaks at a frequency $\omega_{max}\tau = 1$ which permits one to access the relaxation time, and this calorimetric method has been shown to lead to similar results regarding $\tau(T)$ when compared to dielectric data [117, 118]. When such determined relaxation times $\tau = 1/\omega_{max}$ are represented in an Arrhenius plot close to the glass transition, the T dependence of $\tau(T)$ permits determining the fragility (figure 13(b)).

3.2.1. Dielectric relaxation. Similarly to mDSC, dielectric relaxation permits, via the response of the system to an external and oscillating electric field, the provision of information about the relaxation behavior. The complex permittivity $\epsilon^* = \epsilon' - i\epsilon''(\omega)$ can be studied as a function of frequency, and the imaginary part $\epsilon''(\omega)$ (the loss spectra) which also peaks at $\omega_{max}\tau = 1$ can be conveniently fitted in the high temperature regime (Debye) as well as in the supercooled regime using empirical functions (Havriliak–Negami [121], Cole–Cole [122]) to access the relaxation time as a function of thermodynamic conditions, and, particularly, temperature.

While this technique has largely been used for the study of organic glass formers [123–125] due to their increased dielectric strength, the study of network glasses has been mostly restricted to solid electrolytes containing modifier ions (Na, Li,...). In this case, a measurement of the complex conductivity $\sigma^*(\omega)$ permits one to determine, *via* the electrical modulus $M^*(\omega)$, the frequency behavior of the permittivity [126]:

$$\epsilon^*(\omega) = \frac{1}{M^*(\omega)} = \frac{\sigma^*(\omega)}{i\omega\epsilon_0} \quad (17)$$

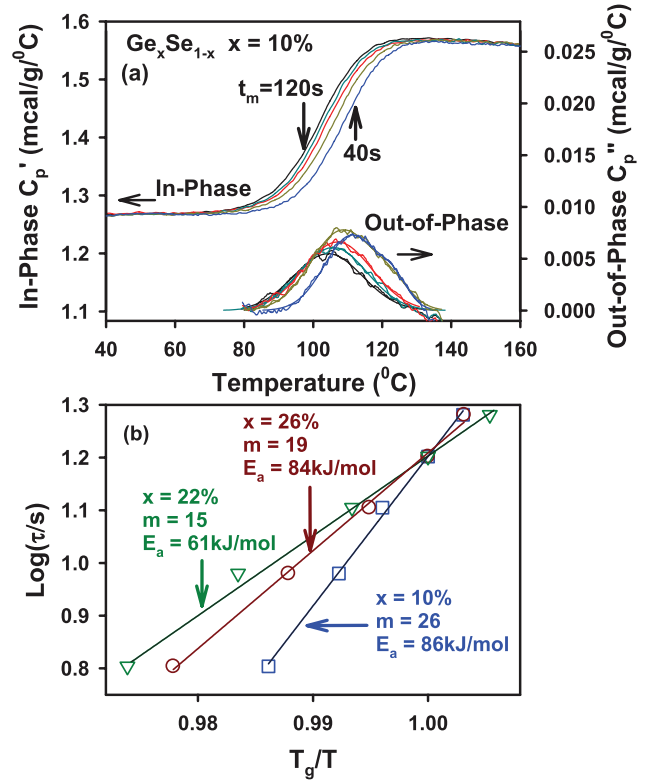


Figure 13. (a) An example of *in-phase* and *out-of-phase* components of complex C_p from mDSC scans as a function of modulation frequency for a $\text{Ge}_x\text{Se}_{100-x}$ melt at $x = 10\%$ [15]. (b) Log of relaxation time (τ) as a function of T_g/T yielding fragility, m , and activation energy E_a from the slope of the Arrhenius plots at indicated compositions (x). Permission from AIP Publishing LLC 2015.

Again, the frequency ω_{max} at which the out-of-phase component $\epsilon''(\omega)$ is maximum leads to a determination of the relaxation behavior of the ions, and related characteristics of glassy relaxation (β , E_A ,...). Typical applications to silicate [127, 128], borates [129–131], thioborates [132], germanates [133], and phosphates [134] can be found in the literature.

3.2.2. Scattering functions. Given the same timescale (ns), inelastic neutron scattering experiments can provide direct access to relaxation functions that can be compared with statistical calculations using molecular simulations (see below). Measured double differential cross-sections are proportional to so-called scattering functions $S(\mathbf{k}, \omega)$ which, via Fourier transform, can be related to the intermediate scattering function $F(\mathbf{k}, t)$. The coherent and incoherent parts of the scattering function allow the determination of a coherent part of the intermediate scattering function $F_{coh}(\mathbf{k}, t)$ providing information about collective particle motion:

$$F_{coh}(\mathbf{k}, t) = \frac{1}{N} \sum_{i=1}^N \sum_{j=1}^N \langle e^{i\mathbf{k} \cdot \mathbf{r}_i(0)} e^{-i\mathbf{k} \cdot \mathbf{r}_j(t)} \rangle, \quad (18)$$

and an incoherent (self) part $F_{inc}(\mathbf{k}, t)$ that focuses on single particle motion:

$$F_{inc}(\mathbf{k}, t) = F_s(\mathbf{k}, t) = \frac{1}{N} \sum_{i=1}^N \langle e^{i\mathbf{k} \cdot \mathbf{r}_i(0)} e^{-i\mathbf{k} \cdot \mathbf{r}_i(t)} \rangle \quad (19)$$

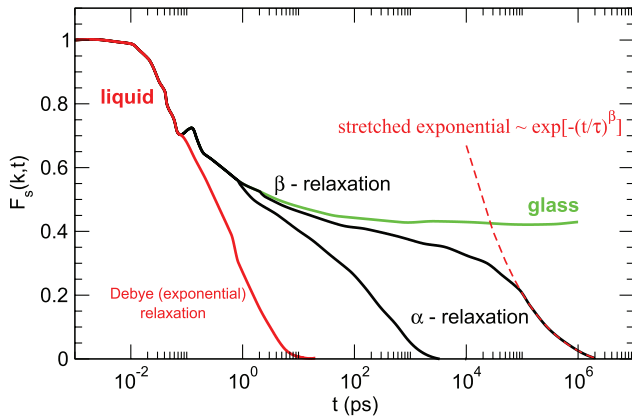


Figure 14. Schematic representation of density correlation function (intermediate scattering or incoherent scattering function) $F_s(k, t)$ in viscous liquids at different temperatures: high temperature liquid (red) with a simple exponential decay, deep supercooled (glass, green), and intermediate temperatures (black) displaying both the β -relaxation plateau, and the α -relaxation regime which can be fitted by a stretched exponential of the form $\exp[-(t/\tau)^\beta]$.

The latter, which follows the Fourier components of density correlations, characterizes the slowing down of the relaxation that can be investigated in liquids for different temperatures down to a temperature close to the glass transition.

Such correlation functions (e.g. $F_s(\mathbf{k}, t)$) display some salient features for most of the glass formers (figure 14). At high temperature, $F_s(\mathbf{k}, t)$ decays in a simple exponential way of Debye type that only takes into account the interactions between particles (microscopic regime), and $F_s(\mathbf{k}, t)$ goes to zero rather rapidly, typically the ps timescale for, say, a silicate liquid at 1800 K (see figure 15). For smaller times, smaller than the typical microscopic times (ps), the time dependence is quadratic in time and arises directly from the equation of motion of the moving atoms. As the temperature is decreased, however, the decay of $F_s(\mathbf{k}, t)$ cannot be described by a simple exponential function, and a plateau sets in at longer times. The time window associated with this plateau is called the ' β -relaxation' and this window increases dramatically as the temperature continues to decrease, driven by the cage-like dynamics of the atoms which are trapped by slow-moving neighbors. This leads to a nearly constant value for density correlations in Fourier space, and is associated with a non-ergodicity parameter f_c characterized by the plateau value $F_s(k, t) \simeq f_c$ in the β -relaxation regime. However, for times which are much larger than this β -relaxation regime, atoms can escape from the traps, can relax, and jump to other atomic traps so that $F_s(\mathbf{k}, t)$ can eventually decay to zero (figure 15), and its behavior is appropriately described by a stretched exponential of the form $F_s(\mathbf{k}, t) \simeq \exp[-(t/\tau)^\beta]$ where τ is the (structural) relaxation time associated with the so-called ' α -relaxation' regime, and β is the Kohlrausch parameter introduced previously. For a full review on the stretched exponential and the nature of the parameter β , we refer the reader to [106]. It should be noted, however, that while the stretched exponential is a convenient fitting form of the long time limit of $F_s(\mathbf{k}, t)$, this does not imply that the glassy dynamics are only non-exponential. In fact, the relaxation dynamics are

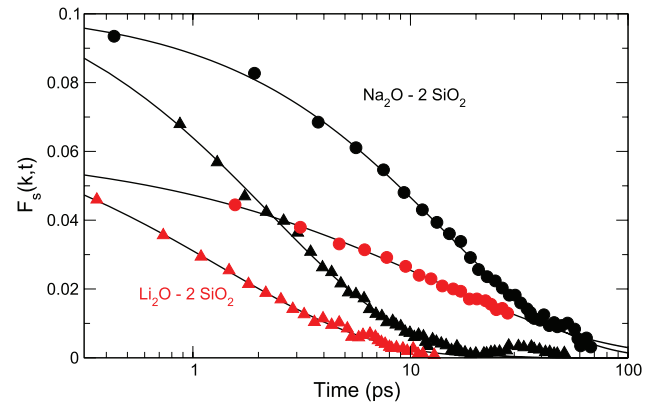


Figure 15. Density correlation functions of $F_s(q, t)$ of sodium and lithium disilicate melts (1600 K, [82]) in the fast alkali relaxation regime at different wavevectors k (circles, $k = 0.4 \text{ \AA}^{-1}$; triangles, $k = 1.0 \text{ \AA}^{-1}$). The solid lines represent fits with a stretched exponential function.

also non-linear given that the structure keeps changing with time and temperature. Therefore, the application of the simple Kohlrausch form which only emphasizes the non-exponential aspect might not be accurate enough to explain the full relaxation dynamics.

As one finally approaches the glass transition, because of the dramatic increase of the relaxation time τ , this α -regime becomes barely observable, and the β -relaxation plateau extends to timescales which are of the order of the typical laboratory timescale or larger (green curve in figure 14).

There has been quite a large body of research on inelastic neutron scattering applied to the determination of the glassy dynamics in supercooled liquids. For networks, Kargl *et al* [82] have used inelastic scattering in alkali silicate liquids to determine the viscous dynamics, the relaxation time $\tau(T)$ and the non-ergodicity parameter f_c . It has been found that in such liquids fast relaxation processes happen on a 10 ps timescale (accessed from a neutron time of flight experiment) and are associated with the decay of the Na–Na structural correlations, whereas slower processes are found on a 10 ns timescale, and involve the decay of network-forming species-related coherent correlations (Si–O, O–O and Si–Si). Such an observation is actually quite systematic for binary modified glasses which contain an alkali modifier, and a certain number of examples of such investigations can be found in the literature (e.g. sodium aluminosilicates [135]).

3.2.3. Nuclear magnetic resonance. The investigation of nuclear magnetic resonance (NMR) spectra as a function of temperature and/or composition also permits access to properties of relaxation [136]. The typical time of spin-lattice relaxation (SLR) can be used to link the dynamics of certain structural fragments resolved by NMR with timescales related to the SLR time. This time is, indeed, associated with the mechanism that couples the equilibration of magnetization for a given linewidth (i.e. a local structure) with the effect of the (lattice) neighborhood.

In the liquid state, the evolution with temperature of the site associated linewidth and their characteristics (e.g. full width

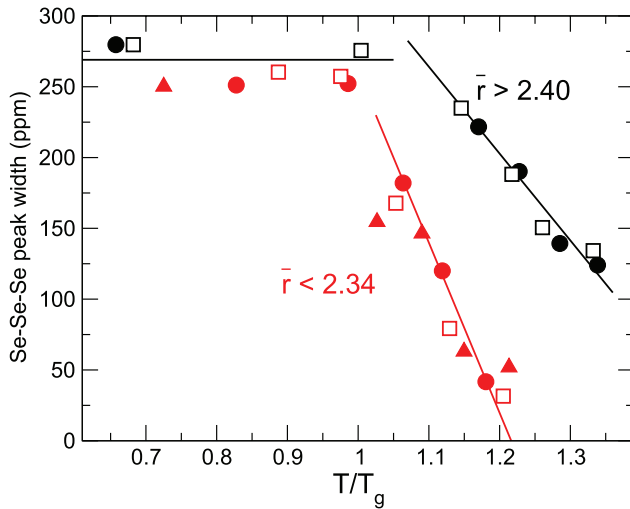


Figure 16. Full width at half maximum of a ^{77}Se NMR resonance associated with Se–Se–Se chains as a function of temperature in $\text{Ge}_x\text{Se}_{1-x}$ glass-forming liquids [137]. Systems have been separated into subclasses satisfying the mean coordination number $\bar{r} = 2 + 2x \geq 2.4$ or $\bar{r} \leq 2.34$. Here, $\bar{r} = 2.4$ represents the rigidity percolation threshold [61].

at half maximum) provide direct indication of how structural fragments impact the evolution with time and temperature [137–141]. Linewidths are expected to narrow upon temperature increase, and since such linewidths can be associated with specific structural features or species, one can have access to aspects of relaxation, and how the local structure affects the dynamics. For instance, for the case of silicate species [138], it has been found that the typical NMR timescale involved in Na cation exchange between Si tetrahedral species was identical to the one determined from viscosity measurements. This indicates that the local Si–O bond-breaking represents the main contribution to viscous flow in silicate liquids. A similar conclusion has been drawn for borosilicates [142], and represents the central result related to this topic, i.e. the investigation of glass relaxation from NMR studies.

In the glassy state, applications to chalcogenides (Ge–Se) have shown that such SLR timescales are significantly smaller for Se–Se–Se chain environments (10^{-9} s) as compared to Ge–Se–Ge fragments (10^{-6} s, [143, 144]), and consistent with the fact that these chains are mechanically flexible, and lead to an enhanced ease to relaxation that is also driven by composition (figure 16). However, an opposite behavior is found for a similar system (As–Se, [145]); such contradictory trends being eventually driven by the magnitude of the applied magnetic field, and how the corresponding frequency compares to the characteristic timescale for dipolar coupling fluctuations [144].

3.2.4. Photoelectron correlation spectroscopy. There is also the possibility to use photon correlation spectroscopy (PCS) to probe the dynamics of the glassy relaxation [146] in order to extend the measurement of correlation functions to the μs s time domain, i.e. close to the glass transition. Another more recent powerful experimental technique using x-ray induced photoelectrons has also emerged thanks to instrumental developments [147], and to an increased flux and coherence of

x-ray beams. For a full review on the technique, see [148]. At present, the development and the first applications of the technique have mostly focused on metallic glasses [149–151]. It has been found that for such systems the dynamics evolve from a diffusive atomic motion in the supercooled liquid, to stress-dominated dynamics in the glass, characterized by a complex hierarchy of aging regimes.

In the case of network glasses, only select yet promising studies have been reported on liquid selenium [152], silicates both in glasses [153, 154] and deep supercooled liquids [155], and phosphates [156, 157]. In the silicates, it has been found that even at 300 K both lithium and sodium silicate glasses are able to relax [153] and rearrange their structure on a length scale of a few Angstroms, thus contradicting the general view of almost arrested dynamics. The measured relaxation time has been found to be surprisingly fast, even hundreds of degrees below T_g , a result that contrasts with the common idea of ultra-slow dynamics, but which is consistent with the measured relaxation behavior [105] of a borosilicate glass far from the glass transition temperature ($T/T_g \simeq 0.3$). The findings also seem to suggest the existence of distinct atomic scale-related relaxation dynamics in glasses, not taken into account by any previous study.

In the binary phosphates $\text{Na}_2\text{O-P}_2\text{O}_5$, Sidebottom and colleagues [156] have analyzed the relaxation of the glass-forming liquids, and have shown that the substantial increase in fragility is accompanied by a progressive depolymerization of the network structure, suggesting that the viscoelastic relaxation in network-forming liquids is controlled only by the topology of the covalent structure. Similar to the case of silicates [135], a decoupling of ionic motions from those of the network species seems to occur as the glass transition is approached.

4. Simple models for enthalpic relaxation

4.1. Tool–Narayanaswamy–Moynihan equation

Probably the simplest way to quantify enthalpic relaxation due to physical aging and structural relaxation is provided by Tool’s concept of fictive temperature [158] which permits definition of the enthalpy of a glass as a function of T_f :

$$H(T, T_f) = H(T_0, T_f) + \int_{T_0}^{T_f} C_{\text{pm}}(T) dT + \int_{T_f}^T C_{\text{pg}}(T) dT \quad (20)$$

where C_{pm} and C_{pg} are specific isobaric heat capacities of the metastable supercooled melt and the glass, respectively, and T_0 is an arbitrary sufficiently high reference temperature at which the system is in a metastable thermodynamic equilibrium. Narayanaswamy generalized Tool’s model [159] by incorporating a distribution of relaxation times, and obtained the following expression for the fictive temperature that can be calculated for any thermal history:

$$T_f(t) = T(t) - \int_0^t dt_1 \left(\frac{dT}{dt} \right)_{t_1} M_H[y(t) - y(t_1)] \quad (21)$$

where M_H is the Kohlrausch–Williams–Watts (KWW) relaxation function introduced previously:

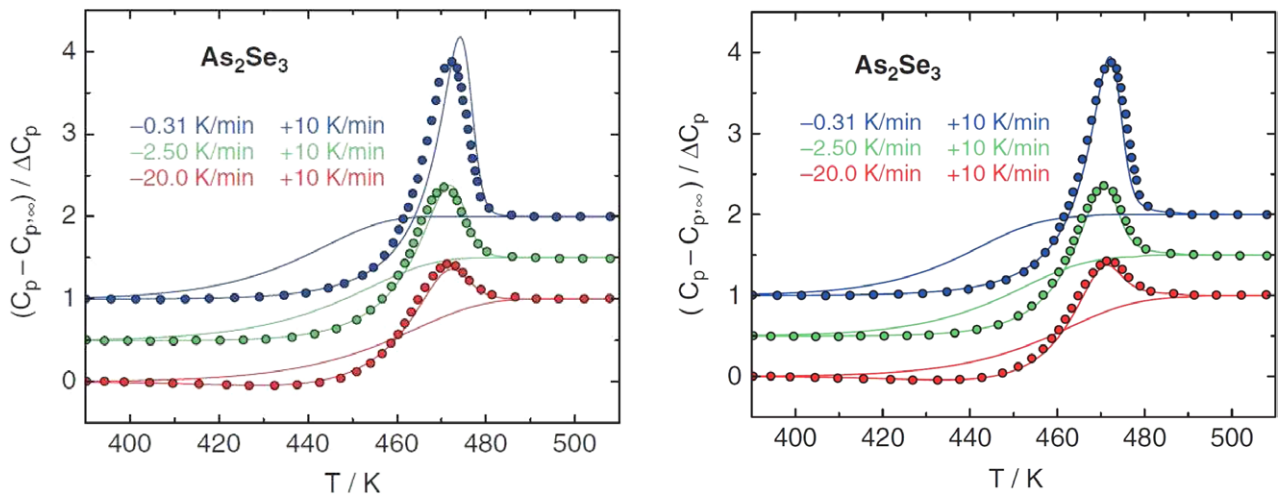


Figure 17. Plot of normalized heat capacity C_p for As_2Se_3 with temperature for cooling rates of -0.31 , 2.5 , and 20 K min^{-1} and heating at a common rate of $+10 \text{ K/min}$. Left: direct TNM modeling [160]. Right: TNM modeling using heterogeneous dynamics with a distribution of relaxation times [161]. Symbols are the experimental DSC data taken from [160]. Permission from AIP Publishing LLC 2015.

$$M_H(y) = \exp[-y^\beta] \quad (22)$$

and, as for the case of the long-time behavior fitting of the intermediate scattering function, the Kohlrausch exponent β ($0 < \beta < 1$) characterizes non-exponentiality. The function M_H is supposed to be inversely proportional to the width of a distribution of relaxation times of independent relaxation processes, y being a dimensionless reduced relaxation time:

$$y(t) = \int_0^t \frac{dt_1}{\tau(t_1)}. \quad (23)$$

The contribution to the relaxation time $\tau(T, T_f)$ is controlled by a non-linearity parameter x ($0 < x < 1$) according to the Tool-Narayanaswamy-Moynihan (TNM) equation:

$$\tau = \tau_0 \exp \left[\frac{x \Delta h^*}{RT} + \frac{(1-x) \Delta h^*}{RT_f} \right] \quad (24)$$

where τ_0 is a constant, Δh^* is an apparent activation energy, and R is the universal gas constant. Having set these equations, the time evolution of the normalized molar heat capacity can be obtained and directly compared to the standard output of a DSC measurement.

The combination of these equations (20)–(24) with Boltzmann superposition (i.e. the Tool–Narayanaswamy–Moynihan (TNM) phenomenology) is the most frequently used non-linear phenomenology for the study of enthalpy relaxation.

4.1.1. Applications. There are many applications of the TNM phenomenology to network glasses using either DSC signals for enthalpic relaxation, or dilatometric measurements for volume relaxation (see figure 17).

Enthalpic structural relaxation in $\text{As}_x\text{Se}_{100-x}$ glasses from DSC has been described within this TNM model [162], and connections can be made with structural changes. A combination of mercury dilatometry and DSC [163] on certain network glasses ($\text{Ge}_2\text{Se}_{98}$ and $\text{As}_2\text{Se}_{98}$) using, again, the TNM model shows that enthalpic and volumetric relaxation are nearly identical and

lead to the same Δh^* value, which is also the case for elemental selenium. In this series of selenide network glasses, there has been a lot of attention [164–167] on the relaxation of pure Se whose network is made of long Se chains [168]. The TNM parameters (pre-exponential factor τ_0 and the apparent activation energy Δh^*) have been found to be very close to the activation energy of viscous flow. Other typical applications of the TNM model to the analysis of enthalpy/volume relaxation can be found for B_2O_3 [169], Ge-Sb-Se-Te [170], $\text{Ge}_{15}\text{Te}_{85}$ [171], As_2S_3 [172] or $\text{Ge}_{38}\text{S}_{62}$ [173] or Te-Se [174].

4.1.2. Limitations. One obvious drawback is that the TNM parameters (β , Δh^* , x) do not seem to be fully independent as emphasized by Hodge [175]. The TNM parameters of 30 organic and inorganic glass formers have been collected, and a strong correlation between the parameters emerges (figure 18). It is suggested [176] that these correlations are somehow expected because the fitting parameters are not orthogonal in parameter search space, and because the TNM parameters themselves have large uncertainties that are also correlated. In addition, there is obviously a lack of a physical model that could provide an interpretation for the parameter and the parameter correlations, the explicit account of a KWW behavior (equation (22)) also being introduced by hand in the theory. Also, relatively subtle distortions of the experimental data can lead to evaluated TNM parameters that are highly inconsistent.

One way to circumvent these problems is to provide other indirect fitting methods allowing one, for instance, to evaluate the apparent activation energy of enthalpic relaxation Δh^* from the heating rate dependence, using the Kissinger formula (12) in combination with a determination of the fictive temperature using the equal enthalpic area method across the glass transition [169, 177]. Additional indirect fitting techniques [110] use the shift of the relaxation peak with the temperature during so-called intrinsic cycles of the glass transition during which the cooling-to-heating ratio is kept constant. For more details on alternative fitting techniques, see [178–180].

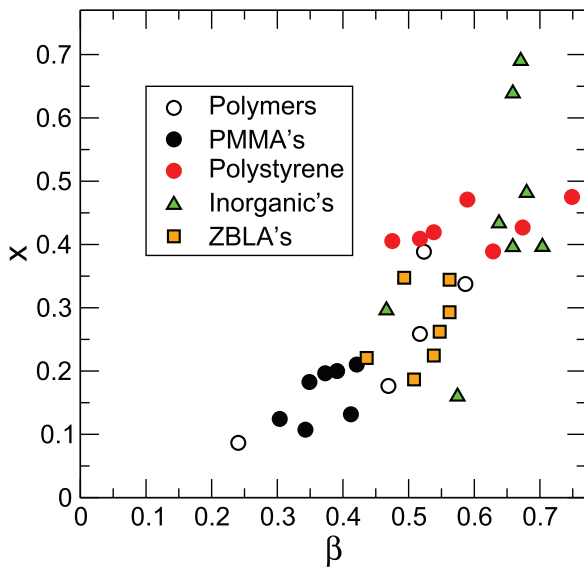


Figure 18. Plot of TNM parameters showing the x versus β correlation indicating the possible correlation between fitting parameters for various glass-forming systems: polymers, polystyrenes, inorganics, fluoropolymer (ZBLA), PMMA. Adapted from [175].

Application to certain glassy selenides (e.g. $\text{Ge}_2\text{Sb}_2\text{Se}_5$) shows that a full account of the enthalpic relaxation cannot be achieved from the TNM equation. While the results exhibit a significant dependence on experimental conditions, part of the TNM parameters do need to be confirmed by such alternative methods [181].

Other important limitations concern the case of the poor reproduction of huge overshoot peaks that manifested after extremely long annealing periods, a failure that may result from the simple exponential behavior for τ (equation (24)). This problem can be solved by assuming heterogeneous dynamics of dynamically correlated domains which relax in an exponential fashion and almost independently from each other [161]. In this case, the enthalpic overshoot for a DSC up-scan is substantially improved (figure 17, right) with respect to the basic modeling [160] using equations (20)–(24). Also, the TNM framework does not account for multiple glass transition temperatures that are found in heterogeneous glasses or in glasses having a reduced glass-forming tendency, i.e. with $\Delta T = T_x - T_g$ quite narrow, T_x here the crystallization temperature which leads to a strong endotherm peak in DSC signals. More references and examples on the TNM model limitations can be found in [182–186].

A comparative method introduced by Svoboda and Malèk [187] builds on the parameter control of the TNM approach through the cycling of all possible theoretically calculated datasets with different relaxation curve profiles. This opens up the possibility of applying the TNM equations even to extremely distorted differential scanning calorimetry data [188].

4.2. Adam and Gibbs theory

Such modeling procedures are actually consistent with other simple thermodynamic approaches as emphasized in some

examples (e.g. selenium [189]). For moderate departure from equilibrium, it has, indeed, been shown that volume and enthalpy relax in the same way when analyzed from the TNM approach or from the Adam-Gibbs model which relates the relaxation time to the configuration entropy of the liquid.

As emphasized above, this Adam-Gibbs (AG) model [27] has a rather large importance in the field of glass transition because it relates the relaxation time towards equilibrium, a crucial quantity in the context of glassy relaxation, with the thermodynamic properties and the accessible states for the liquid. In the initial approach, it is assumed that relaxation involves the cooperative rearrangement of a certain number z of particles. This involves a transition state activation energy between at least two stable configurations so that the configurational entropy S_c must satisfy $S_c \geq k_B \ln 2$. The configurational entropy can be exactly calculated under the additional assumption that (i) the size of these cooperative arranging regions is independent, and (ii) that these represent equivalent subsystems of the liquid, and are linked with the relaxation time. One then obtains equation (4). Such a deep and interesting connection between transport coefficient and entropy has been verified directly, i.e. by representing dynamic properties, e.g. diffusivity, as a function of A/TS_c in a semi-log plot from computer simulations of water [190, 191] silica [192] or OTP [193] (figure 19, left). It can also be obtained from a simultaneous measurement of both the viscosity/diffusivity and the heat capacity in silicates [194–198] and water [199], given that one has:

$$S_c = \int_{T_K}^T \frac{\Delta C_p(T)}{T} dT \quad (25)$$

where T_K represents the Kauzmann temperature at which the entropy vanishes (figure 19). In simulations, S_c has been determined mostly from a general thermodynamic framework taking into account the vibrational contributions [200] from quenched inherent structures (see below). In the experimental determination for the validity of the AG relation, S_c is determined from calorimetric measurements of (i) the crystal heat capacity from low temperature up to the melting temperature T_m , (ii) the enthalpy of melting of the crystal at the melting point, and (iii) the heat capacity of the supercooled liquid from T_m to low temperature. It is found that equation (4) is satisfied in several families of silicate melts (figure 19 right). Note, that such studies have also been realized in fragile organic glass formers [201]. The Adam-Gibbs expression (4) linking τ with the configurational entropy gives a good account of the non-linearity observed in enthalpy relaxation of amorphous polymeric, inorganic, and simple molecular materials near and below T_g [175]. Equation (4) can also be modified if a hyperbolic form is assumed for the heat capacity [202] which seems to be fulfilled in selected glass-forming systems. In this case, S_c behaves as $C/(1 - T_2 - T)$ [203, 204], and leads directly to a VFT behavior (equation (2)) that has $T_2 = T_0 = T_K$ [23, 25, 26]. This simple Adam-Gibbs picture [27], although powerful, contains a certain number of obvious limitations that have been discussed in, for example, [205] (see also the above discussion on $T_0 \simeq T_K$). For instance, the rearrangement

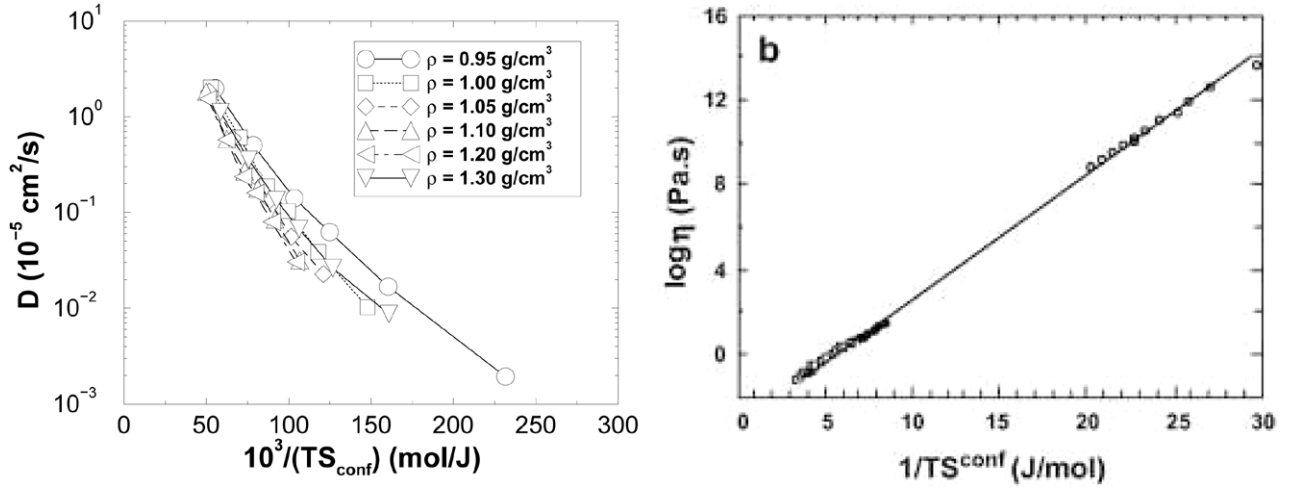


Figure 19. Verification of the Adam-Gibbs relation. Diffusivity or viscosity of liquids plotted as a function of $1/TS_c$ in simulated densified water [191] (left) or experimentally measured silicates [194] (right). Permission from Elsevier 2015.

of cooperative regions is not restricted to supercooled liquids given that such phenomena also take place in crystals with diffusion of correlated vacancies or interstitials. Similarly, the emergence of divergent length scales, as revealed by the growing heterogeneous dynamics setting when one approaches T_g , is in contradiction with the assumption of independent and equivalent regions.

4.3. Harmonic models

An alternative path for the description of glassy relaxation is given by the wide class of kinetic constraint models for which the thermodynamics is trivial, but not the dynamics. Complicated dynamics emerge from local time-dependent rules, and are able to reproduce some of the standard phenomenology of the glass transition. Among these models, the simplest one can be based on the linear elasticity of the glass and the corresponding interaction can be considered as harmonic.

4.3.1. Kirkwood–Keating approach. The justification of the applicability to covalent amorphous networks can be made on the basis of the Kirkwood–Keating interaction potential that has been introduced to fit elastic and vibrational properties [206–208]. It represents a semi-empirical description of bond-stretching and bond-bending forces given by

$$V = \frac{3\alpha}{16d^2} \sum_{i,j} (\mathbf{r}_{ij} \cdot \mathbf{r}_{ij} - d^2)^2 + \frac{3\beta}{8d^2} \sum_{k(i,i')} \left(\mathbf{r}_{ki} \cdot \mathbf{r}_{ki'} + \frac{1}{3}d^2 \right)^2 \quad (26)$$

where α and β are bond-stretching and bond-bending force constants, respectively, and d is the strain-free equilibrium bond length. Such models have been widely used for the realistic modeling of structural (figure 20) and electronic properties of tetrahedral amorphous networks [209, 211, 212], and these simple interaction potentials have also been used to investigate the glass transition phenomenology [213–216]. A certain number of salient features can be recovered within Metropolis dynamics (see next section). The interaction potential can be assimilated with a simple harmonic model

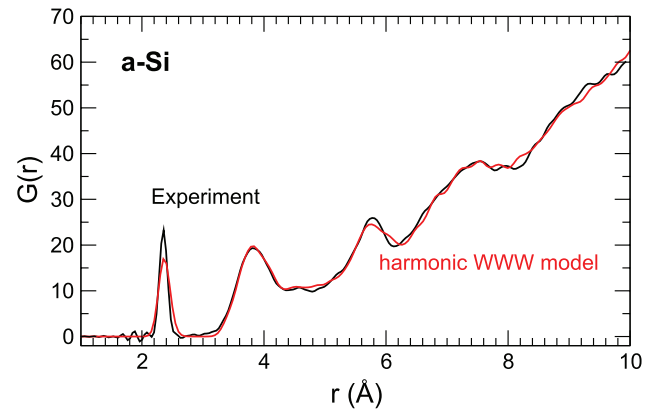


Figure 20. Radial distribution function of amorphous silicon [209] modeled using equation (26), and compared to experiments [210].

written as: $V = (m/2) \sum_i \omega^2 x_i^2$ where ω represents a typical vibrational mode related to bond interactions, and inelastic neutron scattering studies of glasses [217–219] give information about the order of magnitude of the typical stretching and bending vibrational frequencies (energies), typically of about 20–40 meV.

4.3.2. Metropolis dynamics. From these simplified cases [213, 214], the non-trivial dynamics of such potentials (as in equation (26)) can be obtained as follows. Once equation (26) is reduced to the simple harmonic form, changes in atomic positions from x_i to $x'_i = x_i + r_i/\sqrt{N}$ for all i are accepted with probability 1 if the energy decreases, i.e. if $\delta V = V(\{x'_i\}) - V(\{x_i\})$ is negative. Otherwise, the change is accepted with a Metropolis rule $\exp(-\beta\delta V)$. Here, $\{r_i\}$ is a random variable having a Gaussian distribution of zero mean and finite variance equal to Δ^2 . A Gaussian integration [213] leads to the probability distribution $P(\delta V)$ for an energy change δV :

$$P(\delta V) = (4\pi m \omega^2 V \Delta^2)^{-\frac{1}{2}} \exp \left[-\frac{(\delta V - \frac{m \omega^2 \Delta^2}{2})^2}{4m \omega^2 V \Delta^2} \right] \quad (27)$$

Because the probability distribution $P(\delta V)$ only depends on the interaction V , the Markovian dynamics can be analyzed from an equation for energy change. According to the Metropolis dynamics, the equation of evolution for the energy is equal to:

$$\tau_0 \frac{\partial V}{\partial t} = \int_{-\infty}^0 P(x) dx + \int_0^{\infty} x P(x) \exp(-\beta x) dx \quad (28)$$

where τ_0 is a typical time that is inversely proportional to an atomic attempt frequency (10^{-12} s). For the simplest cases, i.e. when the bonds (oscillators) have the same frequency ω (see [215] for mode-dependent solutions), equation (28) reduces [213] to:

$$\tau_0 \frac{\partial V}{\partial t} = \frac{1}{2\beta} [(1 - 4V\beta)f(t)] + \frac{m\omega^2\Delta^2}{4} \operatorname{erfc} \sqrt{\frac{m\omega^2\Delta^2}{16V}} \quad (29)$$

where $\beta = 1/T$, and:

$$f(t) = \frac{m\beta\omega^2\Delta^2}{2} \exp\left[-\frac{m\beta\omega^2\Delta^2}{2}(1 - 2V\beta)\right] \times \operatorname{erfc}\left[\sqrt{\frac{m\omega^2\Delta^2}{16V}}(4V\beta - 1)\right] \quad (30)$$

and erfc is the complementary error function. Equation (29) has an obvious solution, equipartition ($V = T/2$), corresponding to the equilibrium state for the liquid. Results of this model (equation (29), figure 21) show that the glass transition can be reproduced and, at low temperature, the system falls out of equilibrium which manifests by a departure from the equilibrium state $V = T/2$. A decrease of the cooling rate q brings the system to a lower glass energy $V(q, T \rightarrow 0) = V^*(q)$ [213]. Upon reheating, the hysteresis curve signals the onset of relaxation, and this leads to a strong exotherm peak in the first derivative (C_p , inset of figure 21). Linear extrapolations (figure 21) permit one to determine a fictive temperature as a function of cooling rate q . The cross-over between the low-temperature expansion of equation (29) and the equilibrium line $V = T/2$ leads to:

$$q = \frac{4T_f}{\pi\tau_0 \left[\operatorname{erf} \sqrt{\frac{m\omega^2\Delta^2}{8T_f}} - \operatorname{erf} \sqrt{\frac{m\omega^2\Delta^2}{8V^*(q)}} \right]} \quad (31)$$

Similarly, the corresponding heat capacity C_p has the observed behavior from DSC (figure 17) for both the cooling and the heating curves, and the inflection point of the heating curve serves to define a ‘calorimetric’ T_g (filled box in the inset of figure 21) as in the experiments.

In such class of models, departure from the equilibrium value results from a low acceptance rate for moves $x_i \rightarrow x'_i$ according to the Metropolis algorithm. In fact, at low temperature most of the changes leading to an increase of the energy will be rejected, and the system has an acceptance rate for moves that decays to zero. Interestingly, the relaxational dynamics associated with this low acceptance rate can be exactly calculated by linearizing equation (29) around the equilibrium solution, and this leads to an Arrhenius-like behavior at low temperature for the relaxation time of the form:

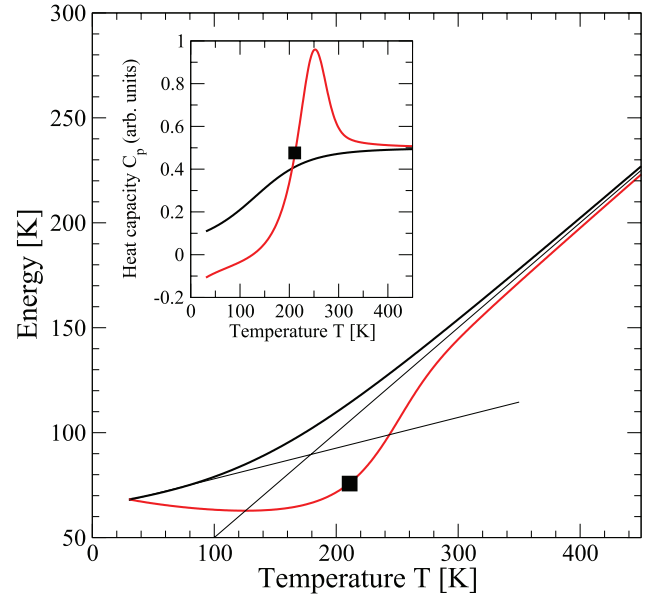


Figure 21. Energy $V(T)$ of a harmonic oscillator system [216] (solution of equation (29)) under cooling (black, upper curve), and annealing (red lower curve) for a rate $q = \pm 1 \text{ K} \cdot \text{s}^{-1}$. The inset shows the evolution of the heat capacity. Black squares indicate the inflexion point of the C_p curve.

$$\tau = \tau_0 \sqrt{\frac{2\pi T^3}{m^3 \omega^6 \Delta^6}} \exp\left[\frac{m\omega^2\Delta^2}{8T}\right] \quad (32)$$

A central result of this approach is that the activation energy for relaxation is directly linked [213, 216] with the typical vibrational frequency of the bonds, which is a local property of the glass, a result that has been recently extended to elastically interacting spring networks [220].

4.4. Survey of other approaches

There are many other approaches which attempt to relate the glassy relaxation to some other physical quantities or parameters. Kovacs and colleagues introduce a retardation time for exponential decay able to appropriately treat the stretched exponential decay of the α -relaxation regime [221] using a finite series of exponentials and, under certain assumptions, the approach can be connected to the TNM phenomenology. However, while the formalism is able to reproduce thermal histories of the glass transition, i.e. cooling and heating scans of enthalpy, its application has been essentially limited to polymers.

In a similar spirit, Ngai *et al* [222] have developed a coupling model that identifies the relaxation rate as the relevant variable, and connects the relaxation time of the stretched exponential function with the Kohlrausch parameter β . This leads to a time-dependent decay function that exhibits non-linearity and a slow-down of the dynamics as the temperature is decreased [223]. A certain number of inorganic ionic-conducting glasses have been analyzed from this approach [127, 224]. However the rate equation of decay function that leads to glassy dynamics has been found to be inconsistent with the Boltzmann superposition principle [225].

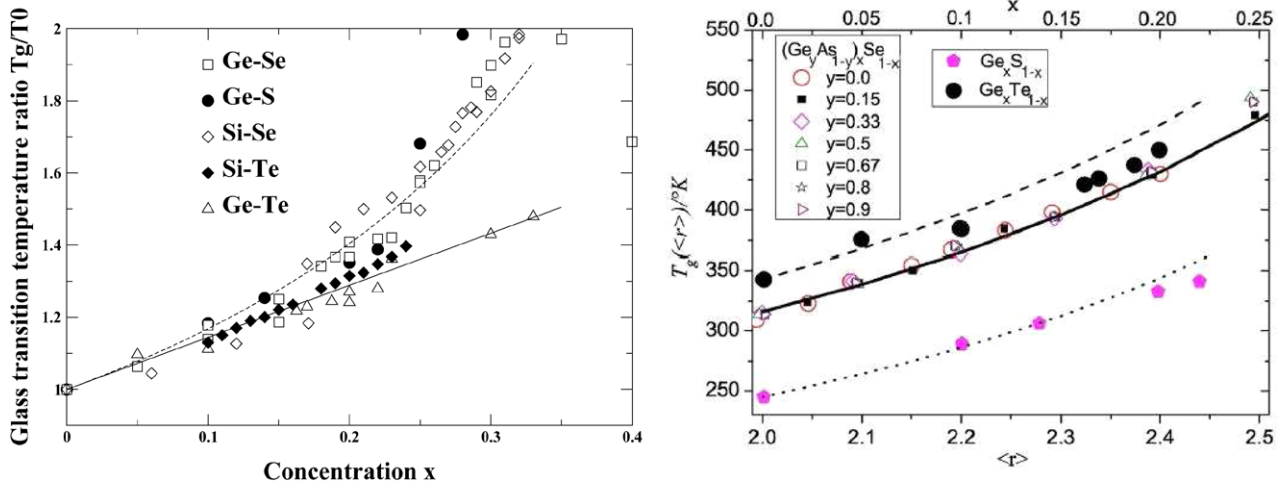


Figure 22. Left: glass transition temperature in binary chalcogenide glasses. Data from Ge–Se [236], Ge–S [237], Si–Se [238], Ge–Te [239] and Si–Te [240]. The solid line corresponds to equation (35) with ($r_A = 2$, $r_B = 4$). The dashed curve corresponds to the fitted Gibbs–Di Marzio equation (equations (33) and (34)), with $B^{-1} = 2 \ln 2 = 0.73$. Right: prediction of the glass transition temperature from the Naumis model [241] for different binary and ternary chalcogenide glasses. Here, the label $\langle r \rangle$ on the x -axis stands for the network mean coordination number. Experimental data are taken from [8, 237, 239]. Permission from the American Physical Society.

Similarly to the coupling model, a certain number of approaches use the stretched exponential to incorporate some non-linear effects which are able to reproduce the glass transition phenomenology. For instance, in [226], non-linearity is introduced by defining a dependence of the relaxation time on the fictive temperature, and such effects act on the endothermic peak obtained in enthalpy at the glass transition and its subsequent evolution under aging. In the case of vitreous selenium, a multioordering parameter model [227] uses a continuous distribution of relaxation times defined by a single Kohlrausch parameter β , able to reproduce experimental DSC data, and to predict the fictive temperature evolution under arbitrary temperature-time histories. The reproduction of DSC data appears to be central to the validation of such simple models, and Yue and colleagues [228] have recently proposed a unified routine to characterize the glass relaxation behavior and determine enthalpic fictive temperature of a glass with an arbitrary thermal history. As a result, the enthalpic fictive temperature of a glass can be determined at any calorimetric scan rate in excellent agreement with modeled values.

5. Role of network topology and rigidity

In network glasses, the effect of structure and network topology or rigidity appears to be central to the understanding of the effect of composition on T_g and relaxation.

5.1. Network connectivity and glass transition temperature

There are various empirical or theory-based relationships showing that the glass transition temperature strongly depends on the glass structure, and that there is much to learn from the evolution with connectivity of T_g .

Besides thermodynamic or vibrational factors such as the well-known ‘two-third rule’ stating that T_g scales as $2/3T_m$

[22] or the Debye temperature of the phonon spectrum, there are structural factors and, in particular, aspects of network connectivity. Tanaka [229] has given an empirical relationship between T_g and the average valence Z of the involved atoms: $\ln T_g \simeq 1.6Z + 2.3$. Varshneya and colleagues [230, 231] have also shown that a modified Gibbs–Di Marzio equation [232], initially proposed for cross-linked polymers, could predict T_g in multicomponent chalcogenide glass systems as a function of the average network coordination number \bar{r} , based only on the degree of atomic cross-linking in a polymeric selenium-based glass (e.g. Ge–Se). The parameter B used has been shown to be dependent on the coordination number r_B of the cross-links (Ge, Si) [233]:

$$T_g(\bar{r}) = \frac{T_g(\bar{r} = 2)}{1 - B(\bar{r} - 2)} \quad (33)$$

with:

$$\frac{1}{B} = (r_B - 2) \ln \left[\frac{r_B}{2} \right] \quad (34)$$

Using stochastic agglomeration of basic local structures representative of the glass [234, 235], an analytical T_g prediction for binary and ternary glasses has been established that seems to be satisfied for a variety of binary and ternary network glasses (figure 22 left). For the former, the glass transition variation of a weakly modified glass A_xB_{1-x} behaves as:

$$\left[\frac{dT_g}{dx} \right]_{x=0} = \frac{T_g(x=0)}{\ln \left[\frac{r_B}{r_A} \right]} = \frac{T_0}{\ln \left[\frac{r_B}{r_A} \right]} \quad (35)$$

where r_B and r_A are the coordination numbers of the atoms or species B and A , respectively, acting as local building blocks of the glass structure, e.g. one has $r_B = 3$ and $r_A = 4$ in a silicate glass made of Q^3 and Q^4 tetrahedral units [235], or $r_B = 4$ and $r_A = 2$ in binary Ge–Se (figure 22). For a ternary system, a parameter-free relationship between T_g and the network

mean coordination number can be also derived on the same basis [242]:

$$\bar{r} = r_{AB} r_{BC} \frac{r_{AC} \alpha^2 (1 - \gamma) + r_{AB} \gamma^2 (1 - \alpha) + r_{BC} \alpha \gamma (\alpha \gamma - \alpha - \gamma)}{(r_{AC} \alpha + r_{AB} \gamma - r_{BC} \alpha \gamma)^2 - 2 r_{AB}^2 r_{BC} \alpha \gamma} \quad (36)$$

where

$$\alpha = \left(\frac{r_A}{r_C} \right)^{T_0/T_g}, \quad \gamma = \left(\frac{r_A}{r_B} \right)^{T_0/T_g}, \quad \delta = \left(\frac{r_A^2}{r_B r_C} \right)^{T_0/T_g} \quad (37)$$

and an excellent agreement has been found with experimental data [243, 244]. Using a slightly different approach based on the general link between the mean-square displacement, $\langle r^2(t) \rangle$, and the vibrational density of states

$$\langle r^2(t) \rangle = \frac{k_B T}{m} \int_0^\infty \frac{g(\omega)}{\omega^2} d\omega, \quad (38)$$

Naumis [241] has derived from the Lindemann criterion of solidification [245], using $\langle r^2(t) \rangle$, a relationship predicting the variation of the glass transition temperature (figure 22, right). These analytical models are helpful in understanding the effect of composition on T_g , and emphasize the central role played by network connectivity, and such ideas and relationships actually help in decoding further anomalies (T_g extrema) which do appear in particular systems such as Ge–Se [236], borates [246] or germanates [247]. Given that the glass-transition temperature is an intrinsic measure of network connectivity, T_g maxima in Ge–Se and As–Se glasses have been interpreted [248] as the manifestation of nanoscale phase separation that is driven by broken chemical order [249] in stoichiometric GeSe₂ and As₂Se₃, and this leads to a reduction of the network connectivity for the Se-rich majority phase at compositions where a T_g maximum is measured.

5.2. Rigidity theory of network glasses

In addition to the effects of network structure on T_g , there is an attractive way to analyze and predict relaxation and glass transition-related properties using rigidity theory. This theory provides an atomic scale approach to understanding the physico-chemical behavior of network glasses using the network topology and connectivity as basic ingredients, and builds on concepts and ideas of mechanical constraints that have been introduced in the pioneering contributions of Lagrange and Maxwell [250, 251]. Phillips [60, 252, 253] has extended the approach to disordered atomic networks, and has recognized that the glass-forming tendency of covalent alloys is optimized for particular compositions. Specifically, it has been emphasized that stable glasses have an optimal connectivity, or mean coordination number $\bar{r} = \bar{r}_c$, which exactly satisfies the Maxwell stability criterion of mechanically isostatic structures, or the condition, $n_c = n_d$, where n_c is the count of atomic constraints per atom and n_d the network dimensionality (usually 3).

In covalent glasses the dominant interactions are usually near-neighbor bond-stretching (BS) and next-near-neighbor bond-bending (BB) forces (see equation (26)). The number of

constraints per atom can be exactly computed in a mean-field way, and is given by:

$$n_c = \frac{\sum_{r \geq 2} n_r \left[\frac{r}{2} + 2r - 3 \right]}{\sum_{r \geq 2} n_r} \quad (39)$$

where n_r is the concentration of species being r -fold coordinated. The contribution of the two terms in the numerator is obvious because each bond is shared by two neighbors, and one has $r/2$ bond-stretching (BS) constraints for a r -fold atom. For BB (angular) constraints, one notices that a two-fold atom involves only one angle, and each additional bond needs the definition of two more angles, leading to the estimate of $(2r - 3)$. For one-fold terminal atoms, a special count [254] is achieved as no BB constraints are involved, and in certain situations some constraints can be ineffective [255]. By defining the network mean coordination number \bar{r} of the network by:

$$\bar{r} = \frac{\sum_{r \geq 2} r n_r}{\sum_{r \geq 2} n_r} \quad (40)$$

one can reduce (39) to the simple equation:

$$n_c = \frac{\bar{r}}{2} + 2\bar{r} - 3 \quad (41)$$

Applying the Maxwell stability criterion, isostatic glasses ($n_c = 3$) are expected to be found at the mean coordination number [60] of $\bar{r} = 2.40$ in 3D, corresponding usually to a non-stoichiometric composition where the glass-forming tendency has been found to be optimized experimentally [256, 257].

The physical origin of this stability criterion has been revealed from the vibrational analysis of bond-depleted random networks [61] constrained by bond-bending and bond-stretching interactions (see equation (26)). It has been demonstrated that the number of zero frequency (floppy) modes f (i.e. the eigenmodes of the dynamical matrix) vanishes for $\bar{r} = 2.38$ when rigidity percolates in the network. The Maxwell condition $n_c = n_d$, therefore, defines a mechanical stiffness transition, an elastic phase transition, above which redundant constraints produce internally stressed networks, identified with a stressed-rigid phase [258, 259]. For $n_c < n_d$, however, floppy modes can proliferate, and these lead to a flexible phase where local deformations with a low cost in energy (typically 5 meV [217]) are possible, their density being given by: $f = 3 - n_c$. There have been various experimental probes of this peculiar transition from Raman scattering [260], stress relaxation [261] and viscosity measurements (figure 23, [8]), vibrational density of states [217], Brillouin scattering [262, 263], Lamb–Mössbauer factors [256], resistivity [264], and Kohlrausch exponents [8, 134, 261]. For a full account of experimental probes and early verification of rigidity theory, readers should refer to books devoted to the subject [265–267].

5.3. Rigidity Hamiltonians

With the prediction of such thresholds and their observation in various properties associated with relaxation in

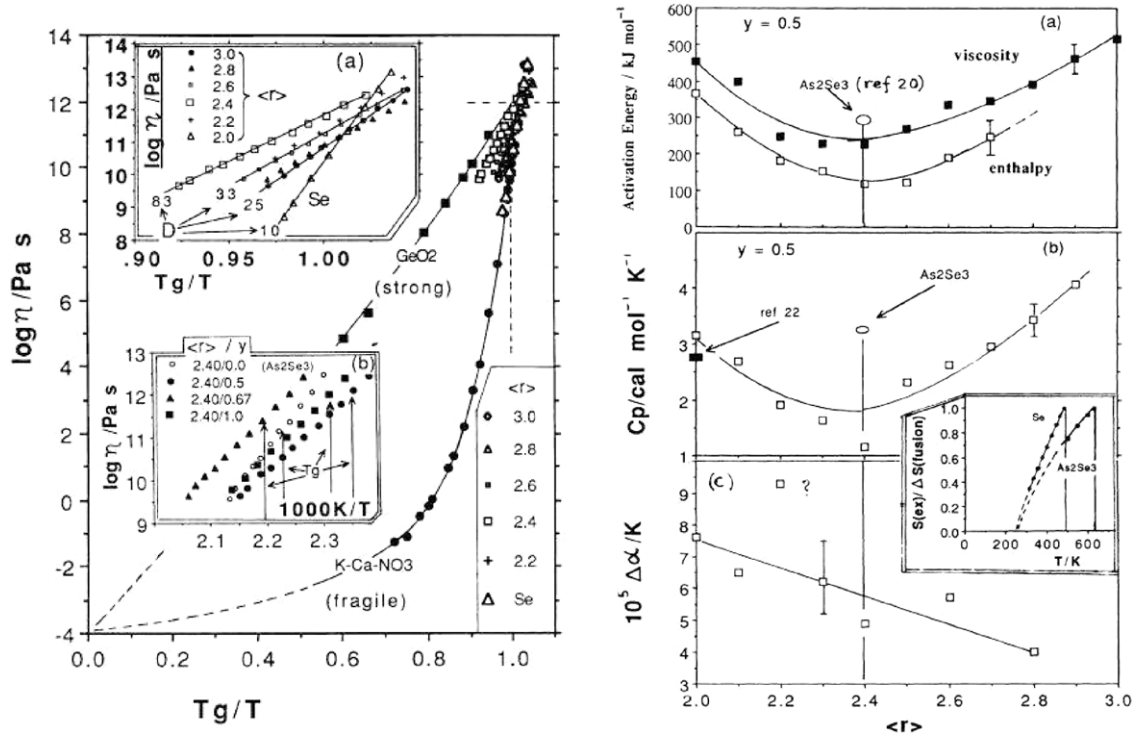


Figure 23. Early verification of the role of rigidity [8] on the relaxation properties in a network-forming liquid (here As–Ge–Se). Left: comparison of pseudo-binary As–Ge–Se liquid viscosities near T_g , compared to the strong (GeO_2) and fragile (K-Ca-NO_3) extremes. The inset zooms into the glass transition region, and shows a strong behavior for a network mean coordination number of $\bar{r} = 2.4$ close to $T_g/T = 1$. Right: behavior with mean coordination number \bar{r} : activation energy determined either from viscosity or enthalpy data (a), heat capacity jump ΔC_p at the glass transition (b), and excess expansion coefficient $\Delta \alpha$ (c). Permission from the American Physical Society.

chalcogenides, oxides and other disordered glassy networks, the connectivity-related flexible to stressed-rigid elastic phase transition has become an interesting means to understand and analyze, in depth, compositional trends of glassy dynamics and relaxation. However, although it provides a framework to understand many features of a system, thermodynamics is absent in the initial approach. One of the main drawbacks of rigidity theory is that the enumeration of bonding constraints in equation (39) is performed on a fully connected network, in principle at $T = 0$ K when neither bonds nor constraints are broken by thermal activation (see, however, [268]), and structural relaxation is obviously absent. The use of the initial theory [61, 250, 251, 258] may be valid as long as one is considering strong covalent bonds or when the viscosity η is very large at $T < T_g$, given that η is proportional to the bonding fraction, but equation (39) is obviously not valid in a high temperature liquid, and one may wonder to what extent it remains useful for the glassy relaxation at $T \simeq T_g$. However, NMR-related relaxational phenomena in Ge–Se indicate that the low temperature rigidity concept can be extended from the glass to the liquid in binary chalcogenide melts with confidence [137]. Furthermore, in equation (39) a mean-field treatment is implicitly assumed given that an average constraint count is performed over all the atoms in the network. This supposes homogeneity of the system, even at the microscopic scale, and neglects the possibility of atomic-scale phase separation or large fluctuations in constraints or coordination numbers as the phase transition is approached.

An important step forward has been made by Naumis and colleagues [269–271]. Prior to the production of a rigidity-related Hamiltonian that could serve as a starting point for the statistical mechanics derivation of various thermodynamic quantities [269, 270], one had to realize that the fraction of cyclic variables in phase space are identified with the fraction of floppy modes $f = 3 - n_c$ because when one of these variables is changed, the system will display a change in energy that is negligible. This means that in the simplest model [271] for network atomic vibrations in the harmonic approximation, the Hamiltonian can be given by:

$$\mathcal{H} = \sum_{j=1}^{3N} \frac{P_j^2}{2m} + \sum_{j=1}^{3N(1-f)} \frac{1}{2} m \omega_j^2 Q_j^2 \quad (42)$$

where Q_j (position) and P_j (momentum) are the j th normal mode coordinates in phase space, and ω_j is the corresponding eigenfrequency of each normal mode. Since it is assumed that floppy modes have a zero frequency, they will not contribute to the energy so that the sum over coordinates only runs up to $3N(1 - f)$.

From this simple Hamiltonian, a certain number of basic features of thermodynamics in connection with rigidity can be derived. First, from the partition function derived from equation (42), both the free energy \mathcal{F} of the system and the specific heat are found [271] to depend on the fraction of floppy modes:

$$\mathcal{F} = -\frac{3Nk_B T}{2} \ln \left(\frac{2\pi m k_B T}{h^2} \right) - \frac{kT}{2} \sum_{j=1}^{3N(1-f)} \ln \left(\frac{2\pi k_B T}{m \omega_j^2} \right) \quad (43)$$

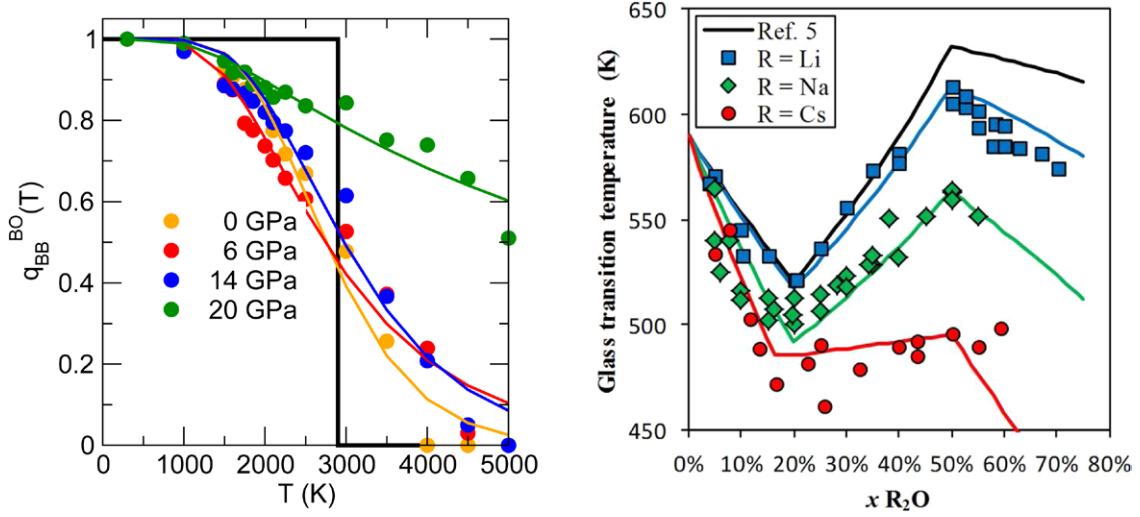


Figure 24. Left: temperature behavior of the Mauro–Gupta function [35] (solid curves, equation (47)) for bond-bending bridging oxygen (BO) in densified sodium silicates, compared to a direct calculation [274] from MD simulations (see below). The data can also be fitted with a random bond function [52] (equation (48)). Simple calculations of topological constraint theory usually involve a step-like function (thick black curve) with an onset temperature, e.g. here, at $T_\alpha \simeq 2900$ K. Right: prediction of the glass transition temperature T_g of binary alkali phosphate glasses $(1-x)\text{R}_{20} - (1-x)\text{P}_2\text{O}_5$ ($\text{R} = \text{Li}, \text{Na}, \text{Cs}$) from temperature-dependent constraints [277]. Permission from AIP Publishing LLC 2015.

$$C_v = 3Nk_B - \frac{3Nk_B}{2}f \quad (44)$$

The latter expression indicates that the specific heat in such model systems corresponds to the Dulong–Petit value that is decreased by a floppy mode contribution, and the finite value of the floppy mode frequency [217] can also be taken into account [271]. Building on these ideas, an energy landscape treatment of rigidity leads to the conclusion that floppy modes can provide a channel in the energy landscape. Indeed, given that variables associated with f are cyclic variables of the Hamiltonian, the energy of the system does not depend upon a change in a floppy mode coordinate, and for a given inherent structure (i.e. a local minimum characterized by ω_j), the number of channels is given by f which increases the available phase space allowed to be visited. Consequently, the number of accessible states $\Omega(E, V, N)$ can be calculated in the microcanonical ensemble, and using the Boltzmann relation $S = k_B \ln \Omega(E, V, N)$, one finds that the configurational entropy provided by the channels in the landscape is simply given by:

$$S_c = f N k_B \ln V, \quad (45)$$

i.e. the floppy mode density is contributing to the configurational entropy and the dynamics of the glass-forming system. From a short-range square potential, the basin-free energy of a potential energy landscape has been investigated using MD simulations [272], and it can be separated into a vibrational and a floppy mode component, allowing for an estimate of the contribution of flexibility to the dynamics, and for this particular class of potentials it has been found that S_c scales as f^3 .

5.4. Temperature-dependent constraints

Building on this connection between floppy modes and the configurational entropy S_c (equation (45)), Gupta and Mauro

have extended topological constraint counting to account explicitly for thermal effects [35] in an analytical model *via* a two-state thermodynamic function $q(T)$. This function quantifies the number of rigid constraints as a function of temperature and subsequently modifies equation (39) to become:

$$n_c(T) = \frac{\sum_{r \geq 2} n_r [q_{\text{BS}}^r(T) \frac{r}{2} + q_{\text{BB}}^r(T)(2r-3)]}{\sum_{r \geq 2} n_r}, \quad (46)$$

where $q_{\text{BS}}^r(T)$ and $q_{\text{BB}}^r(T)$ are step functions associated with BS and BB interactions of an r -coordinated atom (figure 24, left) so that n_c now explicitly depends on temperature. This function has two obvious limits because all relevant constraints can be either intact at low temperature ($q_i^j(T) = 1$) like in the initial theory [60, 61] or entirely broken ($q_i^j(\infty) = 0$) at high temperature. At a finite temperature, however, only a fraction of these constraints can become rigid once their associated energy is less than $k_B T$. Different forms can be proposed for $q_i^j(T) = q(T)$ based either on an energy landscape approach [273]:

$$q(T) = [1 - \exp(-\Delta/T)]^{\nu t_{\text{obs}}}, \quad (47)$$

ν being the attempt frequency and t_{obs} the observation time, or involving a simple activation energy Δ for broken constraints [52]:

$$q(T) = \frac{1 - e^{\Delta/T}}{1 + e^{\Delta/T}}, \quad (48)$$

and the general behavior of $q(T)$ can be computed for any thermodynamic condition from MD simulations [274] (see below). A certain number of thermal and relaxation properties of network glass-forming liquids can now be determined, and a simple step-like function (thick black line in figure 24, left)

with an onset temperature T_α for various constraints allows one to obtain analytical expressions for glass transition temperature [35, 275–278], heat capacity [279], and glass hardness [278, 280]. Fragility can be determined from a continuous form of equation (48). Two central ingredients are necessary. First, it is assumed that the Adam-Gibbs model for viscosity (equation (4)), $\eta = \eta_\infty \exp(A/TS_c)$, holds in the temperature range under consideration, and that the corresponding barrier height A is a slowly varying function with composition. This means that only the configurational entropy S_c will contain the temperature and composition dependence. Secondly, it is assumed that the expression (45) relating the configurational entropy to topological degrees of freedom (floppy mode density) is valid. Strong support for this approach is provided by the MYEGA viscosity modeling curve (equation (7)) which uses these two basic assumptions and has been tested with success over more than a hundred different glass-forming liquids [33]. By further stating that T_g is a reference temperature at which $\eta(T_g(x), x) = 10^{12} \text{ Pa} \cdot \text{s}$ for any composition, equations (4) and (45) can be used to write:

$$\begin{aligned} \frac{T_g(x)}{T_g(x_R)} &= \frac{S_c(T_g(x_R), x_R)}{S_c(T_g(x), x)} = \frac{f(T_g(x_R), x_R)}{f(T_g(x), x)} \\ &= \frac{3 - n_c(T_g(x_R), x_R)}{3 - n_c(T_g(x), x)} \end{aligned} \quad (49)$$

and $T_g(x)$ can be determined with composition x from a reference compound having a composition x_R and a glass transition $T_g(x_R)$, knowing the number of topological degrees of freedom (i.e. $3 - n_c$) for compositions x and x_R from equation (46), and the behavior of the step functions $q(T)$.

Using the expression for $S_c(T_g(x), x)$ in equation (49), and the definition of fragility (equation (1)), one can, furthermore, extract an expression for the fragility index \mathcal{M} as a function of composition:

$$\begin{aligned} \mathcal{M}(x) &= m_0 \left(1 + \frac{\partial \ln S_c(T, x)}{\partial \ln T} \bigg|_{T=T_g(x)} \right) \\ &= m_0 \left(1 + \frac{\partial \ln f(T, x)}{\partial \ln T} \bigg|_{T=T_g(x)} \right) \end{aligned} \quad (50)$$

Typical applications for the prediction of the glass transition temperature concern simple chalcogenides [35], borates [275], borosilicates [279] phosphates [278], or borophosphate glasses [276] (figure 24, right). Equation (50) usually leads to a good reproduction of fragility data with composition, but requires a certain number of onset temperatures T_α (see figure 24, left) that can be estimated from basic assumptions, or which act as parameters for the theory. In addition, such onset temperatures T_α can be related to the corresponding activation energy [35] (equation (47)) to break a constraint via:

$$\Delta = -k_B T_\alpha [1 - 2^{-1/(\nu_{\text{obs}})}] \quad (51)$$

The agreement of such predictive laws for fragility is usually excellent (figure 25(a)), and calculations have been stressed to be robust against parameter sensitivity [275–279].

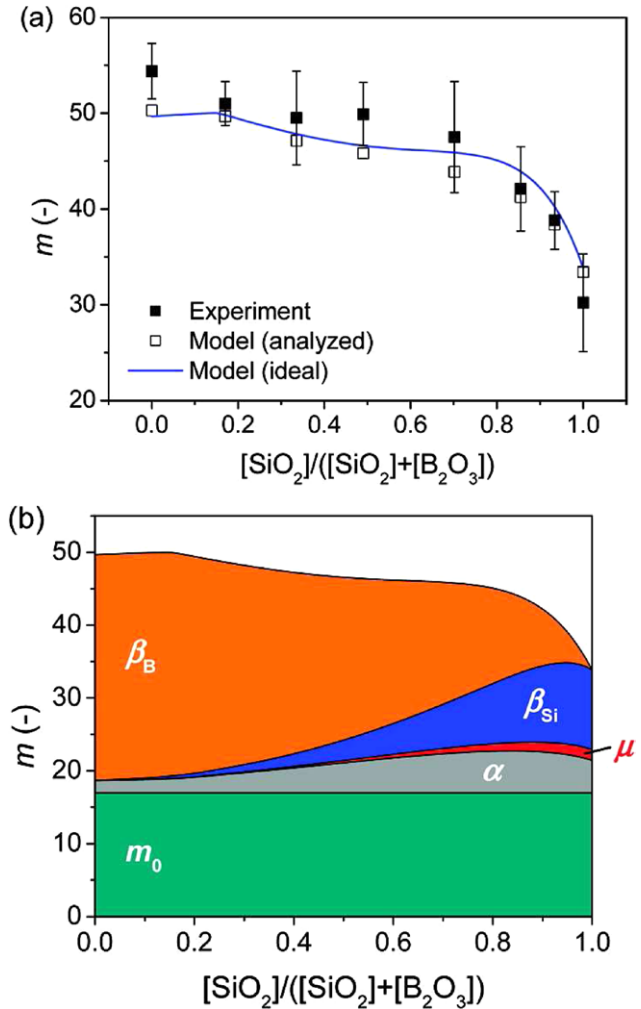


Figure 25. Modeling the composition dependence of the liquid fragility index (m) for borosilicate glasses [279]. (a) Prediction of the fragility index (solid line) as a function of composition, compared to experimental data measured from DSC experiments. (b) Effect of the constraint contribution on the computed fragility with composition: Boron β_B and silicon β_{Si} BB constraints, BS constraints (α) and non-bridging oxygen-related constraints (μ). m_0 is the reference fragility appearing in equation (50). Reprinted with permission from [279].

What is learned from such fragility predictions? First, since the constraint count that evaluates the fragility index is performed on models that reproduce the change in local structure under composition change, the temperature-dependent constraint approach provides a top-down validation of such structural models. Furthermore, as noticed from figure 25(b), one has the opportunity to probe what aspects of interactions contribute the most to the evolution of fragility with composition. In the represented example of borosilicates [279] (figure 25(b)), \mathcal{M} is found to be mostly driven by the bond angle interactions involved in silicon (β_{Si}) and boron (β_B) that constrain the bond-bending motion of the glass-forming liquid (figure 25(b)), whereas the BS interactions contribute only at a large silicon to boron ratio.

With the same formalism, the heat capacity change ΔC_p at the glass transition can be calculated and compared to measurements accessed from DSC. Using the temperature dependence of constraints, it is assumed at a first stage that the major

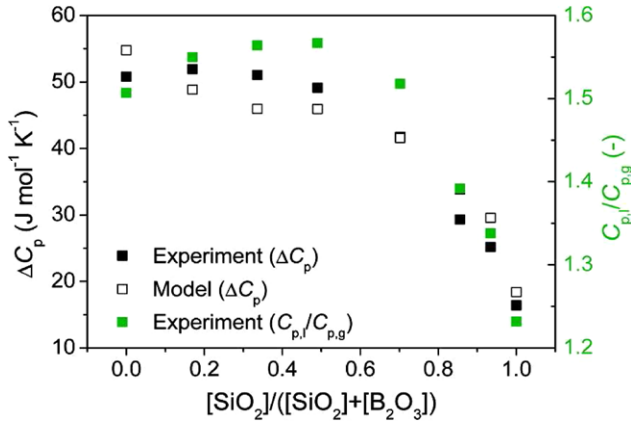


Figure 26. Composition dependence of the change in the isobaric heat capacity ΔC_p during the glass transition in a sodium borate glass [279]. Comparison between experimental data (filled squares) and the model calculations of ΔC_p from equation (54). Reprinted with permission from [279].

contribution to heat capacity at the glass transition arises from configurational contributions $C_{p,\text{conf}}$ that can be related to S_c , so that one has: $\Delta C_p = C_{pi} - C_{pg} \simeq C_{p,\text{conf}}$. The heat capacity change can then be written as a function of the configurational enthalpy and S_c :

$$\Delta C_p = \left(\frac{\partial H_{\text{conf}}}{\partial T} \right)_p = \left(\frac{\partial H_{\text{conf}}}{\partial \ln S_{\text{conf}}} \right)_p \left(\frac{\partial \ln S_{\text{conf}}}{\partial T} \right)_p \quad (52)$$

and using the Adam-Gibbs expression (4) and the derived expression for fragility (50), one can, furthermore, write the jump of the heat capacity at the glass transition with composition x_i :

$$\Delta C_p(x_i, T_g(x_i)) = \frac{1}{T_g(x_i)} \left(\frac{\partial H_{\text{conf}}}{\partial \ln S_{\text{conf}}} \right)_{p, T=T_g} \left(\frac{\mathcal{M}(x_i)}{\mathcal{M}_0} - 1 \right) \quad (53)$$

Equation (53) can be recast in a more compact form given that $S_c(T_g)$ is inversely proportional to T_g , and by assuming that $\partial H_{\text{conf}} / \partial S_c$ is, by definition, equal to the configurational temperature at constant pressure [281] which is close to T_g . This, ultimately, leads to a decomposition-dependent prediction of the heat capacity jump at T_g :

$$\Delta C_p(x_i, T_g(x_i)) \simeq \frac{[A(x_i)]_R}{T_g(x_i)} \left(\frac{\mathcal{M}(x_i)}{\mathcal{M}_0} - 1 \right) \quad (54)$$

Once again, and similarly to relationships on T_g (equation (49)) or the fragility index (equation (50)), the heat capacity jump is evaluated with respect to some reference composition because the parameter $[A(x_i)]_R$, appearing in equation (54), connects the configurational entropy $S_c(T_g)$ with T_g for a reference composition x_R . Applications have been performed on the same glassy systems [279], and successfully compared to experimental measurements (figure 26). Again, such predictions have the merit to accurately reproduce experimental data, and to provide some insight into the validity of structural models that can be checked independently from a variety of other experimental (e.g. spectroscopic) probes.

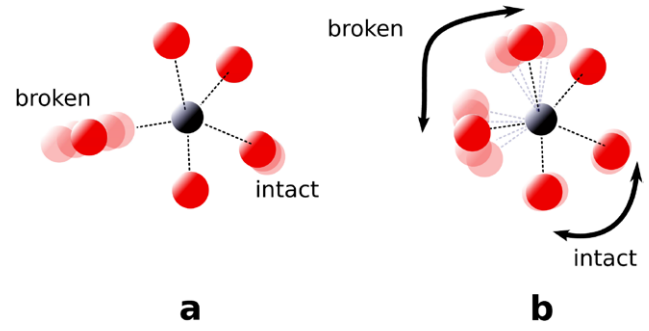


Figure 27. Method of constraint counting from MD-generated configurations. Large (small) radial (a) or angular (b) excursions around a mean value are characterized by large (small) standard deviations on bonds or angles representing broken (intact) constraints.

5.5. MD-based dependent constraints

A more general and alternative approach to a topological constraint count can be proposed in order to establish the number of constraints $n_c(x, T, P)$ for any thermodynamic condition, including under pressure. This is achieved by using molecular dynamics (MD) which also permits establishing correlations with thermodynamic and dynamic properties independently characterized from such atomic scale simulations. In all approaches—classical or first principles (FPMD) using e.g. a Car-Parrinello scheme [282]—Newton's equation of motion is solved for a system of N atoms or ions, representing a given material. Forces are either evaluated from a model interaction potential which has been fitted to recover the properties of some materials, or directly calculated from the electronic density in case of a quantum mechanical treatment using density functional theory (DFT). Recent applications have permitted the very accurate description of the structural and dynamic properties of most archetypal network-forming systems (Ge–Se [282–284], SiO_2 [67], GeO_2 [68, 285], B_2O_3 [286, 287], As–Se [69, 71, 288, 289], As–Ge–Se [290], Si–Se [291, 292] etc), in the glassy or liquid state, and in ambient or densified conditions. A similar achievement has been realized on modified glasses such as alkali silicates [293–297], soda-lime silicates [298, 299], borosilicates [300, 301] or aluminosilicates [302].

The way topological constraints can be extracted from atomic scale trajectories relies essentially on the recorded radial and angular motion of atoms that connects directly to the enumeration of BS and BB constraining interactions, which are the relevant ones for the identification of flexible to rigid transitions. Instead of treating the forces mathematically and querying motion, which is the standard procedure of MD simulations for obtaining trajectories, as in classical mechanics, an alternative scheme is followed. Here, the atomic motion associated with angles or bonds can be related to the absence of a restoring force (figure 27), and this strategy is somewhat different from the ‘*culture of force*’ discussed by Wilcek [303] given that one does not necessarily need to formulate the physical origin of the forces to extract the constraints.

In the case of atomic scale systems, since one attempts to enumerate BS and BB constraints, one is actually not seeking

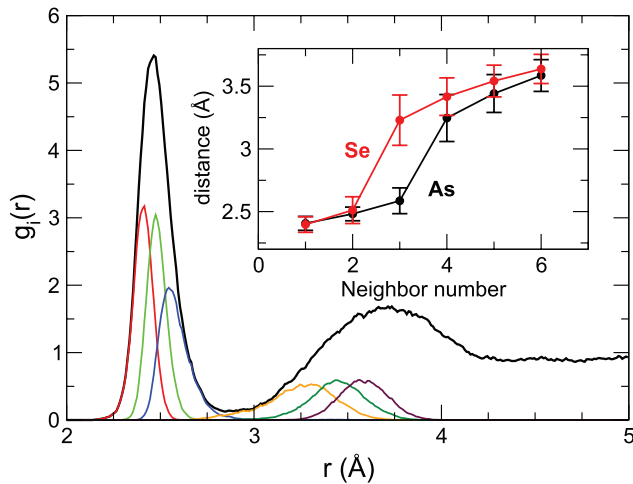


Figure 28. Decomposition of partial pair correlation functions $g_i(r)$ into neighbor distributions in amorphous As_2Se_3 [289]. The inset shows the positions (first moments) of the neighbor distributions and their standard deviations (second moments, represented as error bars), indicating that As and Se have 1.5 and 1 BS constraints, respectively.

motion arising from large radial and angular excursions, but the opposite behavior and also atoms displaying a small motion (vibration) that maintains corresponding bonds and angles fixed around their mean value. These can ultimately be identified with a BS or BB interaction constraining the network structure at the molecular level. Having generated the atomic scale configurations at different thermodynamic conditions from MD, a structural analysis is applied in relation to the constraint counting of rigidity theory such as the one sketched in equation (39).

5.6. Bond stretching

To obtain the number of BS interactions, one focuses on neighbor distribution functions (NDFs) around a given atom i (see figure 28). A set of NDFs can be defined by fixing the neighbor number n (first, second, etc) during the bond lifetime, the sum of all NDFs yielding the usual i -centred pair correlation function $g_i(r)$ where integration up to the first minimum gives the coordination numbers r_i , and hence the corresponding number of bond-stretching constraints $r_i/2$ [71, 289, 304–306]. Figure 28 shows an application to amorphous As_2Se_3 [71]. In As_2Se_3 , three NDFs (colored curves) contribute to the first peak of the As-centred pair correlation function $g_{\text{As}}(r)$, very well separated from the second shell of neighbors, and indicative of the presence of three neighbors around an As atom. It is to be noted that a fourth NDF is present at the minimum of $g_{\text{As}}(r)$, indicating that a small fraction of four-fold As atoms should be present in the glass [289], typically less than 10%. The separation between the first and second shell of neighbors can also be characterized by plotting the NDF peak positions as a function of the neighbor number (inset of figure 28). For example, As_2Se_3 , and also for tetrahedral glasses [305] one can see that there is a clear gap in distance between the distributions belonging to the first and the second neighbor shell. Furthermore, these NDFs which belong to the

first shell display a much lower radial excursion (error bars, see inset of figure 28) as compared to the NDFs of the next (second shell) neighbor distributions. From this simple example (As_2Se_3), one determines $r_{\text{As}} = 3$ and $r_{\text{Se}} = 2$ leading to 1.5 and 1 BS constraints, a result that is expected from a constraint count based solely on the $8-\mathcal{N}$ rule [61, 252], \mathcal{N} being the number of s and p electrons. However, for certain systems for which this rule does not apply (telluride network glasses, see below) or in densified systems with non-monotonic evolutions of coordination numbers under pressure [274], such MD-based constraint counting algorithms provide a neat estimate [304] of BS constraints without relying on crude assumptions.

5.7. Bond bending

5.7.1. Average behavior. The bond-bending (BB) constraint counting from MD simulations is based on partial bond angle distributions (PBADs) $P(\theta_{ij})$ (or $P(\theta)$ in the following) and defined as follows [304, 305]: for each type of a central atom 0, the N first neighbors i are selected, leading to $N(N-1)/2$ possible angles $i0j$ ($i = 1..N-1, j = 2..N$), i.e. 102, 103, 203, etc. The standard deviation σ_θ of each distribution $P(\theta_{ij})$ gives a quantitative estimate of the angular excursion around a mean angular value (figure 27(b)), and provides a measure of the bond-bending strength. Small values for σ_θ correspond to an intact bond-bending constraint which maintains a rigid angle at a fixed value, whereas large σ_θ correspond to a bond-bending weakness giving rise to an ineffective constraint.

Figure 29 shows the PBADs for glassy GeSe_2 and GeO_2 [305]. Broad angular distributions are found in most of the situations, but a certain number of sharper distributions (colored) can also be found, and these are identified with intact angular constraints because these arise from a small motion around an average bond angle. For the special case of tetrahedral glasses, only six angles have nearly identical and sharp distributions, and these are the six angles defining the tetrahedra with a mean value that is centred close to the angle of $\bar{\theta} = 109^\circ$. From such $N(N-1)/2$ different PBADs, a second moment (or standard deviation) can be computed for an arbitrary set of triplets ($i0j$) with ($i, j = 1..N$). Figure 30 shows corresponding results for the standard deviations σ_θ in stoichiometric oxide glasses [305]. Such glasses have their standard deviations nearly equal for the six relevant (Ge, Si) distributions, which are associated with bending motions around the tetrahedral angle of 109° . A slightly different situation occurs in glasses subject to stress, i.e. densified silicates [274] or stoichiometric chalcogenides [71, 282] which exhibit an increased angular bending motion of tetrahedra, as discussed below.

5.7.2. Individual constraints. An additional way of analyzing angular constraints is to follow a given angle individually during the course of the MD simulation (figure 31). For each individual atom k , the angular motion over the time trajectory then leads to a single bond angle distribution $P_k(\theta)$ characterized by a mean $\bar{\theta}_k$ (the first moment of the distribution), and a second moment (or standard deviation σ_{θ_k}). The latter represents, once again, a measure of the strength of the underlying BB interaction. If σ_{θ_k} is large (one usually has $\sigma_{\theta_k} > 15\text{--}20^\circ$

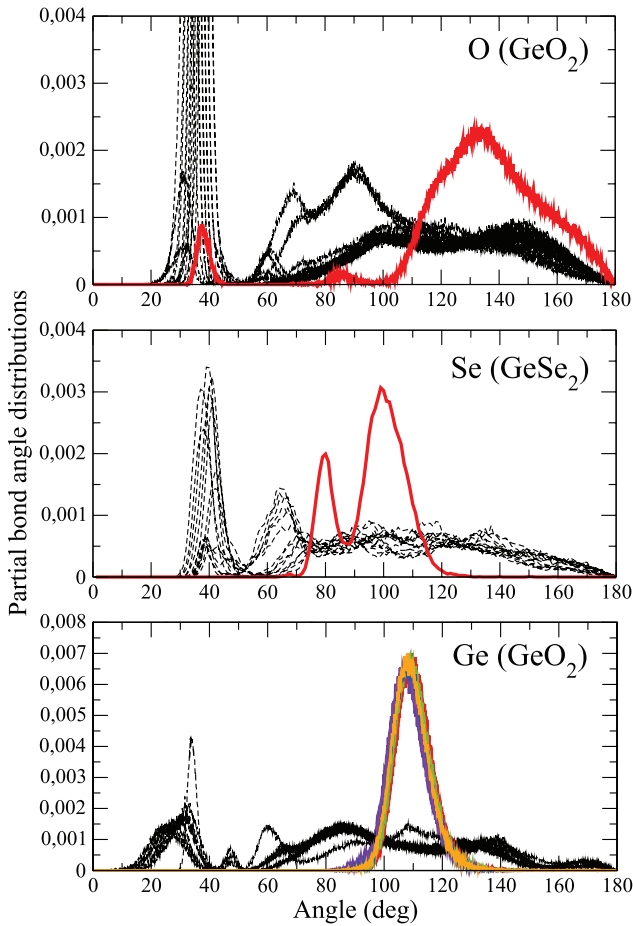


Figure 29. From top to bottom: oxygen, selenium and germanium partial bond angle distributions (PBAD) in GeO_2 and GeSe_2 for an arbitrary $N = 6$ [305] leading to 15 possible PBADs. The colored curves correspond to PBADs with the lowest standard deviation(s) σ_θ . The sharp peaks at $\theta \simeq 40^\circ$ correspond to the hard-core repulsion. The constrained angle around oxygen in germania (panel (c)) is found to be centred at 135° , close to the value obtained from experiments [307]. All other angles display broad variations and correspond to angles defined by next-nearest neighbor shells. Permission from the American Physical Society.

[306]), it suggests that the BB restoring force which maintains the angle fixed around its mean value $\bar{\theta}_k$ is ineffective. As a result, the corresponding BB topological constraint will be broken, and will not contribute to network rigidity. Ensemble averages then lead to a distribution $f(\sigma)$ of standard deviations which can be analyzed and followed under different thermodynamic conditions.

This alternative scheme following constraints individually permits one to separate effects which may arise from disorder from those which originate from the radial or angular motion and which enter into the constraint counting analysis. In fact, when averaged simultaneously over time and space, σ_θ can simply be larger because of an increased angle and bond-length variability induced by an increased bond disorder which will broaden corresponding bond angle/bond length distributions. By following angles and distances with time, this drawback can be avoided. Figure 32 shows the distribution $f(\sigma)$ of angular standard deviations for a bridging oxygen in a sodium silicate liquid with increasing temperatures

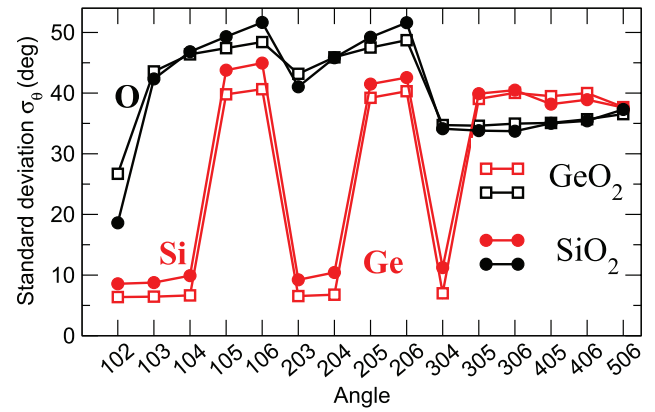


Figure 30. Oxygen and Si/Ge standard deviations computed from 15 PBADs in vitreous germania and silica [305]. The labels on the x -axis refer to all possible triplets $i0j$ between a central atom 0 and two neighbors i and j . For all systems, the PBADs relative to the Group IV (Si, Ge) atom have a low standard deviation σ_θ , of the order of 10 – 20° when the first four neighbors are considered. One finds, for example, $\sigma_{\text{Ge}} \simeq 7^\circ$ for the PBAD 102 of GeO_2 , which is substantially smaller as compared to those computed from other distributions (105, 106, etc) which have $\sigma_\theta \simeq 40^\circ$. Permission from the American Physical Society.

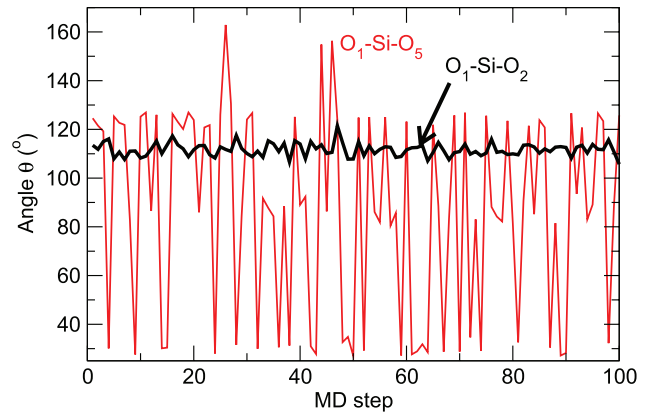


Figure 31. Time evolution (in MD steps) of two typical angles in a liquid sodium silicate [306] defined by either the first two oxygen neighbors around a silicon atom ($\text{O}_1\text{-Si-O}_2$, 102) or by neighbor 1 and neighbor 5 ($\text{O}_1\text{-Si-O}_5$, 105). Large variations are obtained for angles with an ineffective constraint.

[306], and the assignment of the peaks can be made from the inspection of the two limiting temperatures. At elevated temperatures (4000 K), all constraints are, indeed, broken by thermal activation so that $f(\sigma)$ displays a broad distribution centred at a large standard deviation (25°). On the opposite side, at low temperature (300 K) σ_θ values display a sharp distribution ($\sigma < 10^\circ$), indicating that corresponding BB constraints are active. Interestingly, there is a temperature interval at $T \simeq 2000$ K at which one can have a mixture of both types of constraints—effective and ineffective—and the corresponding fraction of intact BB constraints can be computed (inset of figure 32). It exhibits a broad step-like behavior with all the features of the Mauro–Gupta $q(T)$ function [35] introduced previously (see also figure 24).

Such methods, based on angular standard deviations, have also proven to be efficient in order to enumerate the fraction of tetrahedra in amorphous telluride networks [308, 309].

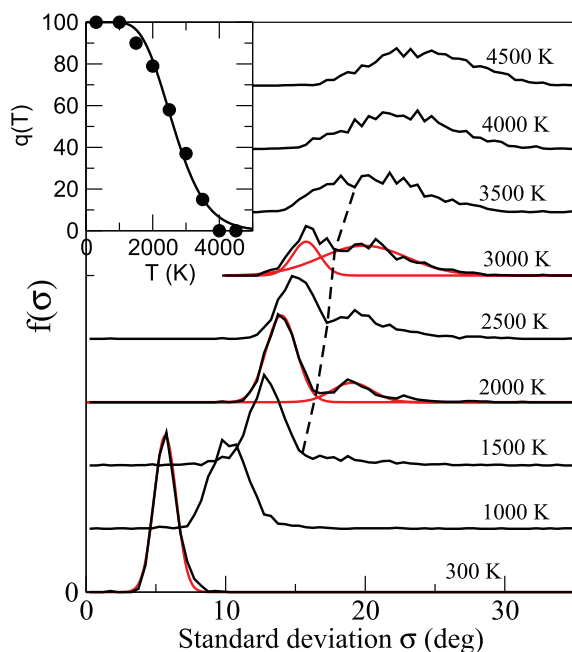


Figure 32. Behavior of the bridging oxygen (BO)-centred standard deviation distributions $f(\sigma)$ in a sodium silicate liquid [306]. Note, the bimodal distribution occurring at $T \approx 2000$ K. The broken line defines a boundary between broken and intact constraint population, estimated to be about $\sigma_\theta = 15^\circ$ at low temperature. Gaussian fits (red curves) are shown for selected temperatures. The inset shows the fraction $q(T)$ of intact oxygen constraints as a function of temperature. The solid curve is a fit using the Mauro–Gupta function [35] of equation (47).

To calculate the population of $\text{GeTe}_{4/2}$ or $\text{SiTe}_{4/2}$ tetrahedra in binary Ge–Te, Si–Te or ternary Ge–Si–Te glasses, one detects atoms having six low standard deviations σ_θ around a Ge/Si atom. Once such atoms are identified, it is found that the corresponding average angle is equal to $\langle \bar{\theta} \rangle \simeq 109^\circ$, and a corresponding bond angle distribution for the whole system peaks at 109° .

Having set the basis of molecular dynamics-based topological constraint counting, we now review certain results obtained within this framework, and how these connect to aspects of glassy relaxation.

6. Rigidity and dynamics with composition

Applications have been performed on a variety of systems [304–306]. We focus, here, on Ge–Se and silicate network glasses and liquids which are probably the most well documented alloys in the field of rigidity transitions.

6.1. Topological constraints

The enumeration of constraints on realistic models of Ge–Se glasses [282] and liquids [284] shows that six Ge standard deviations have a low value ($\sigma_{\text{Ge}} \simeq 10^\circ$), i.e. four times smaller than all the other angles. One thus recovers the result found for the stoichiometric oxides (SiO_2 , GeO_2 , see figure 30). A more detailed inspection reveals that there is a clear difference between compositions (10, 20, and 25% Ge) having

six standard deviations σ_{Ge} nearly equal, and compositions belonging to the stressed rigid phase (33%, 40%) which have an increased value of σ_{Ge} for selected angles. For such systems, as well as for the isochemical compounds ($\text{Ge}_x\text{S}_{100-x}$ [47], $\text{Si}_x\text{Se}_{100-x}$ [238]), the flexible phase has been found to be defined for $0 \leq x \leq 20\%$ and the stressed rigid phase for $x \geq 25\%$, the limit of the glass-forming region being somewhat larger than 33%.

As the Ge content is increased, the intra-tetrahedral angular motion grows for selected angles, as detected, for example, in GeSe_2 by the important growth of standard deviations involving the fourth neighbor of the Ge atom. When the six standard deviations σ_{Ge} defining the tetrahedra are represented as a function of the Ge content (figure 33, left), it is found that the angular motion involving the fourth neighbor (PBADs 104, 204, 304) exhibits a substantial increase once the system is in the stressed rigid phase, while the others (102, 103, 203) are left with a similar angular excursion close to the one found for the oxides (SiO_2 , GeO_2) where it was concluded [305] that tetrahedra were rigid. This underscores the fact that the quantity σ_{Ge} is an indicator of stressed rigidity [284]. Moreover, the presence of stress will lead to asymmetric intra-tetrahedral bending involving an increased motion for selected triplets of atoms, and this indicates that some BB constraints have softened to accommodate stress. A similar situation is encountered in densified silicates [310] or in hydrated calcium silicate networks [311, 312] for which angular motion associated with the tetrahedra $\text{SiO}_{4/2}$ undergoes a substantial change with pressure or composition.

The origin of this softening can be sketched from a simple bar network when stretching motion is considered instead (figure 33, left), and this connects to the well-known relationship between stressed rigidity and bond mismatch in highly connected covalent networks [313]. In such systems, atoms having a given coordination number cannot fulfill all their bonds at the same length because of an important network connectivity that prevents a full relaxation towards identical lengths. In the simplified bar structures sketched in figure 33, all bars can have the same length in flexible (0–20% at Ge) and isostatic networks (20–25% at Ge), but once the structure becomes stressed rigid, at least one bar (e.g. the red bar in figure 33) must have a different length. A similar argument holds for angles. In the stressed rigid Ge–Se, because of the high network connectivity, $\text{GeSe}_{4/2}$ tetrahedra must accommodate the redundant cross-links which force softer interactions [217] (i.e. angles) to adapt and to break a corresponding constraint. This leads to increased angular excursions for atomic Se–Ge–Se triplets (figure 33) involving the farthest (fourth) neighbor of a central Ge atom.

When such systems are analyzed from individual constraints (figure 33 [282], right), it is also seen that some Ge-centred angles have softened once the glass has become stressed rigid. For the flexible GeSe_9 (10%) and the isostatic GeSe_4 (20%, $n_c = 3$ in a mean field count) compositions, a single distribution $f(\sigma)$ for all six angles (102,...304) is found, located at a low value ($\sigma \simeq 8\text{--}9^\circ$) which indicates a weak angular intra-tetrahedral motion. However, at higher Ge content corresponding angles involving the fourth neighbor

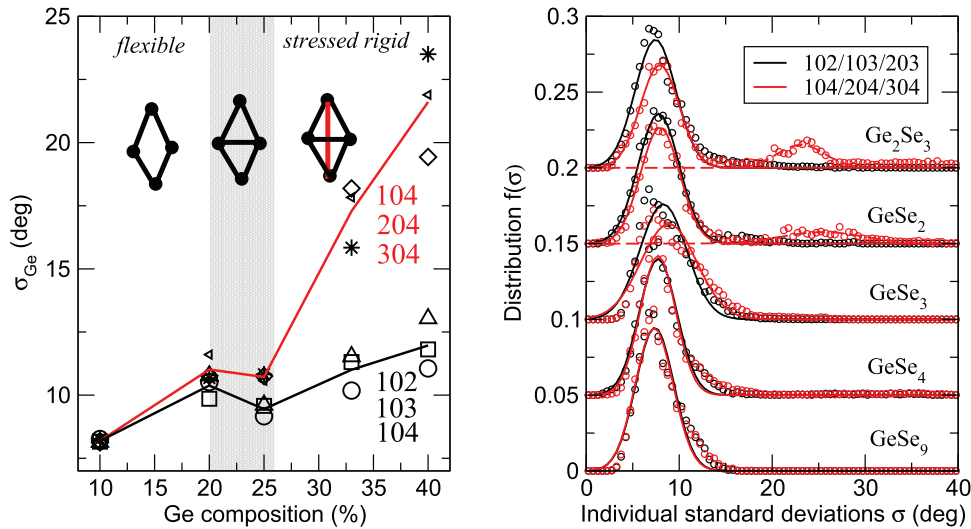


Figure 33. Left: Standard deviations σ_{Ge} as a function of Ge composition in the Ge–Se system [305], split into a contribution involving the fourth neighbor (red line, average of 104, 204 and 304) and the other contributions (black line). The shaded area corresponds to the Boolchand (isostatic) intermediate phase [43] (see below). A simple bar structure represents the nature of the different elastic phases (see text for details). Right: Distribution of Ge angular standard deviations using individual constraints [282]. The total distributions have been split, depending on the neighbor rank: angles involving the first three neighbors (102, 103, 203, black symbols), and the fourth neighbor (104, 204, 304, red symbols). The solid curves are Gaussian fits which serve to estimate the population of broken constraints at high x content. Permission from the American Physical Society.

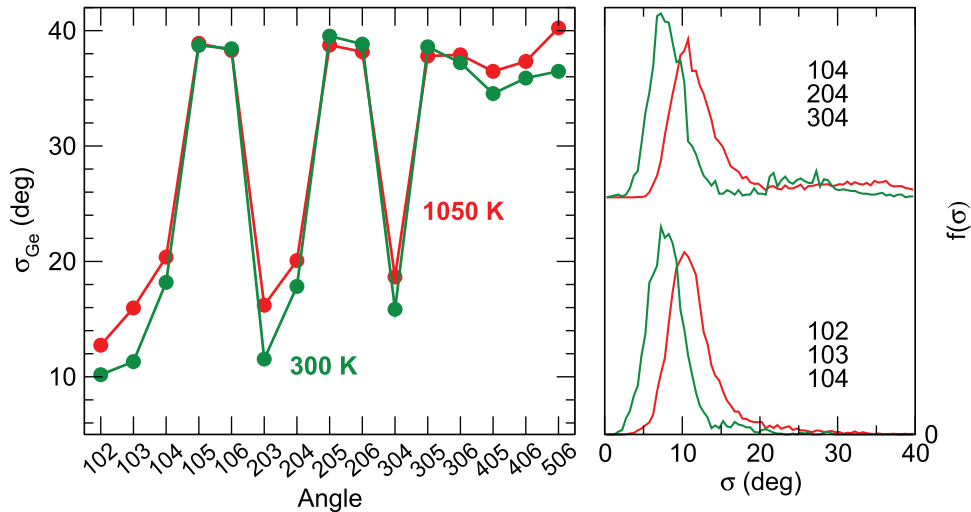


Figure 34. Effect of temperature on standard deviations in liquid (1050 K, red) and amorphous (300 K, blue) GeSe_2 . Left: Standard deviation σ_{Ge} extracted from the partial bond angle distributions (PBAD). Right: Distribution of Ge angular standard deviations using individual constraints. The total distributions are split, depending on the neighbor rank: angles involving the first three neighbors (102, 103, 203), and the fourth neighbor (104, 204, 304, shifted).

(104, 204, 304) partially soften and produce a bimodal distribution (red curve), indicative of the fact that some angular constraints ($\sigma \simeq 22^\circ$) are now broken. An enumeration shows that the fraction of broken constraints is about 17.2% and 21.4% for GeSe_2 and Ge_2Se_3 , respectively [282]. This implies a reduction of the number of Ge BB constraints so that n_c reduces from 3.67 (the mean-field estimate [61]) to 3.5, and from 4.00 to 3.74 for GeSe_2 and Ge_2Se_3 , respectively.

6.2. Behavior in the liquid phase

How do constraints in chalcogenide melts behave at high temperature, and how does the evolution of such constraints

link with relaxation? Using MD simulations, the number of topological constraints has been investigated as a function of temperature in a certain number of glass-forming systems such as GeSe_2 [314], Ge–Te [309], Ge–Si–Te [308] or SiO_2 – 2SiO_2 [274, 306, 310]. Figure 34 shows the analysis for 300 K and 1050 K for GeSe_2 , using either an average count (left) or individual constraints giving the distribution $f(\sigma)$ (right) [314]. Changes in constraints are weak and indicate that a counting at low temperature holds to some extent in a high temperature liquid, and close to the glass transition temperature. The corresponding calculated fraction of broken constraints [314] has been found to be of the same order which highlights the fact that thermal effects on topological

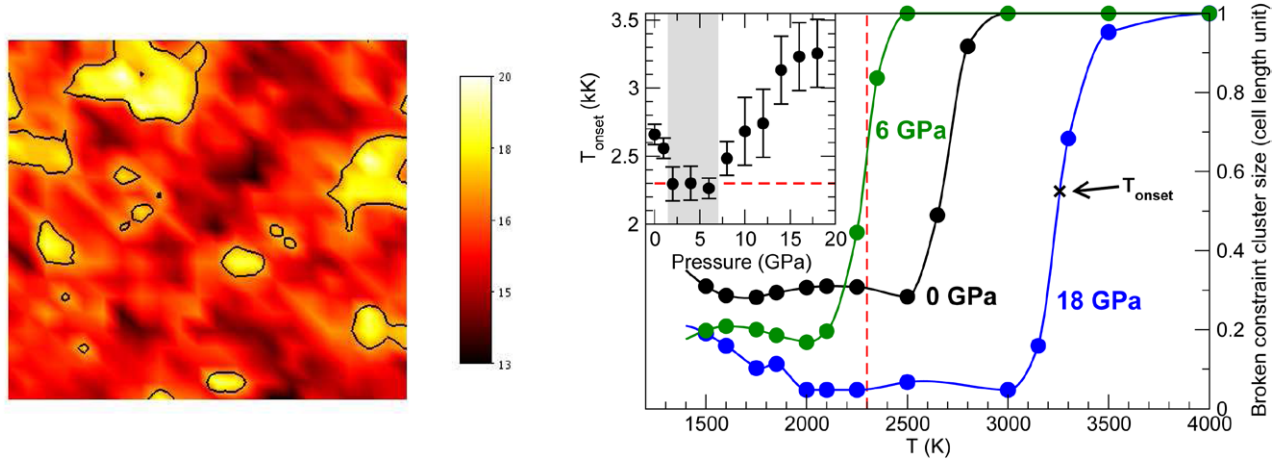


Figure 35. Left: Contour plot of the bridging oxygen standard deviation ($13^\circ < \sigma < 20^\circ$) in a ($P = 0$, 2000 K) sodium silicate liquid [317]. Yellow zones indicate regions of broken constraints. Right: size of the broken constraint clusters (in simulation cell length unit) as a function of temperature for different isobars. The inset shows the evolution of the onset temperature T_{onset} (in kK) as a function of pressure.

constraints are weak in these chalcogenides. This conclusion is consistent with recent results from neutron spin-echo spectroscopy showing that the rigidity concept (and the underlying constraint count) can be extended from the glass to the liquid [315]. Parameters giving the temperature dependence of the relaxation patterns of binary chalcogenide melts have, indeed, been shown to be linearly dependent with the mean coordination number \bar{r} , which represents a measure of a low temperature network for which the rigidity analysis assumes that all constraints are intact [60, 61]. This also seems in line with results in Ge–Se using liquid-state NMR [137] (see also figure 16), which emphasize that relaxational phenomena in the liquid are linked with the constraint count performed at low temperature.

This situation actually contrasts with the findings obtained for oxides (Figure 32) which exhibit a much more pronounced evolution of n_c with temperature (figure 24, left) or under a combined change in temperature and pressure (GeO₂, [316]). Furthermore, for such oxides, it has been found [317] that the distribution of constraints is not randomly distributed (figure 35, left), and corresponding liquids display a heterogeneous distribution with zones of thermally activated broken constraints that can be increased with temperature at constant pressure. In addition, the spatial extent of these flexible regions shows a percolative behavior at a characteristic temperature T_{onset} (figure 35, right) which is deeply connected to flexible to rigid transitions, and influences the fragility of the glass-forming liquid [317]. Here, the temperature at which constraints become homogeneously distributed across the liquid structure is found to depend both on pressure and temperature, with a minimum found at T_{onset} for a certain pressure interval.

6.3. Isostatic relaxation

Isostatic glasses are found to relax very differently from other glass-forming liquids, and the behavior of transport properties appears to be different too, as recently demonstrated for a densified silicate glass [310] using molecular simulations. It relies essentially on the computation of viscosity using

the Green–Kubo (GK) formalism [318] which is based on the calculation of the stress tensor auto-correlation function, given by:

$$\eta = \frac{1}{k_B T V} \int_0^\infty \langle P_{\alpha\beta}(t) P_{\alpha\beta}(0) \rangle \quad (55)$$

using off-diagonal components $\alpha\beta(\alpha, \beta) = (x, y, z)$ of the molecular stress tensor $P_{\alpha\beta}(t)$ defined by:

$$P_{\alpha\beta} = \sum_{i=1}^N m_i v_i^\alpha v_i^\beta + \sum_{i=1}^N \sum_{j>i}^N F_{ij}^\alpha r_{ij}^\beta \quad \alpha \neq \beta, \quad (56)$$

where the brackets in equation (55) refer to an average over the whole system. In equation (56), m_i is the mass of atom i , and F_{ij}^α is the component α of the force between the ions i and j , r_{ij}^β and v_i^β being the β component of the distance between two atoms i and j , and the velocity of atom i , respectively.

When such calculated viscosities are investigated [296] at fixed pressure/density as a function of inverse temperature in an Arrhenius plot, a linear behavior is obtained which allows one to extract an activation energy E_A . A similar procedure can be realized for diffusivity [319]. Both activation energies and diffusivities are found to display a minimum with pressure [69, 70] (figure 6). When the number of constraints is independently calculated [274, 310], it has been detected that the minimum in E_A coincides with $n_c = 3$ (figure 36(a)) suggesting that isostatic networks will lead to a singular relaxation behavior with weaker energy barriers, as also detected experimentally in, for example, Ge–As–Se [8] (figure 23) for which the condition $n_c = 3$ coincides with the mean coordination number of $\bar{r} = 2.4$ defining the condition of isostaticity. Given that one has $\mathcal{M} = E_A \ln_{10} 2 / k_B T_g$, the combination of a minimum in E_A and a smooth or constant behavior of T_g with thermodynamic conditions (pressure, composition) might lead to a minimum in fragility. Such observations have been made for certain chalcogenide melts [15, 41, 87] for which minima in E_A and \mathcal{M} coincide and, under certain assumptions regarding structure, the link with the isostatic nature of the network could be established [43, 47, 238].

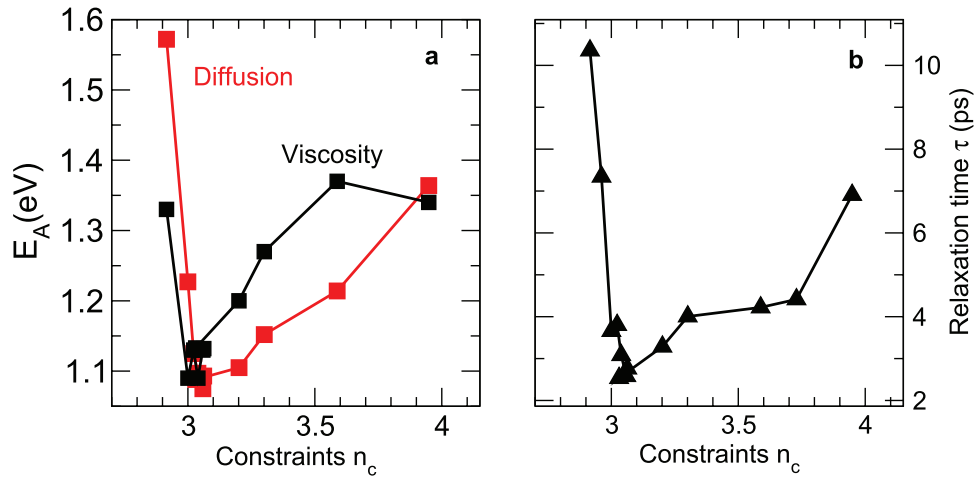


Figure 36. (a) Calculated activation energies E_A for diffusion (red) and viscosity (black) as a function of the number of constraints n_c [310], derived from an Arrhenius plot of oxygen diffusivity and Green–Kubo calculated viscosity in a densified sodium silicate. (b) Calculated relaxation time τ as a function of n_c determined from a separate evaluation of the viscosity and the instantaneous shear modulus [320].

These conclusions actually parallel those made from a simplified Kirkwood–Keating model of the glass transition [216] showing that isostatic glass-forming liquids have an activation energy for relaxation time which is minimum. In addition, a calculated relaxation time τ in the region of the glass transition for the same densified silicate (2000 K, [310]) has been found to evolve similarly. Indeed, a deep minimum is found in the relaxation time ($\tau \approx 2$ –3 ps) in the region where the system is nearly isostatic ($3.0 < n_c < 3.2$, figure 36(b)).

6.4. Reversibility windows

6.4.1. MD signature. Isostatic glasses, furthermore, display reversibility windows, i.e. a tendency to display a minimum of thermal changes at the glass transition which is obviously linked with the particular relaxation behavior (figure 36). When MD numerical cycles are performed across the glass transition from a high temperature liquid, one finds a hysteresis between the cooling and heating curve (figure 37(a)) in a similar fashion to the salient experimental phenomenology of the glass transition (figure 10). This behavior simply reflects the non-equilibrium nature of glasses that are able to slowly relax at $T < T_g$, and decrease volume or enthalpy as the glass is heated back to the liquid phase. However, it has been found [310] that for selected thermodynamic conditions (pressure) and fixed cooling/heating rate the hysteresis curves become minuscule, and the cooling/heating curves nearly overlap. When the area A_H (A_V) of the enthalpy (volume) hysteresis is investigated as a function of pressure or density (inset figure 37(a)), a deep minimum is found which reveals a so-called *reversibility window* (RW) [310, 321].

These thermal anomalies are actually linked with the isostatic nature of the glass-forming liquid, as detected from an MD-based constraint count (figures 37(b) and (c)). A calculation of the total number of constraints shows a plateau-like behavior at a value $n_c = 3$ between 3 GPa and 12 GPa, which can be put in parallel with the evolution of the hysteresis areas (figure 37(a)). The detail shows that angular (BB) adaptation

drives the mechanical evolution of the liquid under pressure because BS constraints increase due to the conversion [67] of silica-like tetrahedral order which prevails at ambient conditions, into octahedral order which dominates at elevated pressure, and which is typical of the short-range order of the crystalline stishovite polymorph [322]. However, at a pressure of about 3 GPa, the system attains an obvious threshold, and further compression leads to a decrease of the number of BB constraints which indicates that some of the angular interactions have softened. Upon further compression, this evolution holds up to a pressure of about 12 GPa, beyond which an important growth takes place. The results indicate an obvious correlation between the RW threshold pressures and those obtained from the constraint count, while identifying the isostatic nature of RW.

6.4.2. Experimental signature from calorimetry. There is actually strong experimental support for these findings connecting RW with the isostatic nature of the network structure, and vast literature has been accumulated on this topic during the last fifteen years. One of the most direct signatures of reversibility windows which has a nearly one-to-one correspondence with the result from MD (inset of figure 37(a)) comes from mDSC measurements (equation (16), figure 12) [236] which exhibit a minimum (figure 38) or even a vanishing (in selected cases, see figure 38(a)) of the non-reversing enthalpy ΔH_{nr} [324]. The sharp boundaries allow one to define a compositional window displaying these enthalpic anomalies (e.g. $23.5\% < x < 26.5\%$ in TeO_2 - V_2O_5 , figure 38(a), [323]), and these can also be evidenced to a lesser extent from the total heat flow and the heat capacity jump at the glass transition (figure 23, [8, 230]).

The use of such calorimetric methods to detect the nearly reversible character of the glass transition has not been without controversy, in part, because of the intrinsic measurement of ΔH_{nr} depends on the imposed frequency, and relates to the imaginary part of the heat capacity $C_p''(\omega)$ [116, 117]. Frequency corrections [325] have to be taken into account

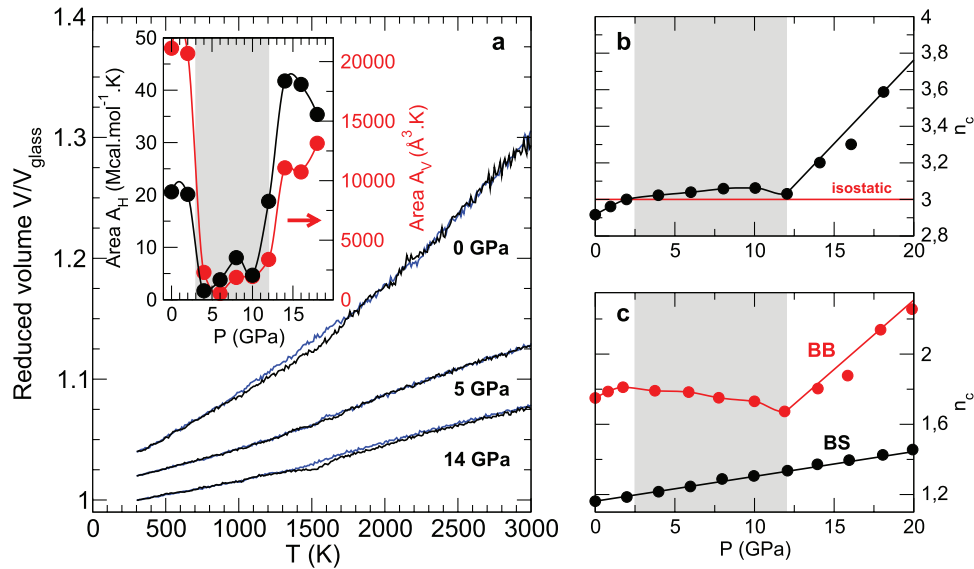


Figure 37. (a) Volume-temperature dependence during a cooling (blue) and heating (black) cycle for selected pressures in a liquid silicate [310] across the glass transition. The volumes have been rescaled with respect to their evolution in the glassy state V_{glass} . Curves at 0 GPa and 5 GPa have been shifted by multiples of 0.1. The cycle leads to a hysteresis which is due to structural relaxation, but is also controlled by rigidity. The inset shows the hysteresis area of the enthalpic (A_H) and volumetric (A_V , red curve, right axis extracted from the main panel) hysteresis as a function of the applied pressure P , defining a reversibility window (gray zone). (b) Calculated total number of constraints per atom. The horizontal red line represents the isostatic line $n_c = 3$, and separates flexible from stressed rigid networks. (c) Calculated number of oxygen stretching and bending constraints n_c^{BS} (black) and n_c^{BB} (red) as a function of pressure. The gray zone (reversibility window) in panel (b) and (c) refers to the one defined in the inset of panel (a).

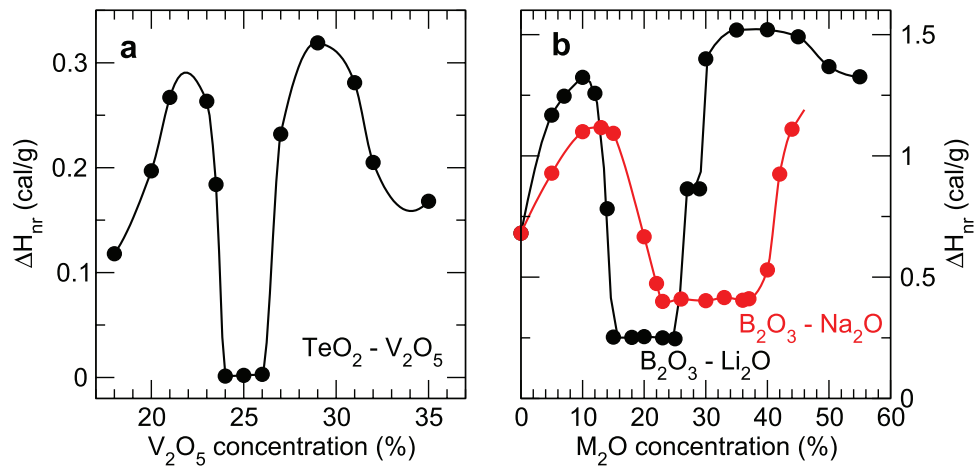


Figure 38. Measured non-reversing enthalpy ΔH_{nr} as a function of modifier content in telluro-vanadate ($\text{TeO}_2\text{-V}_2\text{O}_5$, [323]) and borate glasses ($\text{B}_2\text{O}_3\text{-M}_2\text{O}$, $\text{M} = \text{Li}, \text{Na}$ [54]). Note, the square-well behavior of ΔH_{nr} with composition, and the nearly constant value of ΔH_{nr} over select intervals in composition.

in order to avoid the spurious effects arising from the frequency-dependence of the specific heat [113]. Even with this frequency correction on the non-reversing heat flow leading to a neat measurement of ΔH_{nr} , results have been challenged by several authors who have argued that conclusions drawn from the observed anomalies (figure 38) might well be the result of a measurement artefact [58, 59, 326–328]. However, ΔH_{nr} appears to be not only sensitive to impurities and inhomogeneities [57], but also to the relaxation state of the glass [57, 329] so that the accurate detection, measurement and reproduction of ΔH_{nr} represent a true experimental challenge. Furthermore, it has been demonstrated that conclusions against the detection of an RW were based on samples

of unproven homogeneity [86, 329], as exemplified by the dependence of the fragility on the reaction time (figure 8).

A large number of network glasses (chalcogenides, oxides) display RWs, and these are summarized in figure 39. These represent systems which cover various bonding types, ranging from ionic (silicates [53]), iono-covalent, covalent (Ge-Se , [43]), or semi-metallic (Ge-Te-In-Ag [339]). In a certain number of these systems, e.g. for the simple binary network glasses such as $\text{Ge}_x\text{S}_{1-x}$ or $\text{Si}_x\text{Se}_{1-x}$, the experimental boundaries of the RW are found to all be very close [43, 47, 238], i.e. located between $20\% < x < 25\%$, and aspects of topology fully control the evolution of rigidity with composition, given that there is a weak effect in the case of isovalent Ge/Si or S/Se

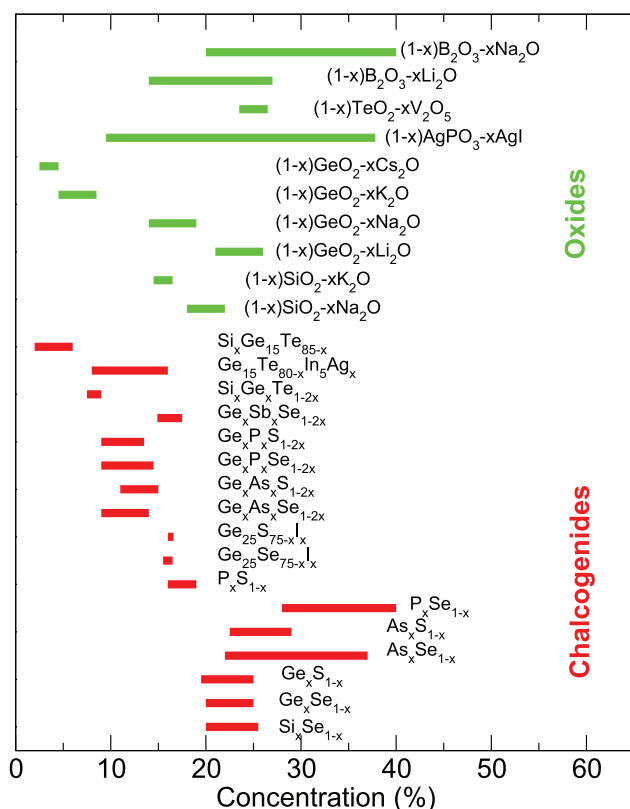


Figure 39. Location of experimental reversibility windows (RW) driven by composition for different chalcogenide and modified oxide glass systems [310]: Si–Se [238], Ge–Se [43], Ge–S [47], As–Se [41], As–S [330], P–Se [331], P–S [332], Ge–Se–I [333], Ge–S–I [334], Ge–As–Se [243], Ge–As–S [335], Ge–P–Se [244], Ge–P–S [336], Ge–Sb–Se [337], Si–Ge–Te [309, 338], Ge–Te–In–Ag [339], $\text{SiO}_2\text{--M}_2\text{O}$ ($\text{M} = \text{Na}, \text{K}$) [53], $\text{GeO}_2\text{--M}_2\text{O}$ ($\text{M} = \text{Li}, \text{K}, \text{Cs}$) [340], $\text{GeO}_2\text{--Na}_2\text{O}$ [341], $\text{AgPO}_3\text{--AgI}$ [134], $\text{TeO}_2\text{--V}_2\text{O}_5$ [323] and $\text{B}_2\text{O}_3\text{--M}_2\text{O}$ ($\text{M} = \text{Li}, \text{Na}$) [54]. In the same families of modified oxides (e.g. borates, see figure 38(b)), there is an effect due to the cation size. Using the 8- \mathcal{N} (octet) rule, the location of RWs can be represented in select systems (Group IV chalcogenides) as a function of the number of constraints n_c using the mean-field estimate of n_c (equation (39)). Permission from the American Physical Society.

substitution. This compositional interval defining the RW connects to the mean-field estimate of the isostatic criterion (equation (41)) satisfying $n_c = 3$ because coordination numbers of Ge/Si and S/Se can be determined from the 8- \mathcal{N} (octet) rule to yield an estimate of the constraints $n_c = 2 + 5x$ using equation (39). In fact, for these IV–VI glasses, the lower boundary of the RW ($x_c = 20\%$) coincides with the Phillips-Thorpe [60, 61] mean-field rigidity transition $n_c = 3$ and $\bar{r} = 2.4$.

For most of the systems however, uncertainties persist regarding the constraint count (equation (39)) derived from the local structures and geometries. Coordination numbers and related active/inactive constraints must be derived from specific structural models, and this becomes immediately apparent when Group V selenides/sulphides are considered (figure 39) because different RW locations are found for isovalent compounds, e.g. differences emerge between As- and P-bearing chalcogenides, and between sulphides and selenides (e.g. P_xS_{1-x} and $\text{P}_x\text{Se}_{1-x}$, [336]). Local structural features have been put forward to explain the trends due to

chemistry [41, 330–332], as well as the special effect of sulfur segregation in sulphide-rich glasses, and these have also served the characterization of related ternaries [243, 335–336]. The validity of these structural models is still debated in the literature, although rather well established in some cases from spectroscopic studies [331, 332]. The above statements seem to remain valid when the tellurides are considered. Because of the increased electronic delocalization of the Te atoms, Group IV and V atoms do not necessarily follow the 8- \mathcal{N} rule and lead to mixed local geometries that are now composition dependent [342, 343], e.g. sp^3 tetrahedral and defect-octahedral for Ge atoms, so that a proper constraint count must rely on accurate simulations, in conjunction [305, 306] with MD-based constraint counting algorithms such as those derived above. RWs have also been measured in modified oxides for which the connectivity change is realized by the addition of modifiers which depolymerize the network structure (figure 1). As a result, the same phenomenology is found, and RWs have been detected between the two possible end limits of networks or elastic phases, i.e. strongly depolymerized and flexible (e.g. pyrosilicates $\text{SiO}_2\text{--}2\text{Na}_2\text{O}$) or highly connected and stressed rigid (e.g. silica-rich silicates).

6.4.3. Alternative signatures of RWs. The presence of a peculiar relaxation phenomena that induce RWs for select compositions leads to various other anomalous behaviors—maxima or minima in physical properties—in the glassy state. These provide other alternative and complementary evidence of the RW signature from calorimetric (mDSC) measurements. Figure 40 displays a survey of some of these properties for three families of modified glasses with widely different chemical bonding, although they display similar features in terms of rigidity: covalent $\text{Ge}_x\text{Se}_{1-x}$ [43, 344], ionic $(1-x)\text{AgPO}_3\text{--}x\text{AgI}$ [134, 345] and iono-covalent $(1-x)\text{GeO}_2\text{--}x\text{Na}_2\text{O}$ glasses [341]. When the atomic sizes are comparable (e.g. $d_{\text{Ge}} = 1.22 \text{ \AA}$, and $d_{\text{Se}} = 1.17 \text{ \AA}$ for the covalent radius in Ge–Se), it has been suggested that glasses will display an increased tendency towards space-filling because of the isostatic nature of the networks (i.e. absence of stress [344]), which manifests by a minimum in the molar volume (figures 40(a) and (c)), a salient feature that has been reported for various systems [15, 41–43, 308, 323, 341, 346]. The stress-free nature of such RWs has been detected from pressure experiments [344] showing the vanishing of a threshold pressure (figure 40(a)) prior to a pressure-induced Raman peak shift. This peak shift usually serves to quantify and to measure residual stresses in crystals. Ionic conductors (figure 40(b)) display an onset of ionic conduction only in compositions belonging to the flexible phase, i.e. when the network can be more easily deformed at a local level because of the presence of floppy modes [134] which promote mobility. This leads to an exponential increase in the conductivity. However, it is to be noted that in RWs an intermediate conductive regime sets in, which also shows an anomalous behavior for a typical jump distance associated with dynamics [347]. Other quite different probes have also revealed the signature of RWs such as DC permittivity (figure 40(b)) [134] or the frequency [341] associated with the imaginary part of the complex dielectric function (IR-TO, figure 40(c)).

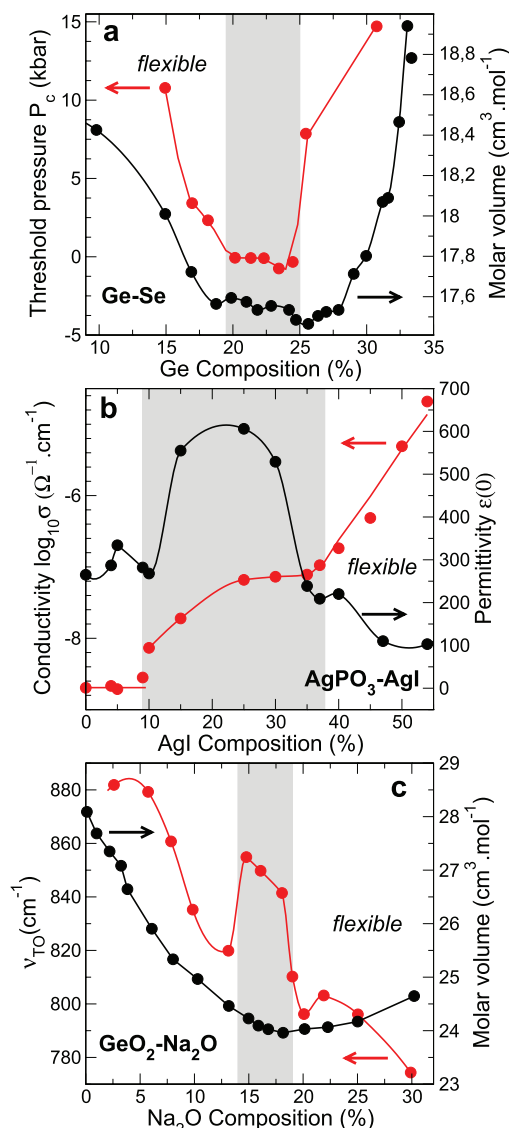


Figure 40. Different quantities showing an anomalous behavior in reversibility windows [70]. (a) Raman threshold pressure [344] and molar volume [43] (right axis) in Ge_xSe_{100-x} as a function of Ge composition. (b) Ionic conduction and zero-frequency permittivity [134] in (100-x)AgPO₃-xAgI as a function of AgI composition [134]. (c) IR-TO vibrational frequency and molar volume (right axis) in (100-x)GeO₂-xNa₂O as a function of Na₂O composition [341]. The gray areas correspond to the reversibility windows determined from calorimetry (mDSC), such as in figure 38. Permission from Wiley and Sons 2015.

6.4.4. Insight from models: evidence for an elastic intermediate phase. A certain number of scenarios have been proposed to describe the observed behaviors depicted in figures 38 and 40, and some emphasize the role of fluctuations [348–351] in the emergence of a double threshold/transition that define an intermediate phase (IP) between the flexible and the stressed rigid phase. Alternatively, mean-field aspects of jamming have been considered, and, here, fluctuations in, for example, coordinations are thought to be limited, but atoms are coupled spatially via elasticity and can organize locally into distinct configurations that may promote an IP.

Given the link between isostaticity [310] and reversibility at the glass transition (figures 37 and 39), and following the

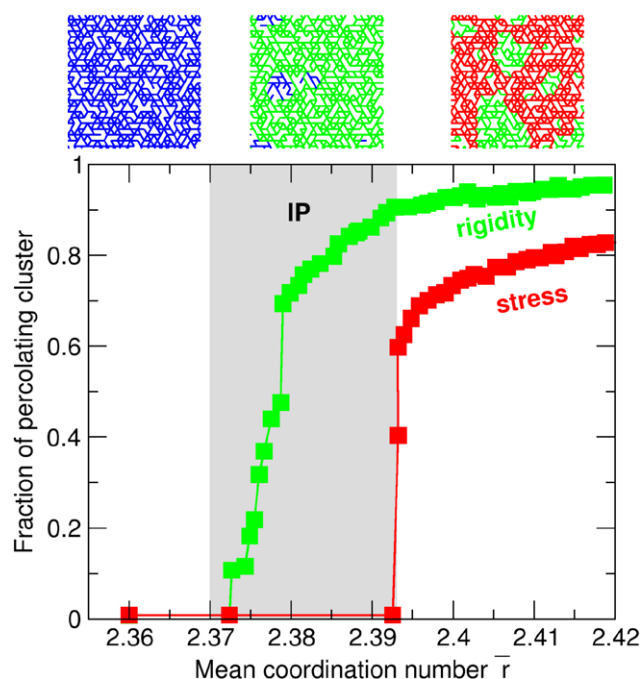


Figure 41. Evidence of a stress-free intermediate phase from the pebble game analysis (adapted from [348, 352]). Fraction of sites on isostatically rigid and stressed rigid percolating cluster in a self-organized network as a function of the network mean coordination number \bar{r} . The intermediate phase which is rigid, but unstressed, exists in these classes of model between $2.375 \leq \bar{r} \leq 2.392$, and coalesces in random networks. This generic behavior is also observed from a spring network [354] (top) showing regions which are flexible (blue), isostatic (marginally constrained, green) and stressed rigid (red). Permission from the American Physical Society.

path based on coordination fluctuations, several authors have attempted to modify the modeling of the initial mean-field theory [60, 61] that leads to a solitary phase transition when $n_c = 3$ (or $\bar{r} = 2.4$ if all BS and BB constraints are considered as intact). These contributions usually assume that amorphous networks will adapt during the cooling through the glass transition, similarly to the angular adaptation revealed from MD [282, 310], in order to avoid stress from additional cross-linking elements.

Using a graph-theoretical approach, Thorpe and colleagues [348, 352] have developed an algorithm (a pebble game, [353]) that takes into account the non-local characteristics of rigidity, and allows one to calculate the number of floppy modes, to locate over-constrained zones of an amorphous network, and ultimately identify stressed rigid clusters for simple bar-joint networks. In the case of simulated self-organized or adaptive networks, the addition of bonds in a network with increasing average connectivity will be accepted only if this leads to isostatically rigid clusters, so that the emergence of stressed rigid clusters is delayed. However, with a steady increase in the connectivity, the network will undergo percolation of rigidity (a rigidity transition at \bar{r}_{c1}) which leads to an unstressed (isostatic) structure (figure 41). The addition of new bonds will contribute to the occurrence of stressed rigid clusters that finally percolate at a second transition (\bar{r}_{c2}), identified with a stress transition, and both transitions define a window in connectivity $\Delta\bar{r} = \bar{r}_{c2} - \bar{r}_{c1}$, and an IP.

Other approaches have built on the same idea, using either a spin cavity method [349] or cluster expansions [350, 355]. These theories lead to a solitary floppy to rigid transition in the absence of self-organization, and to an intermediate phase corresponding to a window in composition/connectivity in which the network is able to adapt in order to lower the stress due to constraints. However, some of these models do not take into account the fact that rigid regions cost energy and, thus, correspond to an infinite temperature. Also, the pebble game [348] and the cavity method [349] apply in $T = 0$ networks which have infinite energy barriers for bond change/removal. Thermal effects have been included [268, 351] and an equilibrated self-organized IP has been recovered for two-dimensional lattice-based models. An important outcome from these models is that an increased sensitivity for single bond addition or removal exists close to the IP, and this suggests that the system is maintained in a critical state on the rigid-floppy boundary throughout the IP.

Instead, using the phenomenology of the elasticity of soft spheres and jamming transitions, Wyart [354] and colleagues have shown that the RW could occur in a certain number of physical situations by considering a lattice spring model for rigidity transitions with weak noncovalent (van der Waals) interactions [220, 356, 357]. It reveals that the temperature considerably affects the way an amorphous network becomes rigid under a coordination number increase, and the existence of an isostatic reversibility window not only depends on T , but also on the relative strength of the weak forces. In a strong force regime, an RW can be found which is revealed by a finite width in the probability to have a rigid cluster spanning the system, driven by fluctuations in coordination, similarly to the results of the pebble game ([353], figure 41). However, when weak interactions are present, the RW disappears below a certain temperature suggesting that the transitions become mean-field at low temperature and coalesce. Furthermore, weak interactions lead to an energy cost for coordination number fluctuations, which decay at finite temperature. These results are partially supported by MD simulations [310] taking into account long-range interactions (Coulomb, van der Waals) allowing one to probe the weak-force regime. Here, coordination fluctuations are found to be small given the weak abundance of five-fold Si atoms (10–20%) [296], and fluctuations are essentially found in angular constraints which show a non-random distribution (figure 35, [317]). However, the vibrational analysis [354] suggests that the IP vibrational modes are similar to the anomalous modes observed in the packing of particles near jamming, thus providing an interesting connection with the jamming transition [4] that might also be embedded in the anomalous variation of the molar volume (figures 40(a) and (c)).

This mean-field scenario for the IP is also the one followed [358] in a rigidity percolation model on a Bethe lattice [359–361] that is based on a binary random bond network with a possibility of having two types of degrees of freedom. Under certain conditions, two discontinuous transitions are found, and the associated IP displays an enhanced isostaticity at the flexible boundary. As a result, the entire IP has a low density of redundant bonds and has, therefore, a low

self-stress. The double transition solution is found to depend on the coordination and the degrees-of-freedom contrast, and might be directly comparable to experiments although important coordination contrasts do not necessarily correspond to situations encountered in, for example, chalcogenides [43].

Although some other models [328, 362] with a weaker theoretical basis have argued that the existence of the IP remains elusive, albeit contradicted by the variety of experimental signatures, there is a strong theoretical and numerical indication that RW or IP glasses display particular relaxation kinetics manifesting in ΔH_{tr} that leads to anomalous properties in different physical properties (figure 40). These findings actually have a much more universal ground because links between the RW and protein folding [363], high temperature superconductors [364] or computational phase transitions [365] have been stressed. Such strong analogies simply underscore the fact that a complex network with external constraints/conditions has the ability to lower its energy by adapting internal thermodynamic variables.

7. Numerical methods

As already mentioned in the previous sections, MD simulation is the method of choice to investigate aspects of glassy relaxation in relation to structure, this relationship being central to the case of network-forming liquids. Rather than presenting the basis of computer simulations (see [366–368]), we discuss which tools have been developed for an increased understanding of glassy relaxation.

In an MD simulation, the trajectories (i.e. the positions $\mathbf{r}_i(t)$ of N particles with $i = 1 \dots N$) serve as a starting point for further investigations regarding, for example, relaxation. Here, $\mathbf{r}_i(t)$ are obtained by solving Newton's equations of motion for a given system using, for example, the well-known Verlet algorithm:

$$\mathbf{r}_i(t + \Delta t) = \mathbf{r}_i(t) + \mathbf{v}_i(t)\Delta t + \frac{(\Delta t)^2}{2}\mathbf{F}_i(t) \quad (57)$$

where

$$\mathbf{v}_i(t + \Delta t) = \mathbf{v}_i(t) + \frac{\Delta t}{2} [\mathbf{F}_i(t) + \mathbf{F}_i(t + \Delta t)] \quad (58)$$

and $\mathbf{F}_i(t)$ is the force acting on atom i , and is derived from an interaction potential that has been fitted in order to reproduce some of the properties of the system of interest. Δt is the time step for the integration of the equations of motion (typically 1 fs in classical MD [368]), and usually several orders of magnitude lower than the typical atomic vibrational frequency. There are intrinsic limitations with the MD method which concern timescales and size. For the latter aspect, with the available computer power, one is able to investigate systems of up to 10^7 atoms, whereas the timescale will be limited to the μs domain. This means that the glass transition can only be partially addressed using these methods, and is limited to the liquid-to-supercooled domain, i.e. to temperatures having, as close as possible, a relaxation time of $\tau \simeq 1 \mu\text{s}$.

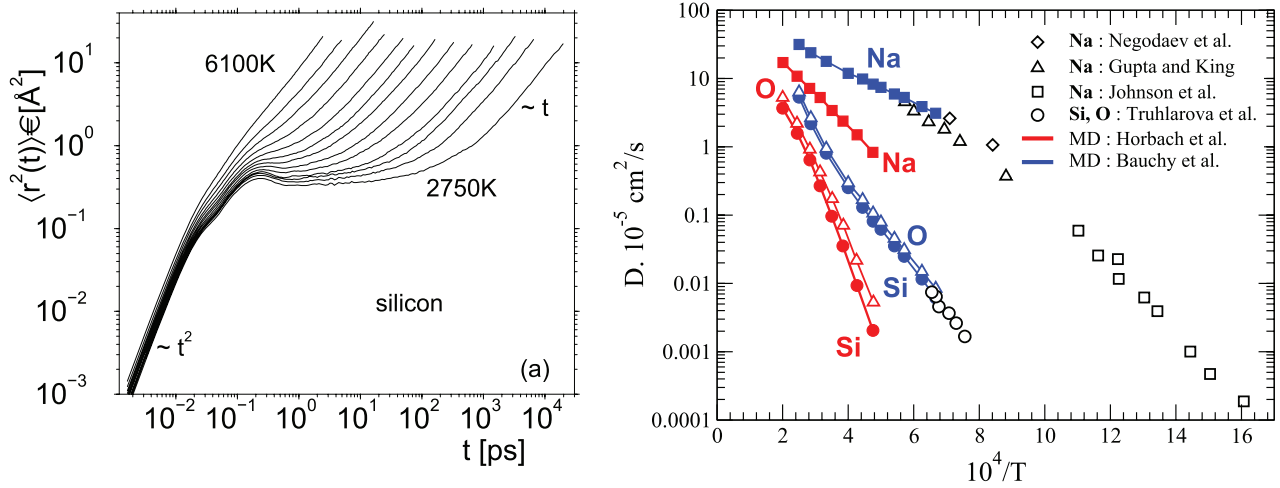


Figure 42. Left: time dependence of the silicon mean-squared displacement for different temperatures in liquid silica [369]. Permission from the American Physical Society. Right: computed diffusion constants D_{Na} , D_{Si} and D_{O} in a sodium silicate liquid as a function of inverse temperature (blue curves and symbols), compared to experimental data for D_{Na} (see [296] for references) and to the simulated values of D_{Na} , D_{Si} and D_{O} using an alternative potential (red curves and symbols, Horbach *et al* [370]). Permission from Elsevier 2015.

From these trajectories $\{\mathbf{r}_i(t)\}$, different properties of the supercooled liquid can be directly calculated, at least in principle, while also connecting with aspects of structure or constraints (figure 27). This is an important reason for their use, and this has motivated a lot of research in recent years.

7.1. Dynamic observables

7.1.1. Diffusion and viscosity. A useful means for the investigation of the dynamics of the glass-forming liquid is given by the investigation of the mean-square displacement of an atom of type α :

$$\langle r^2(t) \rangle = \frac{1}{N_\alpha} \sum_{i=1}^{N_\alpha} |\mathbf{r}_i(t) - \mathbf{r}_i(0)|^2, \quad (59)$$

where the brackets indicate ensemble averages. The behavior of $\langle r^2(t) \rangle$ with time and temperature displays some generic behaviors. At high temperature and short times, the motion of the atoms is usually governed by a ballistic regime for which $\langle r^2(t) \rangle$ scales as t^2 . At long times the dependence of $\langle r^2(t) \rangle$ becomes linear (figure 42, left) and signals the onset of diffusion, with a diffusion constant that follows Einstein's relation $\lim_{t \rightarrow \infty} \langle r^2(t) \rangle / 6t = D$. In a multicomponent liquid, one can thus have access to the diffusion constants D for different species, and these are represented in figure 42 (right) for, as an example, sodium silicates in an Arrhenius plot. The present figure is quite instructive because it also signals that a change in the force field [371, 372] used for the MD simulations can lead to behaviors that can be quite different, and diffusion constants can differ by at least one order of magnitude, and may, therefore, disagree in some cases with experimental measurements.

With decreasing temperature and the slowing down of the dynamics, the mean-square displacement reveals some additional features (figure 42 left) because $\langle r^2(t) \rangle$ still extends to the diffusive regime for the longest simulation times, but in addition shows a plateau-like behavior. This feature appearing

at intermediate times is due a cage effect created by neighboring atoms which trap the tagged atom during a certain time interval (e.g. 0.1 ps–100 ps for 2750 K silica, see figure 42, left), the typical distance associated with this phenomenon being of the order of a fraction of Å ($\langle r^2(t) \rangle \simeq 0.1\text{--}1 \text{ Å}^2$), i.e. somewhat smaller than a typical bond distance. For sufficiently long times, however, the atom is able to escape from that cage, and diffusion sets in.

Once the diffusion constant is determined, it has been found that most of these simulated network-forming liquids display an Arrhenius dependence (figure 42, right) for the diffusivity [71, 285, 296, 369, 370, 373] leading to an estimate of an activation energy E_A (e.g. figure 6 or 36) that is found to be close to experimental findings (e.g. $E_A = 4.66 \text{ eV}$ in silica [369], compared to the experimental 4.70 eV [374, 375]). For selected systems, simulation data exhibit a significant curvature in diffusivity at higher temperatures [285, 369] that has been interpreted as reminiscent of the more fragile behavior of the liquids [369] once T increases.

At high temperature, the evolution of diffusivity parallels that found for calculated viscosities η using the Green–Kubo formalism and equations (55)–(56) which is also found to be Arrhenius-like, and corresponding activation energies E_A are similar (see figure 36). This simply reveals that the Stokes–Einstein relationship holds:

$$D\eta = \frac{T}{6\pi R}, \quad (60)$$

where R is the particle radius ($\simeq \text{Å}$) moving in a fluid. Alternatively, the phenomenological Eyring equation can be used:

$$\eta = \frac{k_B T}{\lambda D}. \quad (61)$$

Here, λ represents a typical jump distance in the liquid, of the order of a bond distance. It has been shown [376, 377] that the Eyring equation works well with viscous liquids such as silicates with a high silica content provided that λ is taken as the

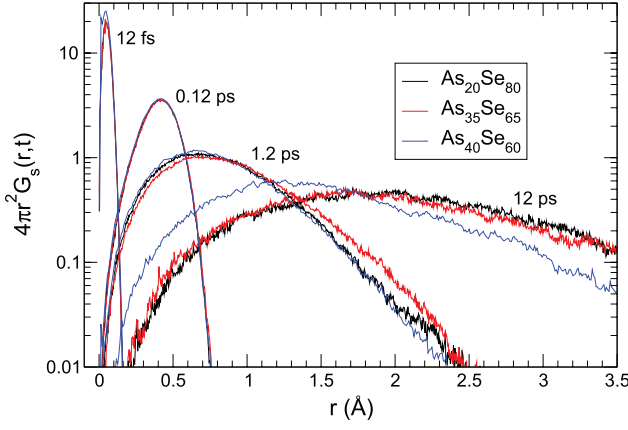


Figure 43. Calculated self part of the van Hove correlation function $4\pi r^2 \mathcal{G}_s^{\text{Se}}(r, t)$ at 800 K for three selected compositions in As–Se liquids [71]: flexible $\text{As}_{20}\text{Se}_{80}$ (black), intermediate $\text{As}_{35}\text{Se}_{65}$ (red) and $\text{As}_{40}\text{Se}_{60}$ (blue). The function is represented for selected times: 12 fs, 0.12 ps, 1.2 ps, 12 ps. Permission from AIP Publishing LLC 2015.

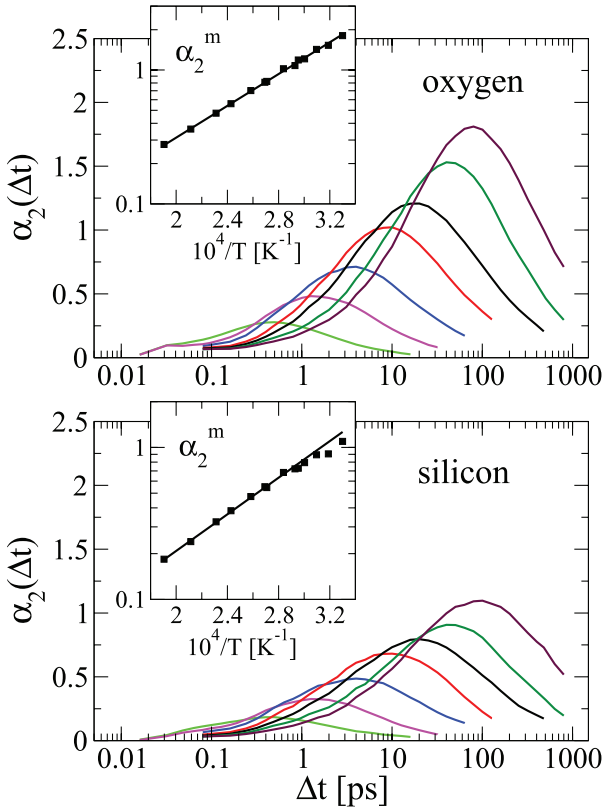


Figure 44. Non-Gaussian parameter α_2 for oxygen and silicon atoms at various temperatures in liquid silica [382]. The insets show the temperature dependence of the maximum of α_2 which follows an Arrhenius law. Permission from the American Physical Society 2015.

oxygen–oxygen mean distance, a result that was also checked numerically for two other silicate liquids [296].

7.1.2. Van Hove correlation function. An additional signature of the dynamics is given by the van Hove correlation function which probes in real space, rather than the average value (equation (59)), the distribution of distances over which

the particle has moved during a time t . This is conveniently quantified by the self part of the van Hove correlation function defined as:

$$\mathcal{G}_s^\alpha(r, t) = \frac{1}{N_\alpha} \left\langle \sum_{k=1}^{N_\alpha} \delta(r - |\mathbf{r}_k(0) - \mathbf{r}_k(t)|) \right\rangle \quad (62)$$

where $\delta(r)$ is the Dirac function. This function $\mathcal{G}_s^\alpha(r, t)$ is the probability density of finding an atom α at time t knowing that this atom was at the origin ($r = 0$) at time $t = 0$. By probing the probability that an atom has moved by this distance r , one is, therefore, able to gather additional information about dynamics. Figure 43 shows such a function ($4\pi r^2 \mathcal{G}_s^{\text{Se}}(r, t)$) for liquid As_2Se_3 [71] at fixed temperature for different times. Note that because of the isotropic nature of the system, the angular integration can be performed leading to the term $4\pi r^2$. It is seen that for very short times (12 fs), $4\pi r^2 \mathcal{G}_s^{\text{Se}}(r, t)$ nearly reduces to the Dirac function as it should do [378], given the definition of $\mathcal{G}_s(r, t)$ (equation (62)). For increased times however, the Se atoms now experience larger distances for a given time, and for $t = 12$ ps, atoms move over distances typical of second nearest neighbor distances (4–5 Å). The second important characteristic that appears from figure 43 is that the distribution is not Gaussian for long times as would be expected for an ordinary liquid for which relaxation phenomena are negligible [378]. In this simple case, the mean-square displacement is, by definition, the second moment of the van Hove function which behaves as:

$$\mathcal{G}_s(r, t) = \frac{\exp\left[-\frac{r^2}{4Dt}\right]}{(4\pi Dt)^{3/2}} \quad (63)$$

Here, the function appears to be much wider with tails in the long time limit that have been revealed by a series of simulations of network-forming liquids (silica [379], As_2Se_3 [71], densified silicates [319]). For short times, however, the van Hove function is made of a single Gaussian distribution that is shifted to the right with increasing time, and the location of the maximum evolves as t^2 , which arises from the ballistic behavior of $\langle r^2(t) \rangle$ (figure 42, left). This characteristic does not apply at intermediate times, but it recovered at very long times, for which $\mathcal{G}_s(r, t)$ is again given by a Gaussian. A convenient way to characterize the departure from such distributions is given by the non-Gaussian parameter [380]:

$$\alpha_2 = \frac{3\langle r^4(t) \rangle}{5\langle r^2(t) \rangle^2} - 1 \quad (64)$$

which becomes non-zero at intermediate times (figure 44) when $\langle r^2(t) \rangle$ exhibits a plateau-like behavior (figure 42, left), and which is directly related to the cage effect when neighboring atoms act as a trap for a moving particle. Current investigations have focused on glass-forming liquids such as water [381], silica [193, 382, 383] or aluminosilicates [384], and have established the correlation between the onset of the β -relaxation plateau (figure 14) and departure ($\alpha_2 \neq 0$) from a Gaussian distribution in the r -dependence of $\mathcal{G}_s(r, t)$. In addition, the large r tail seen in the van Hove correlation function

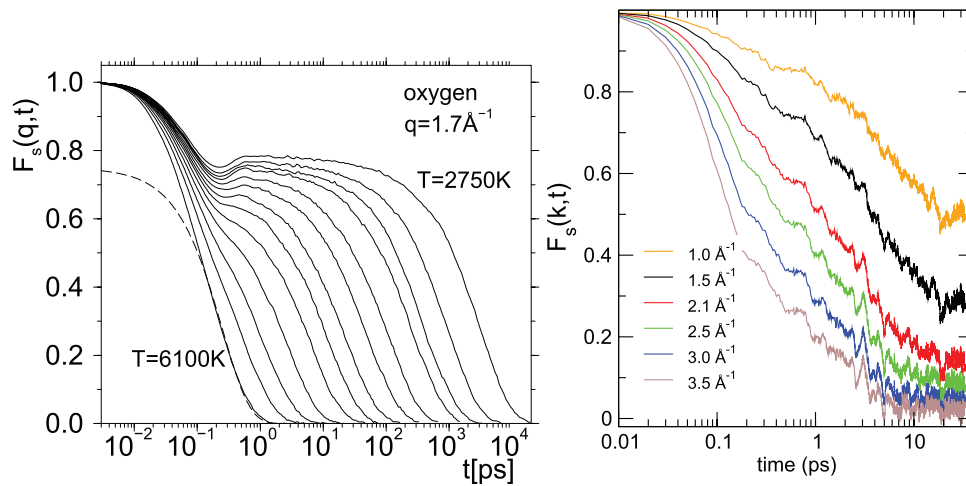


Figure 45. Left: Time dependence of the oxygen-related intermediate scattering function $F_s(q, t)$ at different temperatures investigated [388]. The wavevector q is 1.7 \AA^{-1} , the location of the first peak in the structure factor. Permission of the American Physical Society. Right: same function $F_s(q, t)$ at fixed temperature (1050 K) in liquid GeSe_2 for different wavevectors q . Note that the timescale of GeSe_2 is significantly reduced because of a different modeling scheme (*ab initio* MD).

[385, 386] can also be rather well described [387] by an exponential decay of the form $\mathcal{G}_s(r, t) \simeq \exp(-r/\lambda(t))$ which signals that viscous liquids will differ quite markedly from a high temperature liquid exhibiting a standard Fickian diffusion and a van Hove function of the form of equation (63). One of the main conclusions of such studies is that the dynamics of the atoms at long times and low temperature, i.e. those which contribute to the tail of $\mathcal{G}_s(r, t)$ have non-trivial dynamics that can be further characterized using dynamic heterogeneities (see below), and seem to contain some universal features that are common to network glasses, colloids, grains or simple sphere systems [387].

7.1.3. Intermediate scattering function. As described above, scattering experiments using, for example, neutron diffraction (figure 15) are performed in reciprocal space and can, therefore be compared to the calculated analog of the intermediate scattering function (equation (18)) which directly uses the positions $\mathbf{r}_i(t)$ obtained from the MD trajectory.

Such functions actually display the same phenomenology as the experimental ones, i.e. they exhibit a single Debye-like decay at high temperature, and lead to a β -relaxation plateau at lower T which extends beyond the available computer timescale at low temperature (figure 45, left). For intermediate temperatures, however, the structural (α) relaxation can be investigated and its characteristic (τ , Kohlrausch exponent β , see figure 14) determined as a function of the wavevector, temperature, etc and correlated with other calculated structural properties, e.g. τ being a decreasing function of the wavevector (figure 45, right).

Figure 45 shows such an example in liquid silica [388] and liquid GeSe_2 for different temperatures and wavevectors. It is seen that $F_s(k, t)$ behaves very similarly to the schematic figure represented (figure 14). As the temperature effects are considered, it is seen that $F_s(k, t)$ rapidly decays to zero at high temperature, and also reproduces the anticipated Debye single exponential. At low temperature, the usual two-step relaxation process is found that permits one to detect an α -relaxation

for the longest times. A rescaling of the x -axis using an α -relaxation time $\tau(T)$ defined by $F_s(k, \tau(T)) = e^{-1}$ usually permits one to detect the two temperature regimes that appear as a function of temperature. At high temperatures, such curves $F_s(k, t)$ fall, at long times, rather well onto a master curve that is accurately reproduced by a simple exponential. At low temperature, all curves also nearly overlap, but are reproduced this time by a stretched exponential [388].

The exponential appearing in the definition of the intermediate scattering function (equation (18)) can actually be expanded in $\langle r^2(t) \rangle$ and connects back to the β -relaxation and effects due to non-Gaussian dynamics. In fact, equation (18) rewrites [389]:

$$F_s(k, t) = \exp\left(-\frac{k^2 \langle r^2(t) \rangle}{6}\right) \times \left[1 + \frac{1}{2} \left(-\frac{k^2 \langle r^2(t) \rangle}{6}\right)^2 \alpha_2(t) + \dots\right] \quad (65)$$

where $\alpha_2(t)$ is the non-Gaussian parameter given in equation (64) that can be accessed from measurements/calculations of $F_s(k, t)$ at different wavevectors (figure 45, right). A certain number of limiting cases are interesting and useful for further analysis. For instance, in the time interval where $F_s(k, t) \gg e^{-1}$, the quantity $k^2 \langle r^2(t) \rangle / 6$ is small, and the intermediate scattering function reduces to a single exponential that is equal to $\exp[-k^2 \langle r^2(t) \rangle / 6]$ and can be directly obtained from the Fourier transform of the ‘Fickian’ van Hove function (equation (63)), a condition that is also met when $\ln[F_s(k, t)]/k^2$ is independent of k .

Given the timescale involved, investigations of the glassy relaxation using the intermediate scattering functions have been essentially made on model glasses (soft, hard) sphere glasses or model network glasses [390, 391], and for selected cases on oxides: borosilicates [300] silicates at ambient [392, 393] or under pressure [310], borates [394], calcium aluminosilicates [395] because classical MD simulations can be performed with confidence. In this case, the dynamics are explored on timescales (ns– μ s) which are of the order of the

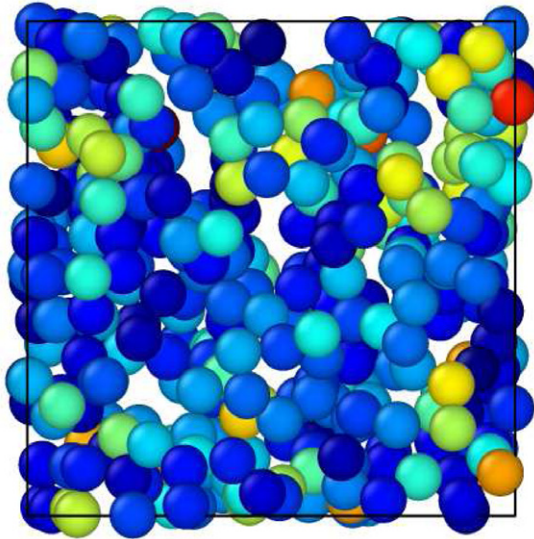


Figure 46. Atomic snapshot of liquid (1050 K) GeSe_2 [397] showing the particle displacements over 88 ps. Different color codes, from dark blue (1 Å) to yellow-red (12 Å) indicate that the displacement of the particles is not homogeneously distributed.

timescale probed in neutron diffraction experiments [82]. This situation contrasts with the one encountered in chalcogenides for which *ab initio* simulations are necessary [396] to account for structural defects and for charge transfer defining the covalent bonds (see, however, figure 45, right), which considerably reduces the timescale (≈ 100 ps). The dependence of $F_s(k, t)$ with wavevector shows that probing the relaxation on larger length scales (i.e. smaller k) leads to reduced dynamics, i.e. $F_s(k, t)$ decays more slowly, and eventually does not fall to zero for the largest computation time.

7.2. Dynamic heterogeneities

An inspection of the local displacements during simulations (figure 46) highlight the fact that the relaxation at the atomic scale is not homogeneous, and evidence has been found numerically that the dynamics are made of vibrations around well-defined positions followed by jumps once atoms have been able to escape from cages. In this respect, the existence of non-Gaussian dynamics [387] that connect to the β -relaxation plateau of the function $F_s(k, t)$ represent a strong indication that one has a distribution of relaxing events that vary with space and time, and emphasize the central role of dynamic fluctuations in the viscous slowing down.

7.2.1. Space and time fluctuations. Detailed features about this slowing down have emerged in the more recent years, and studies provide strong evidence for the existence of these dynamic fluctuations in time and space, now also known as ‘dynamic heterogeneity’ [398]. Simply speaking, one attempts both from experimental and theoretical measurements and signatures [385, 399–401] to quantify the fact that regions in the glass-forming liquid can have different relaxation rates to equilibrium, and that these rates will evolve in a non-trivial way with time and temperature. This is thought to lead to a rather

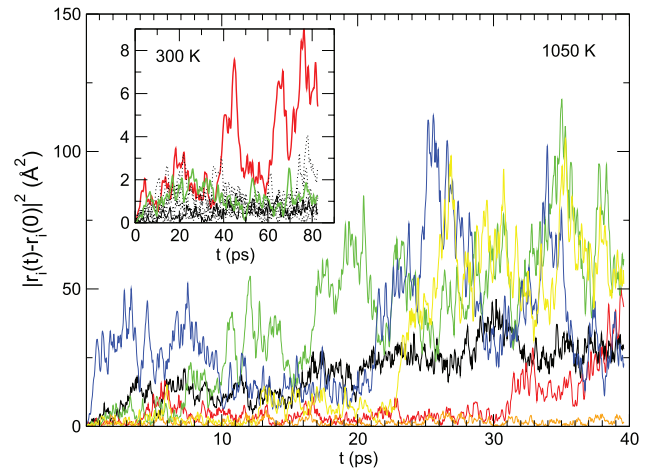


Figure 47. Time-resolved squared displacement of select individual Ge atoms in liquid (1050 K, [397]) and glassy (300 K, inset) GeSe_2 . It is seen that individual trajectories are made of long periods of vibrations and cage-like motions with a reduced spatial extent, but jumps can be noticed.

obvious origin for the non-exponentiality of the α -relaxation given that the KWW stretched exponential can be developed in a series of exponentials with different typical relaxation times, and might indicate that the relaxation is locally exponential, but with a spatial distribution that is complex and non-linear. There is, however, experimental and theoretical evidence [398] showing that even the local dynamics can be non-exponential as well, which increases the complexity.

On this issue, an insightful picture is again provided by MD simulations which show that while the mean-square displacement of a given species displays a smooth behavior with time (figure 42, left), and will, ultimately, provide some information about diffusion, there is evidence for species-dependent individual jumps that result, on average, in the spatial distribution of the van Hove function. These salient features depicted in figure 47 are found for a variety of simple supercooled liquids [402, 403], and not only reveal that such events are intermittent with waiting times between successive jumps statistically distributed, but also that they strongly differ from one particle to another.

7.2.2. Four-point correlation functions. An inspection of the single events depicted in figure 47 that lead to distributions in jump distances encoded in the function $\mathcal{G}_s(r, t)$ (figure 43) indicates that such spatio-temporal fluctuations cannot be described from ensemble-averaged measurements or calculations given that correlations between space and time fluctuations need to be considered. This also tells us such inhomogeneous dynamics, driven by mobile particles, need a generalization of mobility correlation functions, and current development has led to the definition of four-point correlation functions [404, 405] that focus on the statistical analysis of space and time deviations from the average behavior (for technical details see, for example, [402, 406]). There are also alternative approaches [401, 407, 408], some of which focus on the quantity:

$$Q(t) = \sum_{i=1}^N \sum_{j=1}^N w(|\mathbf{r}_i(0) - \mathbf{r}_j(t)|) \quad (66)$$

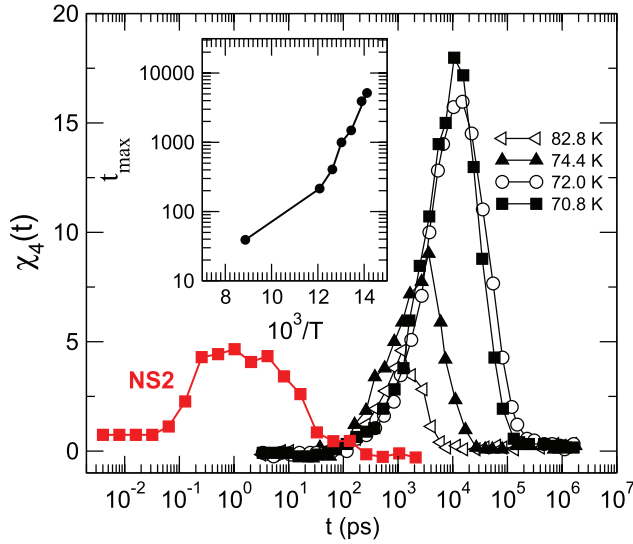


Figure 48. Time dependence and temperature of $\chi_4(t)$ in a densified liquid 2 SiO₂–Na₂O (2000 K, red symbols), and in a Lennard-Jones (LJ) liquid (adapted from [401]). Temperatures have been rescaled in order to correspond to LJ argon [412]. As the temperature decreases, the position t_{\max} of the peak in $\chi_4(t)$ monotonically increases, and shifts to longer times. This reveals an Arrhenius-like behavior (inset).

which is a measure of the degree to which a configuration at time t still overlaps the initial arrangement, the degree of overlapping being established from a window function $w(\mathbf{r})$ (where $w(\mathbf{r}) = 1$ if $|\mathbf{r}| \leq a$ and zero, otherwise with a a typical length scale).

In the simplest approach, one can define a mobility field $f_i(t)$ of the form:

$$f(\mathbf{r}, t) = \sum_i f_i(t) \delta(\mathbf{r} - \mathbf{r}_i) \quad (67)$$

and its fluctuating part is written as $\delta f(\mathbf{r}, t) = f(\mathbf{r}, t) - \langle f(\mathbf{r}, t) \rangle$. This allows the definition of correlations over the fluctuations in both real and reciprocal space:

$$g_4(\mathbf{r}, t) = \langle \delta f(\mathbf{0}, t) \delta f(\mathbf{r}, t) \rangle, \quad (68)$$

$$S_4(\mathbf{k}, t) = \langle \delta f(\mathbf{k}, t) \delta f(-\mathbf{k}, t) \rangle \quad (69)$$

$g_4(\mathbf{r}, t)$ depends only on the time t and the distance \mathbf{r} , and is termed ‘four-point’ because it measures correlations of motion arising at two points, 0 and \mathbf{r} , between 0 and t , and also connects to the variance of the mobility field. A dynamic susceptibility can be introduced from equation (68):

$$\chi_4(t) = \rho \int d^3r g_4(\mathbf{r}, t) \quad (70)$$

The function $\chi_4(t)$ represents the volume on which structural relaxation processes are correlated, and has been computed for a certain number of soft-sphere glass-forming liquids [409, 410] and silica [411]. Note, that an alternative definition of $\chi_4(t)$ can be used from the overlapping function used in equation (66) [401]:

$$\chi_4(t) = \frac{V}{Nk_B T} [\langle Q^2(t) \rangle - \langle Q(t) \rangle^2]. \quad (71)$$

The behavior of $\chi_4(t)$ with time appears to have some generic behavior because for each temperature $\chi_4(t)$ displays a maximum at a peak position that corresponds to the relaxation time [411] of the system. As the temperature is decreased, the intensity of $\chi_4(t)$ increases (figure 48) which signals the growing typical length scale involved in dynamic heterogeneities (space and time fluctuations), whereas the shift of the peak position to longer times reveals the increase of the relaxation time [411].

Given that the growth of the intensity of $\chi_4(t_{\max})$ indicates dynamics becoming increasingly spatially heterogeneous, with decreasing temperature a corresponding dynamic length-scale ξ_4 can be accessed from the low wavevector region of $S_4(k, t)$ (equation (69)) which shows an increase in intensity in the limit $k \rightarrow 0$ [401, 409, 413, 414] but, in the absence of large systems [415, 416], this limit is hardly attainable so that ξ_4 might be accessed from the numerical/experimental data using a low- k functional form inspired from the analysis of static and dynamic density fluctuations in the Ornstein–Zernike theory of liquid-gas transition [417]:

$$S_4(k, t) \simeq \frac{S_0}{1 + k^2 \xi_4^2} \quad (72)$$

In supercooled silica, an analysis using the framework of four-point correlation functions in different ensembles [409, 411] shows that ξ_4 is an increasing function of the relaxation time. Furthermore, there is a strong indication [418] that these multi-point dynamic susceptibilities can be accessed experimentally since temperature and density variations of averaged correlations of a mobility field $f(t)$ contribute to $\chi_4(t)$:

$$\chi_4(t) = \chi_4^{\text{NVE}}(t) + \frac{k_B}{c_v} T^2 \left[\frac{\partial \langle f(t) \rangle}{\partial T} \right]^2 + \rho^3 k_B T \kappa_T \left[\frac{\partial \langle f(t) \rangle}{\partial \rho} \right]^2 \quad (73)$$

$$= \chi_4^{\text{NVE}}(t) + \frac{k_B}{c_v} T^2 \chi_T^2(t) + \rho^3 k_B T \kappa_T \chi_\rho^2 \quad (74)$$

where the susceptibilities χ_T and χ_ρ arise from the fluctuations induced by energy and density, respectively. At fixed density and low temperature $\chi_4^{\text{NVE}}(t)$ is much smaller, and $\chi_4(t)$ is dominated by the contribution due to χ_T (figure 49) that can be measured from the temperature variation of system-averaged correlations $\langle f(t) \rangle$. Other MD simulations on liquid silica have revealed [403] that the structural relaxation dynamics are spatially heterogeneous, but cannot be understood as a statistical bond-breaking process which is thought to be the dominant process for viscous flow [398]. In addition, the high particle mobility seems to propagate continuously through the melt. Furthermore, it has been demonstrated that, on intermediate timescales, a small fraction of oxygen and silicon atoms deviate from a Gaussian behavior and are more mobile than expected from (equation (63)). These highly mobile particles form transient clusters larger than those resulting from random statistics, indicating also that the dynamics are spatially heterogeneous [382]. From a Monte Carlo study of silica [419] the emergence of heterogeneous dynamics is also suggested, and thought to be connected to a decoupling between

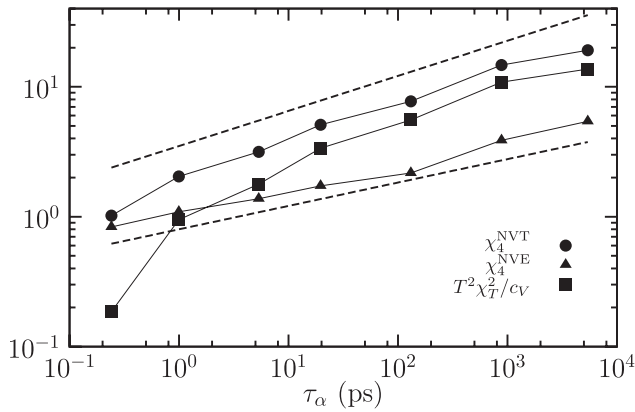


Figure 49. Time dependence of $\chi_4(t)$ in van Beest, Kramer, and van Santen (BKS) silica [411]. At low temperature (large relaxation time), one has $\chi_4^{\text{NVE}} \simeq T^2 \chi_4^2 / c_V$ (see equation (73)). Permission from AIP Publishing LLC 2015.

translational diffusion and structural relaxation (see below), and to a growing four-point dynamic susceptibility. However, dynamic heterogeneity appears to be less pronounced than in more fragile glass-forming models, albeit not of a qualitatively different nature [382].

7.2.3. Stokes–Einstein breakdown. The presence of intermittent dynamics with atoms having a different motion depending on time and space (figure 47), leads to the occurrence of a non-Gaussian diffusion that can be detected when $F_s(k, t)$ and the first term of the expansion of (equation (65)), $\exp[\langle r^2(t) \rangle] / 6Dt$ are directly compared. While both will nearly overlap at high temperature, there is a progressive deviation setting in as the system approaches T_g , and this indicates that the relaxation time (or the viscosity) derived from $F_s(k, t)$ decouples from diffusivity (given by $\langle r^2(t) \rangle$) and has a different behavior with temperature: a feature also known as the Stokes–Einstein breakdown, i.e. the product $\eta D / T$ ceases to be constant (equations (60) and/or (61)) and ceases to fulfill the dispersion relation $\tau = 1/q^2 D$. This decoupling of transport coefficients is usually tracked from the Stokes–Einstein ratio $R_{SE} \equiv D\eta / T$ or the Debye–Stokes–Einstein ratio $R_{DSE} \equiv \eta / \tau T$, and a separate calculation or measurement of both τ and D has acknowledged the decoupling at low temperature in several systems, from organic [420–422], hydrogen-bonded [423] to metallic liquids [424–426].

In structural glass-forming liquids (e.g. GeTe [427]), it has been found that a very high atomic mobility ($D \simeq 10^{-6} \text{ cm}^2 \cdot \text{s}^{-1}$) remains important down to $T \simeq T_g$, indicating the breakdown of the Stokes–Einstein relationship (figure 50) that connects with dynamic heterogeneities, as also suggested from crystallization measurements on a similar system (Ge–Sb–Te [428]). For this particular GeTe system, the high atomic mobility results from zones of fast and slow moving atoms, with the former containing a large fraction of homopolar (GeGe) defects [429].

In order to quantify the decoupling and temperature evolution of both R_{SE} and R_{DSE} , a fractional Stokes–Einstein relationship has been introduced [420–422], i.e. D now scales as

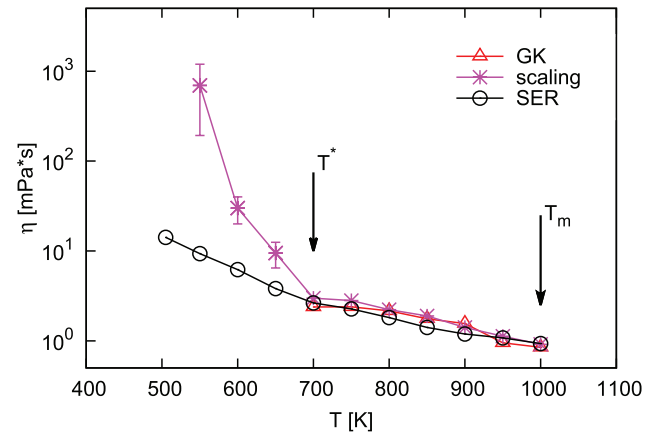


Figure 50. Decoupling between Green–Kubo (GK + scaling) and Stokes–Einstein (SER) calculated viscosities using the calculated diffusivities in liquid GeTe [427]. Permission from J Wiley and Sons 2015.

$\tau^{-\zeta}$ where ζ relates to the characteristic spatio-temporal length scales involved in the heterogeneous dynamics, and a typical value has been found to be about 0.82 – 0.85 for different glass formers [420, 430, 431]. Here, ζ has been proposed to derive from temperature-dependent scaling exponents of both diffusivity and relaxation time, respectively [432]. However, the validity of this fractional Stokes–Einstein relationship has been questioned from a separate investigation of a series of silicate liquids [433] which emphasizes the two fundamentally different mechanisms governing viscous flow and conductivity/diffusivity. Separate fits of resistivity and viscosity curves indeed lead to different temperature dependences that can be appropriately modeled by the AM (equation (6), [32]) and MYEGA (equation (7), [33]) functional forms, respectively, and which lead to a decoupling of diffusivity and viscosity at low temperature without invoking the need for a fractional Stokes–Einstein relation. Also, there is no general agreement on the temperature region over which decoupling of transport coefficients is supposed to onset. While building on the fractional Stokes–Einstein relationship, a systematic study of glass-forming liquids including B_2O_3 , SiO_2 , GeO_2 and soda-lime silicate glasses [430] indicates that the breakdown of the Stokes–Einstein relationship should occur at much higher temperatures, i.e. at viscosities of about $10^2 \text{ Pa} \cdot \text{s}$, a value that is 8–10 decades lower than the one found for T_g .

7.3. Energy landscapes

As already mentioned in different examples above [191–193], numerical simulations also allow one to study in detail the link between thermodynamics and glassy relaxation by using the framework of energy landscapes. This school of thought traces back to the seminal contribution of Goldstein [434] who identified what aspects of glassy dynamics connect to the relevant features of the topography of landscapes: saddles, minima, peaks, basins with an important emphasis on the description of potential energy barriers which contribute to the slowing down of the dynamics, and contribute, overall to a statistical

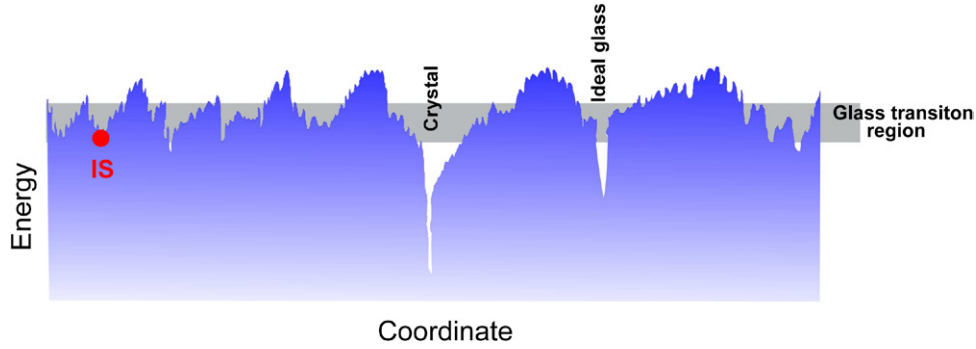


Figure 51. Potential energy landscape of a glass-forming liquid. Local energy minima (inherent structures, IS [435]) contribute to the global shape of the landscape which also contains a deep minimum corresponding to the crystalline polymorph, and a local minimum with the lowest energy corresponding to an ‘ideal’ glass. In the glass transition region, the landscape dominates the dynamics. The red dot signals a local minimum corresponding to an IS.

definition of activated dynamics that is encoded in the previously introduced activation energy E_A for viscosity or diffusion. This has led to the definition of the energy landscape picture in which a high temperature liquid is able to sample the entire phase space and, correspondingly, the energy landscape, because the thermal energies will be of the same order as the heights of the potential energy barriers. As the temperature is lowered, the potential energy landscape will affect the dynamics and thermal energy fluctuations will still allow the liquid to make transitions over energy barriers from one local minimum to another, i.e. activated dynamics. There is a clear separation of the timescales for vibration within one minimum and for transitions from one minimum to another. Once quenched to a glass, the system will be stuck in some local minimum, given that the barrier heights are now much larger than the amplitude of thermal fluctuations, the rearrangement of atomic positions essentially takes place in small regions of the landscape.

7.3.1. Inherent structures. MD simulations appear to be very helpful in order to conveniently characterize the multidimensional potential energy hypersurface created by a large number of interacting atoms or molecules. The notion of ‘inherent structure’ (IS) has been introduced [30, 435–437], and this notion permits one to uniquely separate the complex landscape topography into individual ‘basins’, each containing a local potential energy minimum or IS (figure 51). The search of ISs is usually performed by starting at an original point in configuration space (atomic positions), and performing a steepest descent minimization of the potential energy function by changing atomic coordinates locally until a local minimum (the IS) is found. Such a procedure can be repeated and used to characterize the entire configuration space by separating landscape into regions called basins; all points in a basin having the same IS. There are various ways to numerically detect such IS and to classify their characteristics, depth or curvature. Additionally, shared basin boundaries are defined by saddles or transition states which allow movement from one basin to another one and a variety of techniques have been developed in recent years, such as activation-relaxation [438, 439], steepest descents [28], basin-hopping global optimization [440] or other graph-connected approaches [441–443], some of them applying only to clusters.

7.3.2. Light formalism. In the case of glassy relaxation, the starting point is a system of N particles interacting via a potential $V(\mathbf{r})$. Following the Stillinger–Weber formalism (see, for example, [29, 444]), one usually decomposes the position-related contribution $Q(T, V)$ of the partition function:

$$Z(T, V) = \frac{1}{N! \lambda^{3N}} Q(V, T) = \frac{1}{N! \lambda^{3N}} \int_V e^{V(\mathbf{r}^N)/k_B T} d\mathbf{r}^N \quad (75)$$

into contributions arising from the local minima with an inherent structure energy e_{IS} :

$$Q(T, V) = \sum_i e^{-e_{IS_i}/k_B T} \int_{\text{basin } i} e^{-\Delta V(\mathbf{r}^N)/k_B T} d\mathbf{r}^N \quad (76)$$

where $\Delta V(\mathbf{r}^N) \equiv V(\mathbf{r}^N) - e_{IS}$ is the value of the energy in the local minimum (IS), and the sum excludes basins which have some crystalline order. By averaging over all distinct basins with the same energy e_{IS} , and counting the number of basins of energy e_{IS} :

$$\Omega(e_{IS}) = \sum_i \delta_{e_{IS}, e_{IS_i}} \quad (77)$$

one can write a partition function that is averaged over all distinct basins with the same energy e_{IS} :

$$Q(e_{IS}, T, V) = \frac{\sum_i \delta_{e_{IS}, e_{IS_i}} e^{-e_{IS_i}/k_B T} \int_{\text{basin } i} e^{-\Delta V(\mathbf{r}^N)/k_B T} d\mathbf{r}^N}{\sum_i \delta_{e_{IS}, e_{IS_i}}} \quad (78)$$

which leads to a basin-related partition function and free energy:

$$\begin{aligned} Z(T, V) &= \sum_{e_{IS}} \Omega(e_{IS}) e^{-f_{\text{basin}}(e_{IS}, T, V)/k_B T} \\ &= \sum_{e_{IS}} e^{-[-TS_{\text{conf}}(e_{IS}) + f_{\text{basin}}(e_{IS}, T, V)]/k_B T} \end{aligned} \quad (79)$$

$$f_{\text{basin}}(e_{IS}, T, V) \equiv -k_B T \ln \left[\frac{Q(e_{IS}, T, V)}{\lambda^{3N}} \right] \quad (80)$$

which leads to the definition of the configurational entropy $S_{\text{conf}}(e_{IS})$:

$$S_{\text{conf}}(e_{IS}) \equiv k_B \ln \Omega(e_{IS}) \quad (81)$$

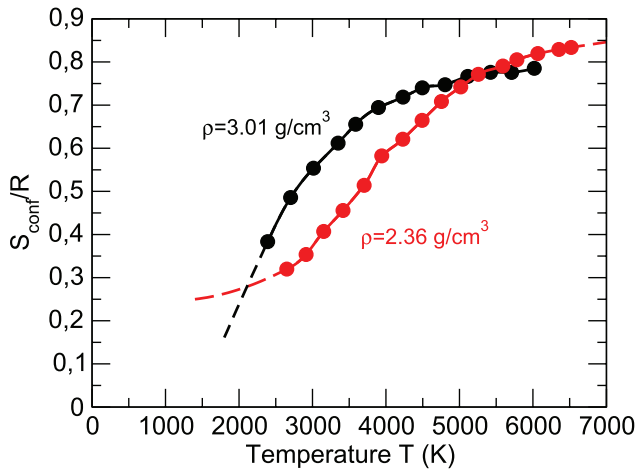


Figure 52. Temperature dependence of S_{conf} of supercooled silica at different densities (adapted from [193]). Dashed lines represent possible extrapolations, and may indicate the possibility of an entropy crisis only for selected densities.

so that the free energy can be reduced to the free energy of the typical basins and the number of such basins with a given IS energy explored at a temperature T .

In practice, and as mentioned before, IS configurations at temperature T are explored and enumerated by, for example, a steepest descent minimization [200, 445]. In addition, the full calculation of the configurational entropy and free energy needs an explicit account of the vibrational (curvature) contributions to each minimum, and a contribution from anharmonic effects that are determined by difference [444] from the calculated total free energy $F(T, V)$ of the system (derived from equation (75)) which is evaluated by thermodynamic integration [29].

73.3. Main results. A certain number of studies have focused on the link between the energy landscape characteristics, the inherent structures and the glassy relaxation of a supercooled liquid. Ultimately, connections with the dynamics can be made and these reveal, for example, that the diffusivity obeys [191] an Adam-Gibbs-like relationship (figure 19, left).

In supercooled silica, potential energy landscapes have been investigated [193, 446–448], and have revealed that the distribution of IS energies significantly deviates from a Gaussian distribution [193], a result that seems to be connected with the progressive formation of a defect-free tetrahedral network which acts as a ground state for the system [448]. As a result, the configurational entropy S_{conf} does not appear to extrapolate to zero at finite temperature [193, 449], and this suggests the absence of a finite Kauzmann temperature (figure 52) at select conditions. Another key result is that for small systems the typical timescale involved in the pseudo-periodic motion between two adjacent inherent structures can be very long [450] and, for certain systems, about eight times the average relaxation time [451]. However, this type of local dynamics does not contribute to the structural relaxation of the supercooled liquid, but at low temperature there are techniques [438] which activate the dynamics in order to escape from such large basins connecting two ISs with a low energy barrier. Using such an IS analysis, the viscosity can be

decomposed [452] into a structural contribution that is associated with energy minima, and a vibrational contribution, the former leading to strain-activated relaxation, while the latter is purely Newtonian, and this also has implications for the fragility behavior [453].

Given that chalcogenides are usually studied from *ab initio* simulations that lead to system sizes that are considerably smaller (see, however, [397]), potential energy landscape approaches have not been considered and applied to these materials so far. Furthermore, such relatively small systems would be relevant for understanding supercooled liquids only at high temperature given that correlated motions of particles grow as the temperature is lowered in the landscape-influenced regime [454]. Studies on transitions in small systems have indeed shown that a system with a small number of atoms can be trapped in metabasins with a wide variety of energies and lifetimes at temperatures in the landscape-influenced region [455, 456], and because hops between such metabasins are correlated, only a limited number of particles will introduce a bias in the dynamics.

8. Aging

Although relaxation times of glasses exceed common observation timescales, physical properties still continue to evolve with time at temperatures below T_g . An increase in the observation time will, therefore, permit one to detect the equilibration of the system at lower temperatures. Much below T_g however, such equilibrium relaxation times become so huge that they are clearly out of reach, e.g. one has an increase to relaxation times of the order of 10^{14} s, given that $\tau(T/T_g)/\tau(1) = \exp[E_A/T]$, and assuming an Arrhenius activation energy of about 1 eV, and a glass transition temperature $T_g \simeq 500$ K, both values being typical of network glasses. In aging experiments, one therefore focuses on temperature intervals which are close to T_g , i.e. $T/T_g \simeq 0.8$. For such temperatures, physical aging can be followed over months and years, as detailed below.

The experimental protocol for an aging experiment is well established. An equilibrated supercooled liquid is abruptly quenched to a temperature $T_w \leq T_g$ at a waiting time $t = t_w = 0$ which corresponds to the beginning of the experiments. Physical properties are then recorded as a function of time but, because of the non-equilibrium nature of the system, such properties will also depend in a non-trivial fashion on the waiting (aging) time t_w before the measurements are performed. In fact, while left unperturbed, the glass will continue to relax and will attempt to reach thermal equilibrium, and the way it relaxes depends on the temperature T_w at which the aging experiment is performed. As a result, the measurement will not only depend on the time t_w , but also on T_w .

8.1. Time correlators

Mean-field glass models [457, 458] originally designed for spin glasses [459] have been introduced in the context of aging, and have emphasized the central role played by broken ergodicity. In such approaches, thermal equilibrium cannot be reached,

and aging results from the downhill motion of an energy landscape that becomes increasingly flat. One major result of such approaches is that the time-translational invariance typical of ergodic systems is broken so that time correlators for any observable must be defined in the aging regime, and these now depend explicitly on both times t and t_w , as do the response functions of the system. Mathematically, such complex time evolutions can be cast into two-time-dependent functions, namely (i) a two-time correlation function defined by:

$$C(t, t_w) = \langle A(t)A(t_w) \rangle - \langle A(t) \rangle \langle A(t_w) \rangle, \quad (82)$$

with $t \leq t_w$, and where $A(t)$ is a typical observable (e.g. the intermediate scattering function $F_s(k, t)$), and (ii) the response function $G(t, t_w)$ given by:

$$G(t, t_w) = \left(\frac{\delta \langle A(t) \rangle}{\delta h(t_w)} \right)_{h=0} \quad (83)$$

where $h(t_w)$ is a conjugate field to the observable A , and the brackets indicate averages over the thermal history. For instance, if $A(t)$ is the average 1D position of the particles $A(t) = 1/N \sum_i \langle x_i(t) \rangle$, then the response function is computed from the perturbed Hamiltonian $H = H_0 - h \sum_i x_i$. In systems in equilibrium, both two-time functions are related via the fluctuation-dissipation theorem [460] which quantifies the relation between the fluctuations in a equilibrated liquid and the response to applied perturbations. This leads to:

$$TG(t, t_w) = - \frac{\partial C(t, t_w)}{\partial t} \quad (84)$$

or, using the integrated response:

$$\Delta C(t, t_w) = C(t, t) - C(t, t_w) = T \int_{t_w}^t G(t, t') dt' \quad (85)$$

One important property of equation (84) and of the two functions $G(t, t_w)$ and $C(t, t_w)$ is their time translation invariance at equilibrium, i.e. all depend only on $t - t_w$. Once the system becomes out of equilibrium at $T < T_g$, a major consequence is that the fluctuation-dissipation theorem does not hold, this behavior being fulfilled in glasses displaying aging behavior for which the response functions and the FDT become waiting time-dependent (i.e. on t_w), and stop being invariant under $t - t_w$. Here, it is convenient to rewrite the FDT of equation (84) using an effective temperature T_{eff} that also leads to the introduction of a fluctuation-dissipation ratio (FDR) $X(t, t_w)$:

$$T = T_{\text{eff}} X(t, t_w) \quad (86)$$

and, by definition, one has at equilibrium $X(t, t_w) = 1$ and $T_{\text{eff}} = T$. From a fundamental viewpoint, the introduction of an effective temperature has a profound implication for the meaning and the measurement of temperature in a system undergoing aging. In fact, since the temperature is related to the timescale (equilibration) and to particle velocities (equilibration), its measurement in a glassy state for which both relaxation times and velocities are time and spatially-dependent (heterogeneous dynamics), poses a true challenge [461] with the difficulty being to define an appropriate thermometer. For certain simple models, additional degrees of freedom

representing the thermometer can be coupled in a simple fashion to an observable of interest, and this allows one to relate the measured temperature to the correlation function and the integrated response [462]. While this definition of T_{eff} has been found to be rather appropriate in a certain number of systems or models [463, 464] investigated within the energy landscape formalism [465], its robustness has also been questioned [466, 467]. We refer the reader to reviews that specifically focus on this topic [468, 469].

8.2. Insight from trap models

A simple way to understand the physics of aging is directly derived from the Goldstein picture of energy landscapes, and uses trap models [456, 471–473] in which particles can move from one local minimum of the complex landscape to another. Here, these local minima are seen as metastable configurations with high energy barriers so that such minima can act as traps and hold the glassy system during a certain finite time.

The central question of this approach is to ask what could be the distribution of such trapping times, and a simple answer can be given assuming that there exists a ‘percolation’ energy level E_0 below which the minima are disconnected. For $E > E_0$, it is possible to hop between any two states given that the energy barrier is equal to $\Delta E = E_0 - E$, and the system can relax to lower energies.

An interesting outcome is the existence of a cross-over between two aging regimes illustrated by, for example, a magnetization function $m(t)$ of a spin system [472] that is exponential:

$$m(t) = m_0 e^{-\frac{\gamma}{1-x} (t/t_w)^{1-x}}, \quad (87)$$

and is a power-law $m(t) = (t/t_w)^{-\gamma}$ for $t \ll t_w$ and $t \gg t_w$, respectively. Here, x characterizes the distribution of free energies in the glassy phase [471], and γ is related to the probability of relaxation when leaving a trap. In the short time domain, these models reproduce the stretched exponential decay typical of α -relaxation, and are also found to depend on t/t_w only. On a more general ground, such non-equilibrium statistical mechanics models capture some of the salient features of the dynamics of aging. Here, the phase space is seen as a large collection of metastable states which induce a broad distribution of lifetimes. When the average lifetime of these metastable states diverges, all the physical observables are dominated by the properties of the deepest state.

A certain number of models with different distributions of trap depths (Boltzmann [474], Gaussian [471]) lead to the usual features of glassy relaxation, i.e. a power-law for simple dynamic variables [475], a super-Arrhenius behavior for the relaxation with a diverging temperature [456] or a stretched exponential decay.

8.3. Molecular dynamics simulations

Computer simulations can directly probe the enunciated breakdown of the fluctuation-dissipation ratio (equation (84)), and a separate computation of the integrated response

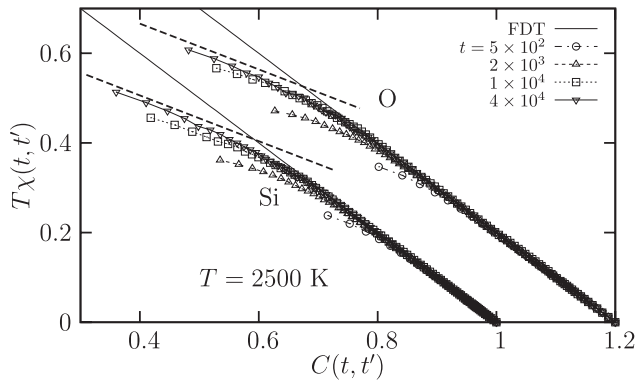


Figure 53. Response versus correlation calculated in the aging regime of a silica glass [470]. At short times, the plots converge to the straight line of slope 1, whereas at large times (small values of $C(t, t')$) a slope $X \simeq 0.51$ is found, yielding an effective temperature of $\simeq 4900$ K. Permission from the American Physical Society.

and the correlation function leads to a straight line with slope $-1/T$ (equation (85), figure 53) in an equilibrated liquid [463, 470, 476], and $-1/T_{\text{eff}}$ in a system subject to aging, the latter situation occurring for small values of the correlation functions. A break in the slope permits the detection of aging regimes, and provides an approximate limit of equilibration. Such simulations also allow one to verify the behavior predicted from trap models [477] or to connect this to dynamic heterogeneities, and for a selected number of strong and fragile glass-forming systems (including silica) the calculated 4-point density susceptibility $\chi_4(t, t_w)$ and the dynamic correlation length $\xi_4(t, t_w)$ have the same behaviors, qualitatively, as a function of t_w and $t - t_w$ [478]. Additionally, the tails of the displacement distributions show a qualitatively different evolution with t_w in the case of more fragile liquids, and this evolution appears to be associated with the particles which have diffused the most.

The local aging dynamics can also be characterized, and this eventually connects back to dynamic heterogeneities for model structural glasses [479]. In silica, aging seems to result from single particle trajectories and jump events corresponding to the escape of an atom from the cage formed by its neighbors [480]. It has been found that the only t_w -dependent microscopic quantity is the number of jumping particles per unit time [481], and this quantity has been found to decrease with age. The second key finding is that for such strong glass-forming systems, but also in more fragile ones [482, 483], neither the distribution of jump lengths that relates to the self part of the van Hove correlation functions (equation (62)) nor the distribution of times spent in the cage are t_w dependent. Except silica, we are not aware of any other MD study on aging in network-forming glasses.

8.4. Applications

8.4.1. Oxides. Aging effects in oxides, and particularly silicates, were first reported in the seminal work of Joule [484, 485] on silicate glass thermometers, and then studied in detail by Nemilov [486, 487]. Nemilov and Johari [488] investigated changes in various physico-chemical properties for aging times ranging from hours to decades. From these

studies, it has been stated that the completeness of aging of glass at any age is determined by its aging rate after about one year [487], and nearly forty glasses have been classified with respect to this criterion. For the special case of silicates, one should keep in mind that glass transition temperatures in such systems are quite high so that aging experiments performed at ambient conditions only show small variations given the important difference with T_g . However, this seems to be contradicted by the observed changes in, for example, density over time [488] which have been found to have characteristic relaxation times much shorter than those of an α -relaxation process. On this basis, it has been proposed that the structural changes occur on timescales typical of a β -relaxation which is typical of cage-like dynamics (figure 14). Densification is then seen as the result of angular changes between $\text{SiO}_4/2$ tetrahedra which induce local strained regions in the glass, and a subsequent dissipation of this strain energy, the former process being much slower and determining the kinetics of aging. The link with structural features driving the effect of aging have also been detected on phosphate [489] or silica-based glasses [490] from spectroscopic studies.

The use of x-ray photon correlation spectroscopy appears to be an interesting probe for the investigation of structural relaxation processes, and by using different thermal histories (cooling rates), one can observe a complex hierarchy of dynamic processes that are characterized by distinct aging regimes. These features are seen in metallic glasses [149, 150] and also in silicates [153], and one can find strong analogies with the aging dynamics of softer glassy materials [491], while also pointing to stress relaxation as a universal mechanism driving the relaxation dynamics of out-of-equilibrium systems. This has also been acknowledged for a borosilicate glass which shows stress relaxation under aging at $T/T_g \simeq 0.3$ [105], but contradicts the qualitative mechanism sketched from density changes with aging [488].

8.4.2. Chalcogenides. Because of their relatively low glass transition temperature, allowing for aging experiments at ambient temperature, there is quite an important body of literature on the effect of aging on various thermal, mechanical, and dielectric properties in polymers [492–496] that has inspired work on chalcogenide network glass-forming liquids such as As–Se or Ge–Se [497, 498], mostly accessed experimentally, and from techniques such as DSC or mDSC. Readers interested in this topic and its promising applications should refer to an excellent review article [498] which also contains more specific aspects of aging such as thermally- or irradiation-induced effects.

There is a crucial dependence of the temperature at which aging is performed, T_w , on the maximum enthalpy ΔH_∞ that can be released upon heating an infinite aged sample, and Saiter [493] has proposed that it scales as:

$$\Delta H_\infty = \Delta C_p(T_g)(T_g(q) - T_w) \quad (88)$$

where T_g is the glass transition determined by the scan with a fixed heating rate, and ΔC_p is the jump in specific heat at T_g . From equation (88), it becomes clear that the measurement of aging will strongly depend on T_w , and eventually

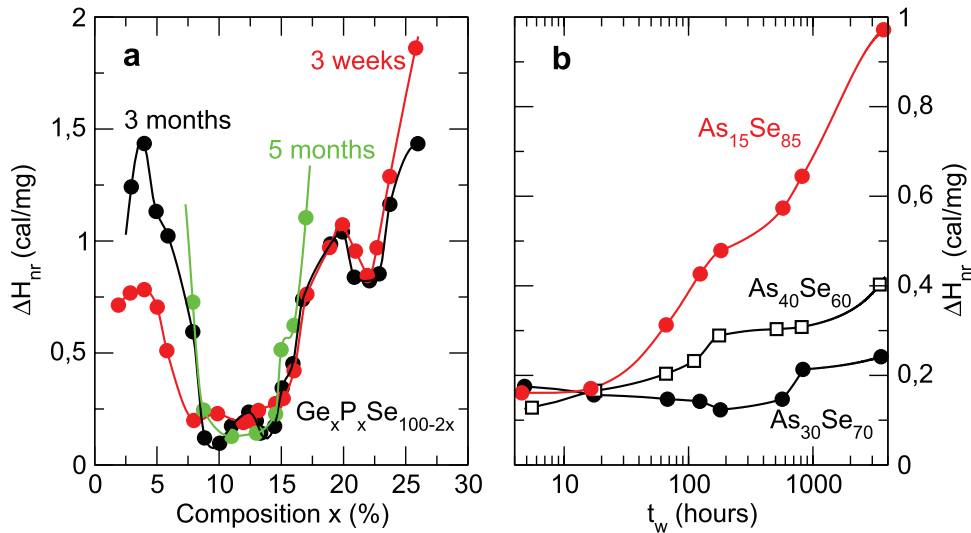


Figure 54. Aging effect on the non-reversing heat enthalpy ΔH_{nr} in chalcogenide networks as a function of aging. (a) Ge–P–Se glasses (adapted from [244]). (b) As–Se glasses (adapted from [507]). For window compositions ($As_{30}Se_{70}$), the evolution with waiting time is substantially reduced.

cancel in case of rejuvenation when $T_w \simeq T_g$. Given this relationship (equation (88)), long-time physical aging has been investigated in these chalcogenide networks [499–501]. Also, since the enthalpic loss is directly related to $T_g - T_w$, aging is enhanced for compositions which have a lower T_g (i.e. usually chalcogen-rich [43]) so that the enthalpic relaxation can be measured within a short period, and seems to follow a sigmoidal time dependence [12].

There are aspects of structure that have been characterized in connection with this topic, in particular from Raman spectroscopy [499, 502], NMR [503], and all indicate the weak changes in short-range order under aging, also characterized from x-ray absorption [503], a conclusion that is consistent with a large dynamic correlation length [401]. When two types of glasses are compared (20 years aged and rejuvenated), Raman spectroscopy of As–Se [499] seems to indicate small changes in bond statistics (as for NMR), and for Se-rich glasses, it has been concluded that Se ring-like structure collapse leads to a reorganization of chain fragments between $AsSe_{3/2}$ units. Overall, these different probes signal that As–Se–Se–As motifs convert into As–Se–As and As–Se–Se–Se–As fragments during aging. This chain-switching mechanism is actually supported from *ab initio* simulations of elemental Se [504] which shows fast (≈ 100 fs) changes in chain structure involving defect coordinations ($r_{Se} = 1$ or 3) that give support to proposed valence-alternation pairs for light-induced structural changes [505, 506].

8.4.3. aging in isostatic glasses. Isostatic network glasses are found to display a significantly reduced tendency towards aging and this has been detected for a certain number of systems. Experiments on Ge–P–Se network glasses across the isostatic phase [244] show that the deep and wide reversibility window in these chalcogenides sharpens and gets deeper as glass compositions outside the window age at 300 K over different periods (figure 54(a)).

It is to be noted that the experimental protocol does not follow the one usually designed for aging studies in, for example, spin glasses for which the system is maintained at a fixed T/T_g [472]. Here, given that T_g is a function of glass composition, the effective aging temperature T_w/T_g itself will also vary with composition. Floppy glasses which are below the IP window age significantly over a 3 month waiting period (figure 54(b)), while stressed-rigid glasses (above the window) age somewhat slower, over ≈ 5 months, an observation that directly results from the slower aging kinetics connected with higher glass transition temperatures. In such IP glasses, there is weak evidence of aging, even after a 5 month waiting period. Similar results have been found for As–Se glasses [507] with a weak evolution of the non-reversing enthalpy for reversible glasses, and contradictory results on this topic [327] have been further analyzed [329] and could be interpreted as a result of nanoscale phase separation resulting from light exposure. Furthermore, it has been pointed out that a proper aging procedure (i.e. at fixed T_w/T_g for all compositions) may not lead to the anomalous behavior observed in figure 54(b), and measurements on Ge–Se glasses using DSC could not reproduce the generic behavior proposed for isostatic glasses [508].

Finally, it must be emphasized that sophisticated experimental procedures, multiple cycles of cooling, heating and waiting times, modulation of the applied external fields, can lead to spectacular effects of aging in glassy materials, such as rejuvenation and memory [498].

9. Conclusions and perspectives

At this stage, rather than summarizing the different topics covered in this article, we would like to emphasize that specific features typical of relaxation in supercooled liquids which could benefit from the low temperature description of the corresponding glassy materials. This is particularly relevant in the case of network glasses. There have been recent efforts to bridge the gap between theoretical approaches and

experimental methods used or derived from the liquid side and the glassy side of the glass transition [509]. Progress has been slow, but more and more methods are being applied to this purpose, and this might be particularly crucial as one considers network glass-forming liquids.

Here, we have reviewed the ongoing effort and studies that have been reported in the literature in order to characterize and understand the physics of the glass transition and related aging phenomena once a system is maintained at $T < T_g$. We have focused on the special case of network-forming glasses, i.e. on materials which are dominated by their low temperature underlying structure. These glasses are often thought to systematically have low fragilities and to belong to the category of strong glass formers, albeit this is contradicted by various experimental measurements [15, 41]. Most of the recent simulation work on inorganic supercooled liquids, and especially the one focusing on dynamic heterogeneities [403, 411] is restricted to liquid silica which has a fragility index of $\mathcal{M} = 20$. Investigation of other typical network formers (B_2O_3 , $GeSe_2$, ...) are welcome. While similar features with fragile liquids have been emphasized [382], there is probably much to learn from an investigation of network glasses because an appropriate alloying allows one to tune physical properties (e.g. structure) in a continuous fashion, that can, in turn, be connected or correlated to dynamic properties such as fragility. Studies of the compositional dependences and the detection of anomalies in dynamic or relaxation properties are, therefore, believed to represent an interesting and additional means to learn more on the glass transition phenomenon.

In this respect, recent efforts [35] attempting to derive approaches that use rigidity theory in a substantially revised version, represent attractive pathways for an improved quantitative description of glassy dynamics. Here, it is assumed that relaxation is controlled by aspects of structure, topology and/or rigidity, or, more generally, by features of the low temperature glass. This fact has been acknowledged by various authors (e.g. [81]), although methods and models are often based on equilibrium statistical mechanics that bear obvious limitations once they are applied to the glassy state. A promising way to combine both approaches, from the glass to the liquid state is provided by molecular dynamics-based constraint counting [305] which permits one to calculate various properties from ensemble averages, and to connect to rigidity theory via an explicit account of the topological constraints. From a more applied viewpoint, given the general use of such simulations in the description of glassy materials, this recent extension now offers the possibility to rationalize the design of new families of other materials using as input the rigidity state of the underlying atomic network, as recently demonstrated [311], and the corresponding glassy dynamics can be investigated.

This link between network rigidity and the thermodynamics and relaxation of supercooled liquids seems to have an even more general ground as recently emphasized [220], and these ideas can actually also be extended to other glass-forming liquids including fragile ones [81]. Indeed, glass elasticity and the presence of soft elastic modes have been found to drive many aspects of glassy relaxation as mentioned

throughout this review, and also to relate to thermodynamic changes across the glass transition. In fact, an abundance of such soft modes permits exploration of the phase space without large changes in energy [271], and this ultimately leads to small changes in the specific heat. This, of course, connects back to the notion of floppy modes [61] that are present in weakly connected (flexible) network glasses.

Finally, it would be interesting to consider, in a combined fashion, aspects from the statistical mechanics of non-equilibrium systems [469], molecular simulations and rigidity theory to investigate the aging of chalcogenide glasses. This would allow the description of these phenomena beyond the qualitative level (figure 54). Given the number of important applications of chalcogenides in optoelectronics [2, 498], the understanding and, eventually, the control of aging phenomena could improve the stability of devices using chalcogenides as base material, as recently stressed in a study on optical phase change recording [510]. Still, a certain number of challenges remain that are inherent to some of the methods employed: small system sizes due to *ab initio* simulations in order to treat correctly the covalent or semi-metallic bonding, and the short timescale of the MD simulations. Despite these limitations, such methods exhibit a certain number of promising results on this topic for the archetypal SiO_2 [470], and might well be applied in a similar fashion to its parent chalcogenide system with a wealth of possible applications, directly derived from the very basic features of non-equilibrium statistical mechanics.

Acknowledgments

Support from Agence Nationale de la Recherche (ANR) (Grant No. 09-BLAN-0109-01 and Grant No. 11-BS08-0012) is gratefully acknowledged. MM acknowledges support from the French-American Fulbright Commission, and from International Materials Institute (H Jain). GENCI (Grand Equipement National de Calcul Intensif) is acknowledged for supercomputing access. The authors thank M Bauchy, C Massobrio, M Wyart, S Le Roux, M Boero, C Bichara, P Boolchand, N Sator, A Pradel, B Guillot, J C Mauro, M Smedskjaer, S Boshle, K Gunasekera, J Du, M Malki, G G Naumis, P S Salmon, A Pasquarello, Y Yue, J-Y Raty, M Salanne, G Ferlat, J C Phillips, P Simon, D De Sousa-Meneses, A Piarristeguy, R Vuilleumier, S Ravindren, N Mousseau, S Chakraborty for stimulating discussions.

References

- [1] Zanutto E D 1998 *Am. J. Phys.* **66** 392
- [2] Piarristeguy A, Cuello G, Fernandez-Martinez A, Cristiglio V, Johnson M, Ribes M and Pradel A 2012 *Phys. Status Solidi B* **249** 2028
- [3] Zachariasen W H 1932 *J. Am. Chem. Soc.* **54** 3841
- [4] O'Hern C S, Silbert L E, Liu A J and Nagel S R 2003 *Phys. Rev. E* **68** 011306
- [5] Angell C A, Poole P H and Shao J 1994 *Nuovo Cimento D* **16** 993
- [6] Stolen S, Grande T and Johnsen H B 2002 *Phys. Chem. Chem. Phys.* **4** 3396

- [7] Neuville D R 2006 *Chem. Geol.* **229** 28
- [8] Tatsumisago M, Halfpap B L, Green J L, Lindsay S M and Angell C A 1990 *Phys. Rev. Lett.* **64** 1549
- [9] Laughlin W T and Uhlmann D R 1972 *J. Phys. Chem.* **76** 2317
- [10] Angell C A 1995 *Science* **67** 1924
- [11] Ito K, Moynihan C T and Angell C A 1998 *Nature* **398** 492
- [12] Angell C A, Ngai K L, McKenna G B, McMillan P F and Martin S W 2000 *Appl. Phys. Rev.* **88** 3113
- [13] Huang D and McKenna G B 2001 *J. Chem. Phys.* **114** 5621
- [14] Simon S L, Plazek D J, Sobieski J W and McGregor E T 1997 *J. Polym. Sci. B* **35** 929
- [15] Gunasekera K, Bhosle S, Boolchand P and Micoulaut M 2013 *J. Chem. Phys.* **139** 164511
- [16] Doremus R H 2003 *Am. Ceram. Soc. Bull.* **82** 1
- [17] Bruning R and Sutton M 1996 *J. Non-Cryst. Solids* **205–7** 480
- [18] Avramov I 1998 *Glastech. Ber. Glass Sci. Technol.* **71C** 198
- [19] Zheng Q, Mauro J C, Ellison A J, Potuzak M and Yue Y 2011 *Phys. Rev. B* **83** 212202
- [20] Russell J K, Giordano D and Dingwell D B 2003 *Am. Miner.* **88** 1390
- [21] Vogel H 1921 *Phys. Z.* **22** 645
Tamman G and Hesse W 1926 *Z. Anorg. Allg. Chem.* **156** 245
Fulcher G S 1925 *J. Am. Ceram. Soc.* **8** 339
- [22] Kauzmann W 1948 *Chem. Rev.* **43** 219
- [23] Richert R and Angell C A 1998 *J. Chem. Phys.* **108** 9016
- [24] Angell C A 1999 *Rigidity Theory and Applications* ed M F Thorpe and P M Duxbury (New York: Kluwer Academic)
- [25] Tanaka H 2003 *Phys. Rev. Lett.* **90** 055701
- [26] Martinez-Garcia J C, Rzoska S J, Drozd-Rzoska A, Martinez-Garcia J and Mauro J C 2013 *Sci. Rep.* **4** 5160
- [27] Adam G and Gibbs J H 1965 *J. Chem. Phys.* **43** 139
- [28] Heuer A 2008 *J. Phys.: Condens. Matter* **20** 373101
- [29] Sciortino F 2005 *J. Stat. Phys.* **05** 1742
- [30] Sastry S, Debenedetti P G and Stillinger F H 1998 *Nature* **393** 554
- [31] Bassler H 1997 *Phys. Rev. Lett.* **58** 767
- [32] Avramov I and Milchev A 1988 *J. Non-Cryst. Solids* **104** 253
- [33] Mauro J C, Yue Y, Ellison A J, Gupta P K and Allan D C 2009 *Proc. Natl Acad. Sci. USA* **106** 19780
- [34] Naumis G G 2006 *J. Non-Cryst. Solids* **352** 4865
- [35] Gupta P K and Mauro J C 2009 *J. Chem. Phys.* **130** 094503
- [36] Ferry J D 1980 *Viscoelastic Properties of Polymers* (New York: Wiley)
- [37] Borizova Z U 1981 *Glassy Semiconductors* (New York: Springer)
- [38] Mazurin O 1983 *Hand Book of Glass Data* (Amsterdam: Elsevier)
- [39] Popescu M 2002 *Non-Crystalline Chalcogenides* (New York: Springer)
- [40] Qin Q and McKenna G B 2006 *J. Non-Cryst. Solids* **352** 2977
- [41] Ravindren S, Gunasekera G, Tucker Z, Diebold A, Boolchand P and Micoulaut M 2013 *J. Chem. Phys.* **140** 134501
- [42] Georgiev D G, Boolchand P and Micoulaut M 2000 *Phys. Rev. B* **62** R9228
- [43] Bhosle S, Boolchand P, Micoulaut M and Massobrio C 2011 *Solid State Commun.* **151** 1851
- [44] Böhmer R, Ngai K L, Angell C A and Plazek D J 1993 *J. Chem. Phys.* **99** 4201
- [45] Ruocco G, Sciortino F, Zamponi F, De Michele C and Scopigno T 2004 *J. Chem. Phys.* **120** 10666
- [46] Chrysikos G D, Kamitsos E I and Yannopoulos Y D 1996 *J. Non-Cryst. Solids* **196** 244
- [47] Chakraborty D and Poolchand P 2014 *J. Phys. Chem. B* **118** 2249
- [48] Wang L M, Angell C A and Richert R 2006 *J. Chem. Phys.* **125** 074505
- [49] Sidebottom D L and Schnell S E 2013 *Phys. Rev. B* **87** 054202
- [50] Angell C A 1971 *J. Phys. Chem.* **78** 3698
- [51] Angell C A and Rao K J 1972 *J. Chem. Phys.* **57** 470
- [52] Angell C A, Richards B E and Velikov V 1999 *J. Phys.: Condens. Matter* **11** A75
- [53] Micoulaut M 2008 *Am. Mineral.* **93** 1732
- [54] Vignarooban K, Boolchand P, Micoulaut M, Malki M and Bresser W J 2014 *Europhys. Lett.* **108** 56001
- [55] Wilson M and Salmon P S 2009 *Phys. Rev. Lett.* **103** 157801
- [56] Wilson M and Madden P A 1997 *Mol. Phys.* **92** 197
- [57] Bhosle S, Gunasekera K, Boolchand P and Micoulaut M 2012 *Int. J. Appl. Glass Sci.* **3** 189
- [58] Wang T, Gulbitten O, Wang R, Yang Z, Smith A, Luther-Davies B and Lucas P 2014 *J. Phys. Chem. B* **118** 1436
- [59] Yang Y, Zhang B, Yang A, Yang Z and Lucas P 2015 *J. Phys. Chem. B* **119** 5096
- [60] Phillips J C 1979 *J. Non-Cryst. Solids* **34** 153
- [61] Thorpe M F 1983 *J. Non-Cryst. Solids* **57** 355
- [62] Smedskjaer M M, Mauro J C and Yue Y 2009 *J. Chem. Phys.* **131** 244514
- [63] Salmon P S, Martin R A, Mason P E and Cuello G J 2005 *Nature* **435** 75
- [64] Salmon P S, Barnes A C, Martin R A and Cuello C J 2006 *Phys. Rev. Lett.* **96** 235502
- [65] Kohara S *et al* 2014 *Nat. Commun.* **5** 5892
- [66] Zeidler A, Salmon P S, Martin R A, Usuki T, Mason P E and Cuello G J 2010 *Phys. Rev. B* **82** 104208
- [67] Zeidler A *et al* 2014 *Phys. Rev. Lett.* **113** 135501
- [68] Salmon P S, Drewitt J W E, Whittaker D A J, Zeidler A, Wezka K, Bull C L, Tucker M G, Wilding M C, Guthrie M and Marrocchelli D 2012 *J. Phys.: Condens. Matter* **24** 415102, 439601
- [69] Bauchy M, Micoulaut M, Boero M and Massobrio C 2013 *Phys. Rev. Lett.* **110** 165501
- [70] Micoulaut M and Bauchy M 2013 *Phys. Status Solidi* **250** 976
- [71] Bauchy M, Kachmar A and Micoulaut M 2014 *J. Chem. Phys.* **141** 194506
- [72] Hosokawa S, Pilgrim W C, Béar J F and Boolchand P 2016 *J. Non-Cryst. Solids* **431** 31
- [73] Scherrer P 1918 *Göttinger Nachr. Ges.* **2** 98
Patterson A 1939 *Phys. Rev.* **56** 978
- [74] Richet P, Roskosz M and Roux J 2006 *Chem. Geol.* **225** 388
- [75] Fang C Y, Yinnon H and Uhlmann D R 1983 *J. Non-Cryst. Solids* **57** 465
- [76] Kohlrausch R 1847 *Ann. Phys., Lpz.* **12** 39
- [77] Sidebottom D L, Rodenburg B V and Changstroem J R 2007 *Phys. Rev. B* **75** 132201
- [78] Buchenau U and Wischnewski A 2004 *Phys. Rev. B* **70** 092201
- [79] Novikov V N and Sokolov A P 2004 *Nature* **431** 961
- [80] Yannopoulos S N and Johari G P 2004 *Nature* **442** E7
- [81] Scopigno T, Ruocco G, Sette F and Monaco G 2003 *Science* **303** 849
- [82] Kargl F, Meyer A, Koza M M and Schöber H 2006 *Phys. Rev. B* **74** 014304
- [83] Sokolov A P, Rössler A, Kisliuk A and Quitmann D 1993 *Phys. Rev. Lett.* **71** 2062
- [84] Sokolov A P, Kisliuk A, Quitmann D, Kudlik A and Rössler R 1994 *J. Non-Cryst. Solids* **172–4** 138
- [85] Yannopoulos S N and Papatheodorou G N 2000 *Phys. Rev. B* **62** 3728
- [86] Bagheria R, Gunasekera K, Boolchand P and Micoulaut M 2014 *Phys. Status Solidi* **251** 1322
- [87] Yang G, Gulbitten O, Gueguen Y, Bureau B, Sangleboeuf J Ch, Roiland C, King E A and Lucas P 2012 *Phys. Rev. B* **85** 144107
- [88] Musgraves J D, Wachtel P, Novak S, Wilkinson J and Richardson K 2011 *J. Appl. Phys.* **110** 063503
- [89] Trachenko K 2006 *J. Phys.: Condens. Matter* **18** L251
- [90] Tandon P 2005 *J. Non-Cryst. Solids* **351** 2210
- [91] Petrávic J 2004 *J. Chem. Phys.* **120** 10188

- [92] Shen J W, Green D J, Tressler R E and Shelleman D L 2003 *J. Non-Cryst. Solids* **324** 277
- [93] Baeurle S A, Hotta A and Gusev A A 2005 *Polymer* **46** 4344
- [94] Hessinger J and Knorr K 1990 *Phys. Rev. Lett.* **65** 2674
- [95] Gueguen Y, Kerryvin V, Rouxel T, Le Fur M, Orain H, Bureau B, Boussard-Plédel C and Sangleboeuf J C 2015 *Mech. Mater.* **85** 47
- [96] Böhmer R and Angell C A 1993 *Phys. Rev. B* **48** 5857
- [97] Gueguen Y, Sangleboeuf J C, Keryvin V, Rouxel T, King E A, Robin E, Delaizir G, Bureau B, Zhang X and Lucas P 2008 *J. Ceram. Soc. Japan* **116** 890
- [98] Anderson P C, Senapati U and Varshneya A K 1994 *J. Non-Cryst. Solids* **176** 51
- [99] Bernard C, Delaizir G, Sangleboeuf J C, Keryvin V, Lucas P, Bureau B, Zhang X and Rouxel T 2007 *J. Eur. Ceram. Soc.* **27** 3253
- [100] Böhmer R, Senapati H and Angell C A 1991 *J. Non-Cryst. Solids* **131–3** 182
- [101] Seaman J H, Lezzi P J, Blanchet T A and Tomozawa M 2014 *J. Non-Cryst. Solids* **403** 113
- [102] Tomozawa M, Lezzi P J, Hepburn R W, Blanchet T A and Cherniak D J 2012 *J. Non-Cryst. Solids* **358** 2650
- [103] Kese K, Theler M and Bergman B 2006 *J. Eur. Ceram. Soc.* **26** 1003
- [104] Kese K, Li Z C and Bergman B 2006 *J. Eur. Ceram. Soc.* **26** 1013
- [105] Welch R W, Smith J R, Potuzak M, Guo X, Bowden B F, Kiczinski T J, Allan D C, King E A, Ellison A J and Mauro J C 2013 *Phys. Rev. Lett.* **110** 265901
- [106] Phillips J C 1996 *Rep. Prog. Phys.* **59** 1133
- [107] Cho J Y, Yang T Y, Park Y J and Jooz Y C 2012 *Electrochem. Solid State Lett.* **15** H81
- [108] Wang L M and Mauro J C 2011 *J. Chem. Phys.* **134** 044522
- [109] Kissinger H E 1957 *Ann. Chem.* **29** 1702
- [110] Moynihan C T, Eastale A J, Wilder J and Tucker J 1974 *J. Phys. Chem.* **78** 2673
- [111] Wang L M, Velikov V and Angell C A 2002 *J. Chem. Phys.* **117** 10184
- [112] Chen Z N, Li Z J, Zhang Y Q, Liu R P, Tian Y J and Wang L M 2014 *Eur. Phys. J. E* **37** 52
- [113] Birge N O and Nagel S R 1985 *Phys. Rev. Lett.* **54** 2674
- [114] Birge N O and Nagel S R 1987 *Rev. Sci. Instrum.* **58** 1464
- [115] Birge B O 1986 *Phys. Rev. B* **34** 1631
- [116] Scheidler P, Kob W, Latz A, Horbach J and Binder K 2001 *Phys. Rev. B* **63** 104204
- [117] Bustin O and Descamps M 1999 *J. Chem. Phys.* **120** 10982
- [118] Carpentier L, Bustin O and Descamps M 2002 *J. Appl. Phys.* **D** **35** 402
- [119] Shawe J E K 1995 *Thermochim. Acta* **260** 1
- [120] Hutchinson J 1998 *Thermochim. Acta* **324** 165
- [121] Havriliak S and Negami S 1966 *J. Polym. Sci. C* **14** 89
- [122] Cole K S and Cole R H 1941 *J. Chem. Phys.* **9** 341
- [123] Richert R 2015 *Adv. Chem. Phys.* **156** 201
- [124] Wang L M, Liu R P, Tian Y J and Richert R 2010 *J. Phys. Chem. B* **114** 3618
- [125] Mandanici A, Huang W, Cutroni M and Richert R 2008 *J. Chem. Phys.* **128** 124505
- [126] Sidebottom D L 2009 *Rev. Mod. Phys.* **81** 999
- [127] Greaves G N and Ngai K L 1995 *Phys. Rev. B* **52** 6358
- [128] Dutta A, Sinha T P, Jena P and Adak S 2008 *J. Non-Cryst. Solids* **354** 3952
- [129] Quinten H J C A, Van Gemert W J Th and Stevels J M 1978 *J. Non-Cryst. Solids* **29** 333
- [130] El-Hadi Z A 2001 *J. Mater. Sci. Technol.* **17** 278
- [131] Roling B 1998 *Solid State Ion.* **105** 185
- [132] Patel H K and Martin S W 2009 *Phys. Rev. B* **45** 10292
- [133] Sidebottom D L and Murray-Krezan C M 2002 *Phys. Rev. Lett.* **89** 195901
- [134] Micoulaut M, Malki M, Novita D I and Boolchand P 2009 *Phys. Rev. B* **80** 184205
- [135] Kargl F and Meyer A 2004 *Chem. Geol.* **213** 165
- [136] Schmidt-Rohr K and Spiess H W 1991 *Phys. Rev. Lett.* **66** 3020
- [137] Gjersing E L, Sen S and Youngmann R E 2010 *Phys. Rev. B* **82** 014203
- [138] Stebbins J F, Sen S and Farnan I 1995 *Am. Mineral.* **80** 861
- [139] Sen S and Stebbins J F 1997 *Phys. Rev. B* **55** 3512
- [140] Maas P, Bunde A and Ingram M D 1992 *Phys. Rev. Lett.* **68** 3064
- [141] Martin S W 1989 *Mater. Chem. Phys.* **23** 225
- [142] Stebbins J F and Sen S 1998 *J. Non-Cryst. Solids* **224** 80
- [143] Sykina K, Bureau B, Le Polle S L, Roiland C, Deschamps M, Pickard C J and Furet E A 2014 *Phys. Chem. Chem. Phys.* **16** 17975
- [144] Sen S, Kaseman D C, Hung I and Gan Z 2015 *J. Phys. Chem. B* **119** 5747
- [145] Deschamps M, Roiland C, Bureau B, Yang G, Le Polle S L and Massiot D 2011 *Solid State Nucl. Magn. Reson.* **40** 72
- [146] Leitner M, Sepiol B, Stadler L, Pfau B and Vogl G 2009 *Nat. Mater.* **8** 717
- [147] Chushkin Y, Caronna C and Madsen A 2012 *J. Appl. Crystallogr.* **45** 807
- [148] Shpyrko O G 2014 *J. Synchr. Radiat.* **21** 1057
- [149] Ruta B, Chushkin Y, Monaco G, Cipelletti L, Pineda E, Bruna P, Giordano P V and Gonzalez-Silveira M 2012 *Phys. Rev. Lett.* **109** 165701
- [150] Ruta B, Baldi G, Monaco G and Chushkin Y 2013 *J. Chem. Phys.* **138** 054508
- [151] Leitner M, Sepiol B and Stadler L M 2012 *Phys. Rev. B* **86** 064202
- [152] Cazzato S, Scopigno T, Yannopoulos S N and Ruocco G 2009 *J. Non-Cryst. Solids* **355** 1797
- [153] Ruta B, Baldi G, Chushkin Y, Rufflé B, Cristofolini L, Fontana A, Zanatta M and Nazzani F 2014 *Nat. Commun.* **5** 3939
- [154] Ross M, Stana M, Leitner M and Sepiol B 2014 *New J. Phys.* **16** 093042
- [155] Tran T D and Sidebottom D L 2013 *J. Am. Ceram. Soc.* **96** 2147
- [156] Fabian R Jr and Sidebottom D L 2009 *Phys. Rev. B* **80** 064201
- [157] Changstrom J R and Sidebottom D L 2008 *J. Phys.: Condens. Matter* **20** 285103
- [158] Tool A Q 1947 *J. Am. Ceram. Soc.* **29** 240
- [159] Narayanaswamy O 1971 *J. Am. Ceram. Soc.* **54** 491
- [160] Moynihan C T *et al* 1976 *Ann. New York Acad. Sci.* **279** 15
- [161] Richert R 2011 *J. Chem. Phys.* **134** 144501
- [162] Svoboda R and Mälek J 2013 *J. Non-Cryst. Solids* **363** 89
- [163] Svoboda R, Honcová P and Mälek J 2010 *J. Non-Cryst. Solids* **356** 447
- [164] Gulbitten O, Mauro J C and Lucas P 2013 *J. Chem. Phys.* **138** 244504
- [165] Abu-Sehly A A, Alamri S N and Joraid A A 2009 *J. Alloys Compd.* **476** 348
- [166] Pilar R, Honcová P, Schulz G, Schick C and Malék J 2015 *Thermochim. Acta* **603** 142
- [167] Slobodian P, Riha P, Rychwalski R W, Emri I, Sáva P and Kubát J 2006 *Eur. Polym. J.* **42** 2824
- [168] Svoboda R, Pustková P and Mälek J 2007 *J. Phys. Chem. Solids* **68** 850
- [169] DeBolt M A, Eastale A J, Macedo P B and Moynihan C T 1976 *J. Am. Ceram. Soc.* **59** 16
- [170] Svoboda R and Mälek J 2015 *J. Alloys Compd.* **627** 287
- [171] Saiter J M, Chebli K and Hamou A 2000 *Physica B* **293** 98
- [172] Mälek J 1998 *Thermochim. Acta* **311** 183
- [173] Mälek J and Svejka R 1994 *J. Non-Cryst. Solids* **172–4** 635

- [174] Svoboda R, Honcovà P and Malèk J 2011 *J. Non-Cryst. Solids* **357** 2163
- [175] Hodge I M 1991 *J. Non-Cryst. Solids* **131–3** 435
- [176] Hodge I M 1997 *J. Res. Natl Inst. Stand. Technol.* **102** 195
- [177] Moynihan C T, Eastale A J, DeBolt M A and Tucker J 1976 *J. Am. Ceram. Soc.* **59** 12
- [178] Hutchinson J M and Kovacs A J 1984 *Polym. Eng. Sci.* **24** 1087
- [179] Hutchinson J M and Ruddy M 1988 *J. Polym. Sci. B* **26** 2341
- [180] Hutchinson J M and Ruddy M 1990 *J. Polym. Sci. B* **28** 2127
- [181] Svoboda R, Honcovà P and Malèk J 2012 *J. Non-Cryst. Solids* **358** 804
- [182] Saiter J M 2001 *J. Opt. Adv. Mater.* **3** 685
- [183] Golovchak R, Kozdras A, Balitska A and Shpotyuk O 2012 *J. Phys.: Condens. Matter* **24** 505106
- [184] Mijovic J, Nicolais L, D'Amore A and Kenny J M 1994 *Polym. Eng. Sci.* **34** 381
- [185] Grassia L and D'Amore A 2011 *J. Non-Cryst. Solids* **357** 414
- [186] Grassia L and Simon S L 2012 *Polymer* **53** 3613
- [187] Svoboda R and Malèk J 2013 *J. Therm. Anal. Calorim.* **113** 831
- [188] Svoboda R and Malèk J 2013 *J. Non-Cryst. Solids* **378** 186
- [189] Malèk J, Svoboda R, Pustková P and Cicmanec P 2009 *J. Non-Cryst. Solids* **355** 264
- [190] Starr F W, Angell C A, La Nave E, Sastry S, Scala A, Sciortino F and Stanley H E 2003 *Biophys. Chem.* **105** 573
- [191] Scala A, Starr F W, La Nave E, Sciortino F and Stanley H E 2000 *Nature* **406** 166
- [192] Mossa S, La Nave E, Stanley H E, Donati C, Sciortino F and Tartaglia P 2002 *Phys. Rev. E* **65** 041205
- [193] Sakai-Voivod I, Poole P H and Sciortino F 2001 *Nature* **412** 514
- [194] Richet P 2009 *J. Non-Cryst. Solids* **355** 628
- [195] Urbain G, Bottinga Y and Richet P 1982 *Geochim. Cosmochim. Acta* **46** 1061
- [196] Scarfe C M, Cronin D J, Wenzel J T and Kaufman D A 1983 *Am. Mineral.* **68** 1083
- [197] Hummel W J and Arndt J 1985 *Contrib. Mineral. Petrol.* **90** 83
- [198] Sipp A, Bottinga Y and Richet P 2001 *J. Non-Cryst. Solids* **288** 166
- [199] Angell C A, Finch E D, Woolf L A and Bach P 1976 *J. Chem. Phys.* **65** 3063
- [200] Sciortino F, Kob W and Tartaglia P 1999 *Phys. Rev. Lett.* **83** 3214
- [201] Roland C M, Cappaccioli S, Lucchesi M and Casalini R 2004 *J. Chem. Phys.* **120** 10640
- [202] Mathot V B F 1984 *Polymer* **25** 579
- [203] Angell C A and Sichina W 1976 *Ann. New York Acad. Sci.* **279** 53
- [204] Angell C A and Bressel R D 1972 *J. Non-Cryst. Solids* **76** 3244
- [205] Dyre J C, Hechsher T and Niss K 2009 *J. Non-Cryst. Solids* **355** 624
- [206] Wooten F, Winer K and Weaire D 1985 *Phys. Rev. Lett.* **54** 1392
- [207] Keating P N 1966 *Phys. Rev.* **145** 637
- [208] Holender J M and Morgan G J 1991 *J. Phys: Condens. Matter* **3** 7241
- [209] Barkema G T and Mousseau N 2000 *Phys. Rev. B* **62** 4985
- [210] Laaziri K, Kycia S, Roorda S, Chicoine M, Robertson J L, Wang J and Moss S C 1999 *Phys. Rev. Lett.* **82** 3460
- [211] Djordjević B R, Thorpe M F and Wooten F 1995 *Phys. Rev. B* **52** 5685
- [212] Dong J J and Drabold D A 1998 *Phys. Rev. Lett.* **80** 1928
- [213] Bonilla L L, Padilla F G and Ritort F 1998 *Physica A* **250** 315
- [214] Ritort F 2005 *J. Phys. Chem. B* **109** 6787
- [215] Garriga A and Ritort F 2005 *Phys. Rev. E* **72** 031505
- [216] Micoulaut M 2010 *J. Phys.: Condens. Matter* **22** 285101
- [217] Kamitakahara W A, Cappelletti R L, Boolchand P, Halfpap B, Gompf F, Neumann D A and Mutka H 1991 *Phys. Rev. B* **44** 94
- [218] Price D L and Carpenter J M 1987 *J. Non-Cryst. Solids* **92** 153
- [219] Cappelletti R, Cobb M, Drabold D A and Kamitakahara W A 1995 *Phys. Rev. B* **52** 9133
- [220] Yan L, Düring G and Wyart M 2013 *Proc. Natl Acad. Sci. USA* **110** 6307
- [221] Kovacs A J, Aklonis J J, Hutchinson J M and Ramos A R 1979 *J. Polym. Sci.* **17** 1097
- [222] Ngai K L and Rendell R W 1998 *Phil. Mag.* **77** 621
- [223] Ngai K L 1996 *Colloid Interface Sci.* **64** 1
- [224] McDonald J R 1998 *J. Appl. Phys.* **84** 812
- [225] Hodge I M 1994 *J. Non-Cryst. Solids* **169** 211
- [226] Jenkins M J and Hay J N 2001 *Comput. Theor. Polym. Sci.* **11** 283
- [227] Munoz A and Cumbresa F L 1992 *Thermochim. Acta* **196** 137
- [228] Guo X, Potuzak M, Mauro J C, Allan D C, Kiczinski T J and Yue Y 2011 *J. Non-Cryst. Solids* **357** 3230
- [229] Tanaka S 1984 *Solid State Commun.* **54** 867
- [230] Sreeram A N, Swiler D R and Varshneya A K 1991 *J. Non-Cryst. Solids* **127** 287
- [231] Senapati U and Varshneya A K 1995 *J. Non-Cryst. Solids* **185** 289
- [232] Gibbs J H and Di Marzio E A 1958 *J. Chem. Phys.* **28** 373
- [233] Micoulaut M and Naumis G G 1999 *Europhys. Lett.* **47** 568
- [234] Kerner R and Micoulaut M 1997 *J. Non-Cryst. Solids* **210** 298
- [235] Micoulaut M 1998 *Eur. Phys. J. B* **1** 277
- [236] Feng X, Bresser W J and Boolchand P 1997 *Phys. Rev. Lett.* **78** 4422
- Ota R, Yamate T, Soga N and Kumuyi S 1978 *J. Non-Cryst. Solids* **29** 67
- [237] Saffarini G 1994 *Appl. Phys. A* **59** 385
- [238] Selvanathan D, Bresser W J and Boolchand P 2000 *Phys. Rev. B* **61** 15061
- [239] Sarrach D J and DeNeufville J P 1976 *J. Non-Cryst. Solids* **22** 245
- [240] Norban B, Pershing D, Enzweiler R N, Boolchand P, Griffiths J E and Phillips J C 1987 *Phys. Rev. B* **36** 8109
- [241] Naumis G G 2005 *Phys. Rev. B* **73** 172202
- [242] Micoulaut M and Naumis G G 2002 *Recent Research Developments in Non-crystalline Solids* vol 2, ed S G Pandalai (Trivandrum: Transworld Research Network) p 363
- [243] Wang Y, Boolchand P and Micoulaut M 2000 *Europhys. Lett.* **52** 633
- [244] Chakravarty S, Georgiev D G, Boolchand P and Micoulaut M 2005 *J. Phys.: Condens. Matter* **17** L1
- [245] Phillips W A, Buchenau U, Nücker N, Dianoux A J and Petry W 1989 *Phys. Rev. Lett.* **63** 2381
- [246] Affatigato M, Feller S, Khaw E J, Feil D, Teoh B and Mathews O 1990 *Phys. Chem. Glasses* **31** 19
- [247] Shelby J E and Ruller J 1987 *Phys. Chem. Glasses* **28** 262
- [248] Boolchand P, Georgiev D G, Qu T, Wang F, Cai L and Chakravarty S 2002 *C. R. Chim.* **5** 713
- [249] Bresser W J and Boolchand P 2000 *Phil. Mag.* **80** 1757
- [250] Lagrange J L 1788 *Méc. Anal.* (Paris)
- [251] Maxwell J C 1864 *Phil. Mag.* **27** 294
- [252] Phillips J C 1983 *Phys. Rev. B* **28** 7038
- [253] Phillips J C 1982 *Phys. Today* **35** 27
- [254] Boolchand P and Thorpe M F 1994 *Phys. Rev. B* **50** 10366
- [255] Zhang M and Boolchand P 1994 *Science* **266** 1355
- [256] Bresser W J, Suranyi P and Boolchand P 1986 *Phys. Rev. Lett.* **56** 2493
- [257] Azoulay R, Thibierge H and Brenac A 1975 *J. Non-Cryst. Solids* **18** 33

- [258] He H and Thorpe M F 1985 *Phys. Rev. Lett.* **54** 2107
- [259] Thorpe M F 1985 *J. Non-Cryst. Solids* **76** 109
- [260] Boolchand P, Bresser W J, Zhang M, Wu Y, Wells J and Enzweiler R N 1995 *J. Non-Cryst. Solids* **82** 143
- [261] Bohmer R A and Angell C A 1992 *Phys. Rev. B* **45** 1091
- [262] Duquesne J Y and Bellessa G 1985 *J. Phys. Colloq.* **46** C10-445
- [263] Gump J, Finkler I, Xia H, Sooryakumar R, Bresser W J and Boolchand P 2004 *Phys. Rev. Lett.* **92** 245501
- [264] Asokan S, Prasad M Y N and Parthasarathy G 1989 *Phys. Rev. Lett.* **62** 808
- [265] Thorpe M F and Duxbury P M (eds) 1999 *Rigidity Theory, Applications* (New York: Academic)
- [266] Thorpe M F and Phillips J C (eds) 2001 *Phase Transitions, Self-organization in Electronic, Molecular Networks* (New York: Kluwer Academic)
- [267] Micoulaut M and Popescu M (eds) 2009 *Rigidity, Boolchand Intermediate Phases in Nanomaterials* (Bucharest: INOE Publishing House)
- [268] Chubynsky M V, Brière M A and Mousseau N 2006 *Phys. Rev. E* **74** 016116
- [269] Huerta A and Naumis G G 2002 *Phys. Lett. A* **299** 660
- [270] Huerta A and Naumis G G 2002 *Phys. Rev. B* **66** 184204
- [271] Naumis G G 2005 *Phys. Rev. B* **71** 026114
- [272] Foffi G and Sciortino F 2006 *Phys. Rev. E* **74** 050401
- [273] Gupta P K and Mauro J C 2007 *J. Chem. Phys.* **126** 224504
- [274] Bauchy M and Micoulaut M 2013 *Phys. Rev. Lett.* **110** 095501
- [275] Mauro J C, Gupta P K and Loucks R J 2009 *J. Chem. Phys.* **130** 234503
- [276] Hermansen C, Youngman R E, Wang J and Yue Y 2015 *J. Chem. Phys.* **142** 184503
- [277] Rodrigues B P, Mauro J C, Yue Y and Wondraczek L 2014 *J. Non-Cryst. Solids* **405** 12
- [278] Hermansen C, Mauro J C and Yue Y 2014 *J. Chem. Phys.* **140** 154501
- [279] Smedskjaer M, Mauro J C, Youngman R E, Hogue C L, Potuzak M and Yue Y 2011 *J. Phys. Chem. B* **115** 12930
- [280] Smedskjaer M M, Mauro J C and Yue Y 2010 *Phys. Rev. Lett.* **105** 115503
- [281] Araujo R J and Mauro J C 2010 *J. Am. Ceram. Soc.* **93** 1026
- [282] Micoulaut M, Kachmar A, Bauchy M, Le Roux S, Massobrio C and Boero M 2013 *Phys. Rev. B* **88** 054203
- [283] Massobrio C, Micoulaut M and Salmon P S 2010 *Solid State Sci.* **12** 199
- [284] Micoulaut M, Vuilleumier R and Massobrio M 2009 *Phys. Rev. B* **79** 214204
- [285] Micoulaut M, Guissani Y and Guillot B 2006 *Phys. Rev. E* **73** 031504
- [286] Zeidler A *et al* 2014 *Phys. Rev. B* **90** 024206
- [287] Ferlat G, Charpentier T, Seitsonen A P, Takada A, Lazzeri M, Cormier L, Calas G and Mauri F 2008 *Phys. Rev. Lett.* **101** 065504
- [288] Drabold D A, Li J and Tafel D N 2003 *J. Phys.: Condens. Matter* **15** S1529
- [289] Bauchy M and Micoulaut M 2013 *J. Non-Cryst. Solids* **377** 34
- [290] Opletal G, Wang R P and Russo S P 2015 *J. Phys. Chem. A* **118** 4790
- [291] Celino M and Massobrio C 2003 *Phys. Rev. Lett.* **90** 125502
- [292] Massobrio C, Celino M, Salmon P S, Martin R A, Micoulaut M and Pasquarello A 2009 *Phys. Rev. B* **79** 174201
- [293] Cormack A N, Du J and Zeitler J N 2002 *Phys. Chem. Chem. Phys.* **4** 3193
- [294] Horbach J and Kob W 1999 *Phil. Mag. B* **79** 1981
- [295] Du J and Cormack A N 2004 *J. Non-Cryst. Solids* **349** 66
- [296] Bauchy M, Guillot B, Micoulaut M and Sator N 2013 *Chem. Geol.* **346** 47
- [297] Du J and Corrales L R 2006 *J. Phys. Chem. B* **110** 22346
- [298] Cormack A N and Du J 2001 *J. Non-Cryst. Solids* **293** 283
- [299] Laurent L, Mantsi B and Micoulaut M 2014 *J. Phys. Chem. B* **118** 12750
- [300] Pedesseau L, Ispas S and Kob W 2015 *Phys. Rev. B* **91** 134202
- [301] Cormier L, Ghaleb D, Delaye J M and Calas G 2000 *Phys. Rev. B* **61** 14495
- [302] Winkler A, Horbach J, Kob W and Binder K 2003 *J. Chem. Phys.* **120** 384
- [303] Wilcek F 2004 *Phys. Today* **57** 10
- [304] Micoulaut M, Otjacques C, Raty J Y and Bichara C 2010 *Phys. Rev. B* **81** 174206
- [305] Bauchy M, Micoulaut M, Celino M, Boero M, Le Roux S and Massobrio C 2011 *Phys. Rev. B* **83** 054201
- [306] Bauchy M and Micoulaut M 2011 *J. Non-Cryst. Solids* **357** 2530
- [307] Hussein R, Dupree R and Holland D 1999 *J. Non-Cryst. Solids* **246** 159
- [308] Gunasekera K, Boolchand P and Micoulaut M 2014 *J. Appl. Phys.* **115** 164905
- [309] Micoulaut M, Gunasekera K, Ravindren S and Boolchand P 2014 *Phys. Rev. B* **90** 094207
- [310] Bauchy M and Micoulaut M 2015 *Nat. Commun.* **6** 6398
- [311] Bauchy M, Qomi M J A, Bichara C, Ulm F J and Pellenq R J M 2014 *Phys. Rev. Lett.* **114** 125502
- [312] Bauchy M, Qomi M J A, Bichara C, Ulm F J and Pellenq R J M 2014 *J. Phys. Chem. C* **118** 12485
- [313] Mousseau N and Thorpe M F 1995 *Phys. Rev. B* **52** 2660
- [314] Micoulaut M, Flores-Ruiz H and Bauchy M 2015 *Molecular Dynamics Simulations of Disordered Materials (Springer Series in Materials Science vol 215)* p 275
- [315] Bermejo F J, Cabrillo C, Bychkov E, Fouquet P, Ehlers G, Häussler W, Price D L and Saboungi M L 2008 *Phys. Rev. Lett.* **100** 245902
- [316] Pacaud F and Micoulaut M 2015 *J. Chem. Phys.* **143** 064502
- [317] Bauchy M and Micoulaut M 2013 *Europhys. Lett.* **104** 56002
- [318] Allen M P and Tildesley D J 1987 *Computer Simulations of Liquids* (Oxford: Oxford University Press)
- [319] Bauchy M and Micoulaut M 2011 *Phys. Rev. B* **83** 184118
- [320] Bauchy M, Qomi M J, Bichara C, Ulm F J and Pellenq R J M 2014 arXiv:1410.2916
- [321] Mantsi B, Bauchy M and Micoulaut M 2015 *Phys. Rev. B* **92** 134201
- [322] Trachenko K and Dove M T 2002 *J. Phys.: Condens. Matter* **14** 1143
- [323] Chakraborty S, Boolchand P, Malki M and Micoulaut M 2014 *J. Chem. Phys.* **140** 014503
- [324] Boolchand P, Georgiev D G and Goodman B 2001 *J. Optoelectr. Adv. Mater.* **3** 703
- [325] Guoa X, Mauro J C, Allan D C and Yue Y 2012 *J. Non-Cryst. Solids* **358** 1710
- [326] Lucas P, King E A, Gulbitten O, Yarger J L, Soignard E and Bureau B 2010 *Phys. Rev. B* **80** 214114
- [327] Golovchak R, Jain H, Spotyuk O, Kozdras A, Saiter A and Saiter J M 2008 *Phys. Rev. B* **78** 014202
- [328] Shpotyuk O and Golovchak R 2011 *Phys. Status Solidi C* **8** 2572
- [329] Chen P, Boolchand P and Georgiev D G 2010 *J. Phys.: Condens. Matter* **22** 065104
- [330] Chen P, Holbrook C, Boolchand P, Georgiev D G and Micoulaut M 2008 *Phys. Rev. B* **78** 224208
- [331] Georgiev D G, Boolchand P, Eckert H, Micoulaut M and Jackson K A 2003 *Europhys. Lett.* **62** 49
- [332] Boolchand P, Chen P and Vempati U 2009 *J. Non-Cryst. Solids* **355** 1773
- [333] Wang F, Boolchand P, Jackson K A and Micoulaut M 2007 *J. Phys.: Condens. Matter* **19** 226201

- [334] Wang Y, Wells J, Georgiev D G, Boolchand P, Jackson K A and Micoulaut M 2001 *Phys. Rev. Lett.* **A 87** 5503
- [335] Qu T and Boolchand P 2005 *Phil. Mag.* **85** 875
- [336] Vempati U and Boolchand P 2004 *J. Phys.: Condens. Matter* **16** S5121
- [337] Gunasekera K, Boolchand P and Micoulaut M 2013 *J. Phys. Chem. B* **117** 10027
- [338] Das C, Kiran M R S N, Ramamurty U and Asokan S 2012 *Solid State Commun.* **152** 2181
- [339] Varma G S, Das C and Asokan S 2014 *Solid State Commun.* **177** 108
- [340] Boolchand P 2015 unpublished results
- [341] Rompicharla R, Novita D I, Chen P, Boolchand P, Micoulaut M and Huff W 2008 *J. Phys.: Condens. Matter* **20** 202101
- [342] Raty J Y, Otjacques C, Gaspard J P and Bichara C 2010 *Solid State Sci.* **12** 193
- [343] Kalikka J, Akola J, Jones R O, Kohara S and Usuki T 2012 *J. Phys.: Condens. Matter* **24** 015802
- [344] Wang F, Mamedov S, Boolchand P, Goodman B and Chandrasekhar M 2005 *Phys. Rev. B* **71** 174201
- [345] Novita D I, Boolchand P, Malki M and Micoulaut M 2007 *Phys. Rev. Lett.* **98** 195501
- [346] Bourgel C, Micoulaut M, Malki M and Simon P 2009 *Phys. Rev. B* **79** 024201
- [347] Micoulaut M and Malki M 2010 *Phys. Rev. Lett.* **105** 235504
- [348] Thorpe M F, Jacobs D J, Chubynsky M V and Phillips J C 2000 *J. Non-Cryst. Solids* **266–9** 859
- [349] Barré J, Bishop A R, Lookman T and Saxena A 2005 *Phys. Rev. Lett.* **94** 208701
- [350] Micoulaut M and Phillips J C 2003 *Phys. Rev. B* **67** 104204
- [351] Brière M A, Chubynsky M V and Mousseau N 2007 *Phys. Rev. E* **75** 056108
- [352] Thorpe M F and Chubynsky M V 2001 *Phase Transitions and Self-organization in Electronic and Molecular Networks* (New York: Kluwer Academic) p 43
- [353] Jacobs D J and Thorpe M F 1995 *Phys. Rev. Lett.* **75** 4051
- [354] Yan L and Wyart M 2014 *Phys. Rev. Lett.* **113** 215504
- [355] Micoulaut M and Phillips J C 2007 *J. Non-Cryst. Solids* **353** 1732
- [356] Ellenbroek W G, Zeravcic Z, van Saarloos W and van Hecke M 2009 *Europhys. Lett.* **87** 34004
- [357] Wyart M, Liang H, Kabla A and Mahadevan L 2008 *Phys. Rev. Lett.* **101** 215501
- [358] Moukarzel C 2013 *Phys. Rev. E* **88** 062121
- [359] Moukarzel C, Duxbury P M and Leath P L 1997 *Phys. Rev. E* **55** 5800
- [360] Moukarzel C F 2003 *Phys. Rev. E* **68** 056104
- [361] Duxbury P M, Jacobs D J, Thorpe M F and Moukarzel C 1999 *Phys. Rev. E* **59** 2084
- [362] Shpotyuk O, Hyla M, Boyko V and Golovchak R 2008 *Physica B* **403** 3830
- [363] Jacobs D J, Rader A J, Kuhn L A and Thorpe M F 2001 *Proteins* **44** 150
- [364] Phillips J C 2002 *Phys. Rev. Lett.* **88** 216401
- [365] Monasson R, Zecchina R, Kirkpatrick S, Selman B and Troyansky L 1999 *Nature* **400** 133
- [366] Frenkel D and Smit B 1996 *Understanding Molecular Simulation—from Algorithms to Applications* (San Diego, CA: Academic)
- [367] Binder K and Ciccotti G 1996 *Monte Carlo and Molecular Dynamics of Condensed Matter Systems* (Bologna: Italian Physical Society)
- [368] Binder K and Kob W 2011 *Glassy Materials and Disordered Solids* (Singapore: World Scientific)
- [369] Horbach J and Kob W 1999 *Phys. Rev. B* **60** 3169
- [370] Horbach J, Kob W and Binder K 2001 *Chem Geol.* **174** 87
- [371] Kramer G J, de Man A J M and van Santen R A 1991 *J. Am. Chem. Soc.* **113** 6435
- [372] Cormack A N, Du J and Zeitler T R 2003 *J. Non-Cryst. Solids* **323** 147
- [373] Micoulaut M and Massobrio C 2009 *J. Optoelectr. Adv. Mater.* **11** 1907
- [374] Mikkelsen J C 1984 *Appl. Phys. Lett.* **45** 1187
- [375] Brébec G, Seguin R, Sella C, Bevenot J and Martin J C 1980 *Acta Metall.* **28** 327
- [376] Shimizu N and Kushiro I 1984 *Geochim. Cosmochim. Acta* **48** 1295
- [377] Tinker D, Leshner C E, Baxter G M, Uchida T and Wang Y 2004 *Am. Mineral.* **89** 1701
- [378] Hansen J P and Mc Donald R 1986 *Theory of Simple Liquids* (New York: Academic)
- [379] Kob W, Donati C, Plimpton S J, Poole P H and Glotzer S C 1997 *Phys. Rev. Lett.* **79** 2827
- [380] Rahmann A 1964 *Phys. Rev.* **136** A405
- [381] Matharoo G S, Gulam Razul M S and Poole P H 2006 *Phys. Rev. E* **74** 050502
- [382] Vogel M and Glotzer S 2005 *Phys. Rev. E* **70** 061504
- [383] Kerrache A, Teboul V, Guichaoua D and Monteil A 2003 *J. Non-Cryst. Solids* **322** 41
- [384] Van Hoang V 2005 *Phys. Rev. B* **75** 174202
- [385] Weeks E R, Crocker J C, Levitt A C, Schofield A and Weitz D A 2000 *Science* **287** 627
- [386] Saltzmann E J and Schweizer K S 2006 *Phys. Rev. E* **74** 061501
- [387] Chadhuri P, Berthier L and Kob W 2007 *Phys. Rev. Lett.* **99** 060604
- [388] Horbach J and Kob W 2001 *Phys. Rev. E* **64** 041503
- [389] Nijboer B R A and Rahmann A 1966 *Physica* **32** 415
- [390] Coslovich D and Pastore G 2009 *J. Phys.: Condens. Matter* **21** 285107
- [391] Chaudhuri P, Hurtado P I, Berthier L and Kob W 2015 *J. Chem. Phys.* **142** 74503
- [392] Horbach J, Kob W and Binder K 2003 *J. Phys.: Condens. Matter* **15** S903
- [393] Kieffer J 1994 *J. Non-Cryst. Solids* **172–4** 1285
- [394] Fullerton S K and Maranas J K 2004 *J. Chem. Phys.* **121** 8562
- [395] Morgan N A and Spera F J 2001 *Geochim. Cosmochim. Acta* **65** 4019
- [396] Massobrio C, Pasquarello A and Car R 1999 *J. Am. Chem. Soc.* **121** 2943
- [397] Micoulaut M, Le Roux S and Massobrio C 2012 *J. Chem. Phys.* **136** 224504
- [398] Ediger M D 2000 *Ann. Rev. Phys. Chem.* **51** 99
- [399] Whitelam S, Berthier L and Garrahan J P 2004 *Phys. Rev. Lett.* **92** 185705
- [400] Biroli G and Bouchaud J P 2004 *Europhys. Lett.* **67** 21
- [401] Lačević N, Starr F W, Schroeder T B and Glotzer S C 2003 *J. Chem. Phys.* **119** 7372
- [402] Berthier L, Biroli G, Bouchaud J P, Cipeletti L and van Saarloos W (ed) 2011 *Dynamical Heterogeneities in Glasses, Colloids, and Granular Media* (Oxford: Oxford University Press)
- [403] Vogel M and Glotzer S C 2004 *Phys. Rev. Lett.* **92** 255901
- [404] Donati C, Glotzer S C and Poole P H 1999 *Phys. Rev. Lett.* **82** 5064
- [405] Berthier L 2004 *Phys. Rev. E* **69** 020201
- [406] Berthier L and Biroli G 2011 *Rev. Mod. Phys.* **83** 587
- [407] Dauchot O, Marty G and Biroli G 2005 *Phys. Rev. Lett.* **95** 265701
- [408] Hurley M M and Harrowell P 1995 *Phys. Rev. E* **52** 1694
- [409] Berthier L, Biroli G, Bouchaud J P, Kob W, Miyazaki K and Reichmann D 2007 *J. Chem. Phys.* **126** 184503
- [410] Toninelli C, Wyart M, Berthier L, Biroli G and Bouchaud J P 2005 *Phys. Rev. E* **71** 041505
- [411] Berthier L, Biroli G, Bouchaud J P, Kob W, Miyazaki K and Reichmann D 2007 *J. Chem. Phys.* **126** 184504

- [412] Wahnström G 1991 *Phys. Rev. A* **44** 3752
- [413] Doliwa B and Heuer A 2000 *Phys. Rev. E* **61** 6898
- [414] Whitelam S and Garrahan J P 2004 *J. Phys. Chem. B* **108** 6611
- [415] Flenner E and Szamel G 2010 *Phys. Rev. Lett.* **105** 217801
- [416] Karmakara S, Dasgupta C and Sastry S 2009 *Proc. Acad. Nat. Sci.* **106** 3675
- [417] Stanley H E 1971 *Introduction to Phase Transitions and Critical Phenomena* (New York: Oxford University Press)
- [418] Berhler L, Biroli G, Bouchaud J P, Cipelletti L, El Masri D, Lhôte D, Ladiou F and Pierro M 2005 *Science* **310** 1797
- [419] Berthier L 2007 *Phys. Rev. E* **76** 011507
- [420] Swallen S F, Bonvallet P A, McMahon R J and Ediger M 2003 *Phys. Rev. Lett.* **90** 015901
- [421] Mapes M K, Swallen S F and Ediger M 2006 *J. Phys. Chem. B* **110** 507
- [422] Chang J and Silliescu H 1997 *J. Phys. Chem. B* **101** 8794
- [423] Fernandez-Alonso F *et al* 2007 *Phys. Rev. Lett.* **98** 077801
- [424] Yu H B, Samwer K, Wu Y and Wang W H 2012 *Phys. Rev. Lett.* **109** 095508
- [425] Brillo J, Pommrich A I and Meyer A 2011 *Phys. Rev. Lett.* **107** 165902
- [426] Han X J and Schöber H R 2011 *Phys. Rev. B* **83** 224201
- [427] Soso G C, Behler J and Bernasconi M 2012 *Phys. Status Solidi* **249** 1880
- [428] Orava J, Greer A L, Gholipour B, Hewak D W and Smith C E 2012 *Nat. Mater.* **11** 279
- [429] Soso G C, Colombo J, Behler J, Del Gado E and Bernasconi M 2014 *J. Chem. Phys.* **118** 13621
- [430] Mallamace F, Branca C, Corsaro C, Leone N, Sporeen J, Chen S-H and Stanley H E 2009 *Proc. Natl Acad. Sci.* **107** 22457
- [431] Blondel O and Toninelli C 2014 *Europhys. Lett.* **107** 26005
- [432] Jung Y I, Garrahan J P and Chandler D 2004 *Phys. Rev. E* **69** 061205
- [433] Mauro J C and Ellison A J 2011 *J. Non-Cryst. Solids* **357** 3924
- [434] Goldstein M 1969 *J. Chem. Phys.* **51** 3728
- [435] Stillinger F H and Weber T A 1982 *Phys. Rev. A* **25** 978
- [436] Stillinger F H 1995 *Science* **267** 1935
- [437] Stillinger F H and Weber T A 1984 *Science* **225** 983
- [438] Béland L K, Brommer P, El-Mellouhi F, Joly J F and Mousseau N 2011 *Phys. Rev. E* **84** 046704
- [439] El-Mellouhi F, Mousseau N and Lewis L J 2008 *Phys. Rev. B* **78** 153202
- [440] Wales D J and Doye J P K 1997 *J. Phys. Chem. A* **101** 5111
- [441] Carr J M, Trygubenko S A and Wales D J 2005 *J. Chem. Phys.* **122** 234903
- [442] Calvo F 2010 *Phys. Rev. E* **82** 046703
- [443] Becker O M and Karplus M 1997 *J. Chem. Phys.* **106** 1495
- [444] Wales D J 2004 *Energy Landscapes* (Cambridge: Cambridge University Press)
- [445] La Nave E, Mossa S, De Michele C, Sciortino F and Tartaglia P 2003 *J. Phys.: Condens. Matter* **15** S1085
- [446] Jund P and Jullien R 1999 *Phys. Rev. Lett.* **83** 2210
- [447] Bembenek S D and Laird B B 2001 *J. Chem. Phys.* **114** 2340
- [448] Saksaengwijit A, Reinisch J and Heuer A 2004 *Phys. Rev. Lett.* **93** 235701
- [449] Saika-Voivod I, Poole P H and Sciortino F 2004 *Phys. Rev. E* **69** 041503
- [450] Büchner S and Heuer A 1999 *Phys. Rev. E* **60** 6507
- [451] Büchner S and Heuer A 2000 *Phys. Rev. Lett.* **84** 2168
- [452] Lacks D J 2001 *Phys. Rev. Lett.* **87** 225502
- [453] Lacks D J 2003 *J. Chem. Phys.* **118** 1593
- [454] Doliwa B and Heuer A 2003 *Phys. Rev. E* **67** 030501
- [455] Doliwa B and Heuer A 2003 *Phys. Rev. E* **67** 031506
- [456] Denny R A, Reichman D R and Bouchaud J P 2003 *Phys. Rev. Lett.* **90** 025503
- [457] Cugliandolo L F and Kurchan J 1993 *Phys. Rev. Lett.* **71** 173
- [458] Cugliandolo L F and Kurchan J 1994 *J. Phys. A* **27** 5749
- [459] Franz S and Mézard M 1994 *Europhys. Lett.* **26** 209
- [460] Cugliandolo L F, Kurchan J and Peliti L 1997 *Phys. Rev. E* **55** 3898
- [461] Kurchan J 2005 *Nature* **433** 222
- [462] Bertier L and Barrat J L 2002 *Phys. Rev. Lett.* **89** 095702
- [463] Kob W and Barrat J L 1999 *Europhys. Lett.* **46** 637
- [464] Ono I K, O'Hern C S, Durian D J, Langer S A, Liu A J and Nagel S R 2002 *Phys. Rev. Lett.* **89** 095703
- [465] Mossa S, La Nave E, Sciortino F and Tartaglia P 2002 *Eur. Phys. J. B* **30** 351
- [466] Fielding S and Sollich P 2002 *Phys. Rev. Lett.* **88** 050603
- [467] Pérez-Madrid A, Reguera D and Rubi J M 2002 *Physica A* **329** 357
- [468] Cates M and Evans M (eds) 2000 *Soft and Fragile Matter, Aging in Glassy Systems* (Bristol: Institute of Physics Publishing)
- [469] Cugliandolo L 2011 *J. Phys. A: Math. Theor.* **44** 483001
- [470] Berthier L 2007 *Phys. Rev. Lett.* **98** 220601
- [471] Bouchaud J P 1992 *J. Phys.* **2** 1705
- [472] Mézard M, Parisi G and Virasoro M 1986 *Spin Glass Theory & Beyond* (Singapore: World Scientific)
- [473] Monthus C and Bouchaud J P 1996 *J. Phys. A: Math. Gen.* **29** 3847
- [474] Odagaki T 1995 *Phys. Rev. Lett.* **75** 3701
- [475] Odagaki T and Yoshimori A 2000 *J. Phys.: Condens. Matter* **12** 6509
- [476] Kob W and Barrat J L 1999 *Physica A* **263** 234
- [477] Warren M and Rotter J 2013 *Phys. Rev. Lett.* **110** 025501
- [478] Parsaeian A and Castillo H E 2008 *Phys. Rev. E* **78** 060105
- [479] Castillo H E and Parsaeian A 2007 *Nat. Phys.* **3** 26
- [480] Vollmayr-Lee K, Bjorkquist R and Chambers L M 2013 *Phys. Rev. Lett.* **110** 017801
- [481] Yunker Y, Zhang Z, Aptowicz K B and Yodh A G 2009 *Phys. Rev. Lett.* **103** 115701
- [482] Warren M and Rottler J 2009 *Europhys. Lett.* **88** 58005
- [483] Warren M and Rottler J 2010 *Phys. Rev. Lett.* **104** 205501
- [484] Joule J 1884 *The Scientific Papers of J.P. Joule* vol 1 (London: Physical Society) p 558
- [485] Joule J P 1867 *Manchester Literary and Philosophical Society* p 292
- [486] Nemilov S V 2000 *Glass Phys. Chem.* **26** 511
- [487] Nemilov S V 2001 *Glass Phys. Chem.* **27** 214
- [488] Nemilov S V and Johari G P 2003 *Phil. Mag.* **83** 3117
- [489] Kaseman D C, Endo T and Sen S 2013 *J. Non-Cryst. Solids* **359** 33
- [490] Levelut C, Faivre A, Le Parc R, Champagnon B, Hazemann J L, David L, Rochas C and Simon J P 2002 *J. Non-Cryst. Solids* **307–10** 426
- [491] Lynch J M, Cianci G C and Weeks E R 2008 *Phys. Rev. E* **78** 031410
- [492] Struik L C E 1978 *Physical aging in Amorphous Polymers and Other Materials* (New York: Elsevier)
- [493] Saiter J M, Arnoult M and Grenet J 2005 *Physica B* **355** 370
- [494] Takahara K, Saito H and Inoue T 1999 *Polymer* **40** 3729
- [495] Hutchinson J M 1995 *Prog. Polym. Sci.* **20** 703
- [496] Drozdov A D 1999 *Comput. Mater. Sci.* **15** 422
- [497] Golovchak R, Gorecki Cz, Kozdras A and Shpotyuk O 2006 *Solid State Commun.* **137** 67
- [498] Shpotyuk O, Golovchak R and Kozdras A 2013 *Chalcogenide Glasses* ed J L Adam and X Zhang (Amsterdam: Elsevier) p 209
- [499] Golovchak R, Shpotyuk O, Kozdras A, Vlcek M, Bureau B, Kovalsky A and Jain H 2008 *J. Phys.: Condens. Matter* **20** 245101
- [500] Golovchak R, Kozdras A, Shpotyuk O, Kozyukhin S and Saiter J M 2009 *J. Mater. Sci.* **44** 3962

- [501] Saiter J M 2001 *J. Optoelectron. Adv. Mater.* **3** 685
- [502] Yannopoulos S N and Andrikopoulos K S 2004 *J. Chem. Phys.* **121** 4747
- [503] Golovchak R, Shpotyuk O, Kozdras A, Bureau B, Vlcek M, Ganjoo A and Jain H 2007 *Phil. Mag.* **87** 4323
- [504] Zhang X and Drabold D A 1999 *Phys. Rev. Lett.* **83** 5042
- [505] Li J and Drabold D A 2000 *Phys. Rev. Lett.* **85** 2785
- [506] Street R A and Mott N F 1975 *Phys. Rev. Lett.* **35** 1293
- [507] Boolchand P, Georgiev D G and Micoulaut M 2002 *J. Optoelectron. Adv. Mater.* **4** 823
- [508] Zhao H Y, Koh Y P, Pyda M, Sen S and Simon S L 2013 *J. Non-Cryst. Solids* **368** 63
- [509] www.cecam.org/workshop-0-160.html
- [510] Raty J Y, Zhang W, Luckas J, Chen C, Mazzarello R, Bichara C and Wuttig M 2015 *Nat. Commun.* **6** 7467